Radiofrequency Coils for Ultra-High Field Body MRI

by Sedig Farhat, MSc

Thesis submitted to the University of Nottingham for the degree of

Doctor of Philosophy, 2013

Contents

Abstract

In this thesis, the probes were modelled and constructed at the SPMMRC. All measurements were performed on a 7T Philips scanner. The coils have been successfully evaluated. The dipole, loops, strip line and wrist probes for imaging the pelvis, knee and wrist were tested for clinical use at 7T. Two elements wrist coil can pick up signals from the whole region of interest. The advantage is more uniformity of field of view and better sensitivity. The *in vivo* MRI images acquired in the wrist showed the two elements provided the good quality images for the human wrist. The second study is microstrip line probe. The current flows over the flat-strip were computed, it showed that a significant increase of current close to the edges. This result agrees with theory. We did not use the strip line coil to image a human body, because the coil generated a high SAR/B_1^{+2} level in the region of interest. The third study was of a coil of two square loops. One way of achieving decoupling is to use the overlapping technique to decouple the coils in the simulation. It produced high signal-to-noise ratio and provides a large field of view. Finally, the dipole has been developed for *in vivo* MRI applications. We presented a novel model for determining the length of the PECs required for tuning the dipole at 298 MHz. The efficiency, field of view and homogeneity were improved by adding the flat strip, two strips and array strips dipole. The SAR/B_1^{+2} generated by the dipoles was much less than produced by the loop coil and strip line coil in the pelvis. The dipoles showed the desired improvement in SNR and homogenous coverage. Coverage goes much further into the pelvis and knee as well.

Acknowledgements

I would like to thank a number of people for their various contributions. Firstly, my supervisors: Dr. Paul Glover and Prof. Penny Gowland for their guidance and help throughout this research. I wish to thank Mr. Andre Antunes and Dr. Daniel Lee, Dr. Samuel Wharton and Carolyn Costigan who provided advice and help. I would like to thank my family and friends. I would like to thank the Tripoli University for their funding.

Thank you all.

List of abbreviations

λ	Wavelength
γ	Gyromagnetic ratio
χ	Susceptibility
μ_r	Relative permeability
μ_o	permeability of free space
σ	Conductivity
ρ	Density
ε_o	Permitivity of free space
ε_r	Relative permitivity
ω	Angular frequncy
A	Electric potential
B_o	Static magnetic field

B_1	RF magnetic field
B_1^+	Positive rotating RF field
B_1^-	Negative rotating RF field
C	Capacitance
CCM	Conduction Current Magnitude
E	Electric field
f	Frequency
FFE	Fast Field Echo
FSE	Turbo Spin Echo
FOV	field of view
FID	Free induction decay
G	Magnetic field gradient
I	Current
L	Inductance
M_o	Magnetization
P	Power

PEC	Perfect Electric Conductor
Q	Quality factor
Q_o	Unloaded quality factor
Q_L	Loaded quality factor
R	Resistance
ROI	Region of interest
SAR	Specific absorption rate
SE	Spin echo
SNR	Signal to Noise Ratio
T_1	Longitudinal relaxation time
T_2	Transverse relaxation time
T2WFSE	T2 weighted fast spin echo
V	Voltage
X	Reactance
Z	Impedance

Chapter 1

1 Introduction

There are many diagnostic medical imaging modalities in use today such as X-ray, PET scan, CT scan, Ultrasound and Magnetic Resonance Imaging (MRI). The latter is one of the most useful techniques and is a powerful tool for the visualization of the internal structure of a human being and the functioning of the human brain. It was developed independently by Sir Peter Mansfield [1] and Paul Lauterbur in 1973. They developed techniques which use NMR to produce images. They were both awarded the 2003 Nobel Prize in Medicine for discoveries concerning magnetic resonance imaging. Also Sir Peter Mansfield developed the echo-planar image (EPI) technique in 1977 [2], now used for functional MRI. Thousands of MRI systems have now been installed worldwide, most of them in clinical usage and others for research.

The RF probe coil is one of the main devices in the MRI system. RF probes have two main functions: excitation of nuclear spins and detection of the signals. RF probes can be divided into three categories: 1) transmit and receive probe (transmission mode or/and reception mode), 2) receive only, and 3) transmit only [3]. The probe can be driven in a single mode (one feeding port) or in a quadrature mode (two ports). Two port drive should improve the receiving sensitivity based on the principle of NMR spin direction.

David Hoult [4] stated that the nuclear magnetic resonance (NMR) signal strength may be assessed by application of the principle of reciprocity. Based on this principle, an r.f. coil can be evaluated. Early RF probes were simple wires placed around the region of interest and solenoid probe. A single wire loop probe, and

more generally a set of conductors were the most commonly used to detect the signal.

Technical developments and improvements to magnet design have increased the available the static magnetic field, which is extremely significant to enhance the image quality. Low field MRI is not as sensitive as high field, given that the Larmor frequency increases as the static magnetic field increases as well as the net magnetisation. As the frequency increases then the wavelength becomes shorter than the dimensions of a sample volume. At 7 T (300 MHz) the wavelength inside the head and pelvis of a human body are approximately 12.5 *cm* and 13.1 *cm* respectively. Therefore, the dimension of the head as an example is roughly twice the operational wavelength [5]. Moreover, the inhomogeneity caused by the dielectric and boundary conditions in the human body, become significant at high field strength [6]. Raised RF attenuation in tissue causes decreased B_1 efficiency due to conductivity [7]. Also, RF power deposition increases causing a higher SAR for a given B_1 [8].

It is difficult to generate uniform radio frequency over a sample volume of interest and also not easy to design and build large size RF probes which operate at high frequency when the wavelength of a high frequency in human approaches the RF coil's dimension [6]. However, an alternative approach is the transceiver array probe, where this design will allow for independent phase and amplitude to be controlled for each individual element [9]. Uniformity is necessary for RF probe as any RF inhomogeneity affects the flip angles and hence the contrast [1]. The B_1^+ uniformity is required to produce accurate multi-echo pulse sequences. The geometrical structure of an rf coil also needs to be considered. Design of RF coils involves the accurate characterization of the electromagnetic field distributions inside a biological sample. The Biot-Savart law can be used at a low field strength, which gives very good approximations. However, at high field strength it is necessary to solve fully Maxwell's equations to determine the interaction between the coil and phantom or human tissues [10]. There are several methods, which have been used in the past; the most popular one is the Finite Difference Time Domain (FDTD) method. Using high field such as 7T faces

technical challenges in obtaining good RF penetration, sensitivity, homogeneity and also a large field of view. All these parameters may be modelled for each design of coil and discussed in this research.

This research will undertake to design and build a range of RF surface coils for scanning on a 7T at Nottingham University. In this thesis we wish to answer the question: which of these geometries is optimum for imaging at high field? The work in this research is focused on the development of RF coils, which can be used to overcome some difficulties such as inhomogeneity, by imaging a far field region. The probes will be able to scan a human knee, wrist and pelvis. Before building any coils, it is necessary to model the coil by applying FDTD simulations to develop new coil geometry. Previous studies have shown that the B_1^+ field distribution depends on the geometry of the coil and signal to noise ratio (SNR) and sensitivity vary as a function of the B_1. The commercial software XFDTD will be used to simulate the electromagnetic properties of different coil geometries such as the wrist coil, microstrip line, circular loop coil and dipole coil.

To develop and improve the probe efficiency, the current distributions must be calculated on the surface of the probe. To obtain deep B_1^+ penetration, the Poynting vector may be computed to evaluate the probe. To achieve a good optimization, all model dimensions should be considered the same as those that will be utilized in experiments. For that reason, the B_1^+, B_1^- and SAR must be determined in order to obtain the best performance of the probe. There are many precautions that should be taken into account through the stages of designing the probe such as obtaining high SNR and low SAR, which can be achieved by using the FDTD method and MATLAB codes. The aim of this project is to design and build an RF probe to be used on a 7T for wrist, knee and pelvis scanning.

In 2010 Raaiimakers et al. [8] published a first paper that first proposed using the dielectric material made of a ceramic . This paper described a good comparison between the dipole, loop and stripline coils. In 1990 Roemer et al. published a paper [11] which details the coupling and decoupling technique. The overlapping

technique was reported. By using this technique, it is possible to compensate mutual induction to almost zero. In 2003 Kwok et al. published a paper which provides description of how to reduce electrical coupling with a knee coil by distributing three capacitors in each element and the overlapping technique was used to decouple the elements [12]. Pruessmann et al. [13] have constructed a mechanically adjustable coil array for wrist MRI. They used low pre-amplifier impedance to decouple eight elements. The paper by Collins et al. [14] provides a good description about the calculations of B_1 distributions, SNR and SAR. In 1998 Chen et al. [15] published a paper. This paper detailed the FDTD method. It provides numerical simulation of SAR and B_1. In 1996 C. Gabriel et al. [16] published a paper regarding the dielectric properties of biological tissues. This paper provides an overview about the relative permittivity and conductivity of tissues at different frequencies.

1.1 Thesis Outline

The thesis is organised into eight chapters. Chapter one presents the introduction and scope of this thesis. Chapter two presents the MRI theory and instrumentation such as main magnet and gradient coils.

Chapter three demonstrates the RLC circuit, coaxial cables, quality factor, coupling and decoupling. It also details noise and eddy current effects. Next we describe how to simulate the coils using theory relevant to the Finite Difference Time Domain (FDTD) method, explore tissues properties, as well as finally presenting the segmentation of the female pelvis model. Chapter four details the development of the wrist coil, modelling both one and two elements. The B_1^- mapping, sensitivity and the decoupling technique are shown.

Chapter five presents microstrip transmission line theory and then models the one strip line and two strip line. It also computes the B_1^+ and specific absorption rate (SAR), testing one element and two elements on the 7T. Chapter six provides background information about the loop coil, models one-loop coil, and two-loop

coils, and explores coupling and decoupling of the two loops. It also tests one element coil on the 7T.

Chapter seven focuses on the development of the dipole antenna for transmit and receive. Initially based on a water dielectric, which is a novel design, then the modelling and building of the dipole antenna using a ceramic material is described. A high frequency RF surface coil based on the use of ceramic has been developed for *in vivo* MRI applications on the human pelvis at 7T. This chapter deals with four different types of dipoles. We will describe modelling the dipole antenna as mounted on the ceramic one-strip, two-strip, flat-strip and array strips. Comparisons with phantom studies were performed. Chapter eight contains a brief summary of the results obtained from the simulations, tests of the coils on the 7T and comparing results of simulations with different parameters; some future work is also suggested in this chapter.

References:

1. McRobbie, D.W., E.A. Moore, M.J. Graves, and M.R. Prince, *MRI From Picture to Proton*2007, United States of America: Cambridge Press.

2. Mansfield, P., *Multi-planar image formation using NMR spin echoes.* Journal of Physics C: Solid State Physics, 1977. **10**: p. 10:L55-58.

3. Hernandez, R., A. Rodriguez, P. Salgado, and F. Barrios, *Concentic dual loop RF coil for magnetic resonance imaging.* Revista Mexicana De FISCA, 2003. **49**(2): p. 107-114.

4. Hoult, D.I., *The Principle of Reciprocity in Signal Strength Calculations.* Magnetic Resonance, 2000. **12**(4): p. 173-187.

5. Ibrahim, T., R. Lee, B. Baertlein, A. Abduljalil, H. Zhu, and P. Robitaille, *Effect of RF coil excitation on field inhomogeneity at ultra high fields: A field optimized TEM resonator.* Magnetic Resonance imaging, 2001. **19**: p. 1339-1347.

6. Zhang, X., K. Ugurbil, and W. Chen, *A microstrip transmission line volume coil for human head MR imaging at 4T.* Magnetic Resonace 2003. **161**: p. 242-251.

7. Wald, L.L., G.C. Wiggins, A. Potthast, and C. Triantafyllou, *Design Consideration and Coil Comparisons for 7 T Brain Imaging.* Appl. Magn. Reson., 2005. **29**: p. 19-37.

8. Raaijmakers, A.J.E., O. Ipek, D.W.J. Klomp, C. Possanzini, and C.A.T. Van den beng, *Design of a Radiative Surface Coil Array Element at 7 T: The Single-Side Adapted Dipole Antenna.* Magnetic Resonance in Medicine, 2011. **66**(5): p. 1488-1497.

9. Wu, B. and R. Krung, *7T Human Spine Imaging Arrays with Adjustable Inductive Decoupling.* IEEE Trans. Biomed. Eng., 2010. **57**(2): p. 397-403.

10. Wang, S. and J.H. Duyn, *Time -domain finite difference/ finite-element hybrid simulations of radio frequency coils in magnetic resonance imaging.* Phys. Med. Biol., 2008. **53**: p. 2677-2692.

11. ROEMER, P.B., P.S. Souza, and O.M. Mueller, *The NMR Phased Array.* MAGNETIC RESONANCE IN MEDICINE, 1990. **16**: p. 192-225.

12. Kwok, W.E., J. Zhigang, G. Seo, and S.M. Totterman, *A four-element phased array coil for high resolution and parallel MR*

imaging of the Knee. Magnetic Resonace Imaging, 2003. **21**: p. 961-967.

13. Nordmeyer, J.A., N. De Zanche, and K.P. Pruessmann, *Mechanically Adjustable Coil Array for Wrist MRI.* Magnetic Resonance in Medicine, 2009. **61**: p. 429 – 438.

14. Collins, C.M. and M.B. Smith, *Calculations of B1 distribution, SNR, and SAR for a surface coil adjacent to an anatomically-accurate human body model.* Magnetic Resonace in Medicine, 2001. **45**: p. 692-699.

15. Chen, J., Z. Feng, and J.M. Jin, *Numerical Simulation of SAR and B1 Field Inhomogeneity of Shielded RF Coils Loaded with the Human Head.* IEEE TRANSACTIONS ON BIOMEDICAL ENGINEERING, 1998. **45**(5): p. 650-659.

16. Gabriel, C., S. Gabrriel, and E. Corthout, *The dielectric properties of biological tissues.* Phys. Med. Biol., 1996. **41**: p. 2231-2249.

Chapter 2

Magnetic Resonance Principles

2 Magnetic Resonance Imaging (MRI) Theory

In this chapter, the basic principles of magnetic resonance imaging (MRI) are described. The main components and function of MRI scanner components such as the magnet and gradient coils are described.

Nuclear magnetic resonance (NMR) is a phenomenon observed when nuclei such as hydrogen are placed in a magnetic field B_0. The main concept behind magnetic resonance is that some nuclei have the property of spin leading to a magnetic moment $\boldsymbol{\mu}$. MRI is based on the interaction between an applied magnetic field and a spin. In the absence of an applied magnetic field the magnetic moments of the protons are orientated in a random manner, but when the sample is placed in the magnetic field a new thermal equilibrium state is created [1]. The spin orientations are parallel and anti-parallel and have different energies. The parallel (spin up) orientation to B_0 has lower energy while the anti-parallel (spin down) has higher energy [2].

2.1 Boltzmann Distribution

The population distribution of spins between spin-up and spin-down states can be described as:

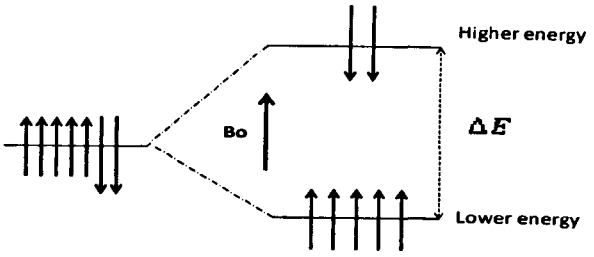

Figure 2.1-1 shows Zeeman energies.

$$\frac{N_\alpha}{N_\beta} = \exp\left(-\frac{\Delta E}{k_B T}\right), \qquad 2.1.1$$

Where N_α and N_β are the numbers of spins in the spin-down state and spin-up state respectively, and ΔE is the energy difference between the states. The difference in population at high temperature can be computed as given by.

$$N_\beta - N_\alpha \cong \frac{N\gamma B_o}{2k_B T}, \qquad 2.1.2$$

Where T is the temperature, B_0 is the static magnetic field and k_B is the Boltzmann constant ($1.38 \times 10^{-23} JK^{-1}$).

The summation of parallel and anti-parallel magnetic moments over the whole sample will be non-zero and has a value of M_0. This is called the net magnetization; the vector has the same direction of B_0:

$$M_0 = \chi B_0, \qquad 2.1.3$$

Where χ is the susceptibility.

In a homogenous static magnetic field of strength B_0 the equilibrium magnetization M_0 is defined by the Langevin equation [3]:

$$M_0 = \frac{\gamma^2 h^2 \rho B_0}{4 k_B T}, \qquad 2.1.4$$

Where k_B is Boltzmann's constant, T is the absolute temperature and ρ is the number of nuclei per unit volume.

The MRI principle can be described using both a classical approach and quantum mechanics. It was noted that there are two possible states for protons $\pm 1/2$ which have a magnetic moment μ [4] as shown in Figure 2.1-2.

$$\boldsymbol{\mu} = \gamma \mathbf{I}, \qquad 2.1.5$$

Where γ the gyromagnetic ratio (point charge in circular motion = (q/2m)) and **I** is the angular moment.

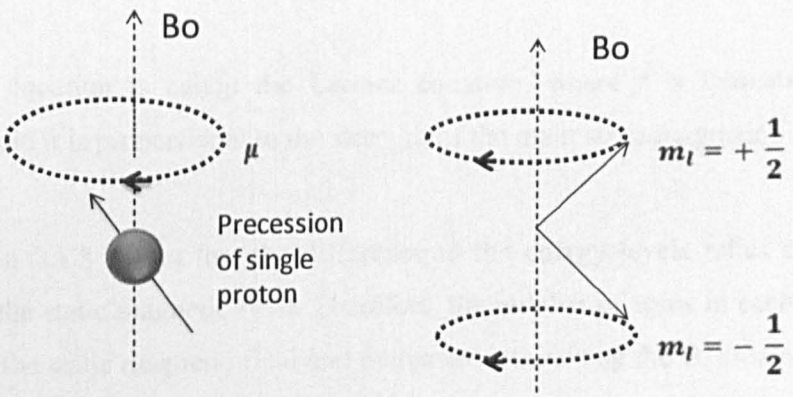

Figure 2.1-2: Precession of the magnetic moment about B_o.

The magnitude of the angular moment is quantized, meaning it has an integer number ranging from $+I$ to $-I$ and the z component can be written as:

$$I_z = m\frac{h}{2\pi}, \qquad 2.1.6$$

$$\mu_z = \gamma m \frac{h}{2\pi}. \qquad 2.1.7$$

It was found that when a sample or human body is placed in the magnetic field, a new thermal equilibrium is established and the magnetic moment gains the energy, The Zeeman energies can be written as the difference between two states.

$$\Delta E = \gamma m \frac{h}{2\pi} B, \qquad 2.1.8$$

where m=-I, -I+1... I

The resonance frequency can be defined as [5]:

$$f = \frac{\Delta E}{h} = \frac{\gamma B_o}{2\pi}, \qquad 2.1.9$$

The above equation is called the Larmor equation, where f is frequency of precession and it is proportional to the strength of the main static magnetic field.

The equation 2.1.8 shows that the difference in the energy levels relies on the strength of the static magnetic field. Therefore, the number of spins in each level depends on the static magnetic field and increases with raising the B_o as shown in Figure 2.3-1.

2.2 Equation of Motion

The NMR phenomenon can be described using either a classical or a quantum mechanical approach. In the classical theory of motion, the dynamics of a magnetic moment in the external field **B** can be expressed as:

$$\frac{d\boldsymbol{\mu}}{dt} = \gamma\,(\boldsymbol{\mu} \times \mathbf{B}), \qquad 2.2.1$$

The above differential equation can be written in terms of three Cartesian equations:

$$\frac{d\mu_x}{dt} = \gamma\mu_y B_0 = \omega_o \mu_y, \qquad 2.2.2$$

$$\frac{d\mu_y}{dt} = -\gamma\mu_x B_0 = -\omega_o\, \mu_x, \qquad 2.2.3$$

$$\frac{d\mu_z}{dt} = 0. \qquad 2.2.4$$

In fact, the magnetic moment in the main static magnetic field rotates in two-dimensional transverse planes. μ_x *and* μ_y can be written in two terms, real and imaginary parts:

$$\mu_+(t) = \mu_x(t) + i\,\mu_y(t), \qquad 2.2.5$$

$$\mu_+(t) = \mu_+(0)e^{-i\omega_0 t}, \qquad 2.2.6$$

This represents a clockwise rotation in the complex plane.

2.3 Free Induction decay (FID)

Based on the principle of reciprocity, when applying unit current to the probe and the B_1 generated at the sample, the signal induced in the probe by the precessing nuclear magnetic moment, M, will be proportional to the strength of this field and given as [6]:

$$\xi = -\frac{d}{dt}(B_1.M). \qquad 2.3.1$$

The most basic NMR experiment is the generation of a free induction decay signal. When the sample is placed in a homogeneous magnetic field and the r.f probe placed very close to the sample to generate B_1 at the Larmor frequency, the B_1 field causes the spins to flip into the transverse x-y plane [7]. When the B_1 is switched off, the spins return to their equilibrium state and the probe receives the signal. The FID then decays exponentially. The rate depends on the uniformity of B_0 and the T_2 of the sample. This provides information about the environment of the spins. A simple Fourier transform of the free induction decay provides the complex signal or phase amplitude signal [8].

To excite the spins we apply an electromagnetic wave to the region of interest using RF coils or antenna. After applying a 90° RF pulse, the observable magnetization of the sample in the *x-y* (or transverse) plane.

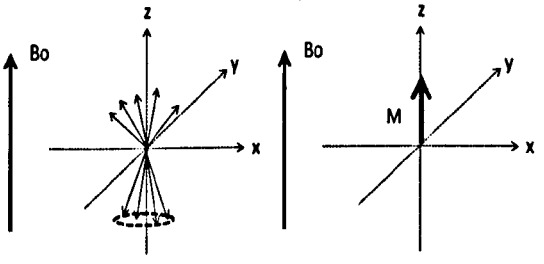

Figure 2.3-1: Alignment of protons under the influence of the external applied magnetic field.

If the longitudinal magnetization is rotated into the *x-y* plane as shown in Figure 2.3-2. The transverse magnetization can be described by

$$M_{xy}(t) = M_0 e^{-\frac{t}{T_2}}, \qquad 2.3.2$$

Where T_2 is the transverse (spin-spin) relaxation time.

The transverse magnetization M_{xy} rotates about the z-axis. This induces an alternating voltage which has the same frequency as the Larmor frequency in a receiver when the coil is tuned at the same frequency. The induced *emf* in the receiver coil is expressed by

$$emf = -\int \frac{B_1}{I_c}\frac{\partial M}{\partial t} dV. \qquad 2.3.3$$

Transverse plane M_{xy} is MRI signal that is detected to form MRI image. The time needed to decay the transverse magnetization to 37% is called the T_2 relaxation time and is also known as the spin-spin relaxation time. It was found that the T_2 of body tissues varies from less than a few milliseconds for bone to more than a second (1000 ms) for simple fluid such as bulk water [9]. Transverse magnetization decays and the moments realign with the main magnetic field, as transverse magnetization decays, the longitudinal magnetization is slowly recovery, and this process is called longitudinal relaxation or T_1 recovery.

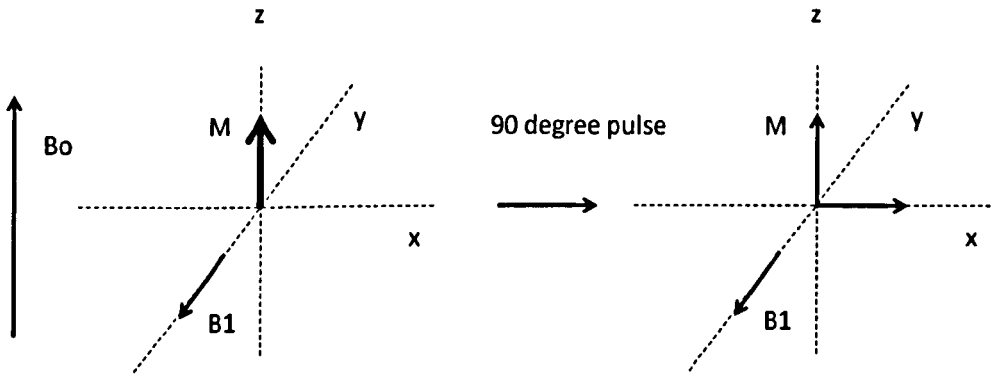

Figure 2.3-2: The magnetization (M) rotates into the transverse plane.

T_1 is a characteristic of the sample and the time needed for 63% of the magnetization to recover; it can be described by equation:

$$M_Z = M_O\left(1 - e^{-t/T_1}\right), \qquad 2.3.4$$

Where T_1 the spin-lattice relaxation time (longitudinal) [10].

2.4 Linearly and Circularly Polarized Magnetic Fields

The 2D Cartesian can be replaced by a left circular or right circular unit vector:

$$x^{left} = \hat{x}\cos\omega t - \hat{y}\sin\omega t,$$
$$x^{right} = \hat{x}\cos\omega t + \hat{y}\sin\omega t, \qquad 2.4.1$$

Now, the amplitude B_1 can be written as the left-handed or right-handed and then by combining of 2.4.1, the two terms produce the linear RF field along x, as shown in the first equation, which is the clockwise (negative) and the second equation, which is the counter-clockwise (positive). A linearly polarized B_1 can be produced as the sum of two components rotating around the z-axis at same frequency but in the opposite directions as:

$$B_1^L = B_1 e^{-i\omega t}, \qquad 2.4.2$$

$$B_1^R = B_1 e^{i\omega t}, \qquad 2.4.3$$

$$B_1^{lin} = B_1^L + B_1^R = 2B_1\cos\omega t. \qquad 2.4.4$$

Moreover, by adding two linearly polarized RF fields that have the same frequency and also the same peak amplitude, but which are spatially orthogonal perpendicular to each other but having a 90-degree relative phase, will generate circular polarization, as shown in:

$$B_1^{cir} = B_1(\hat{x}\cos\omega t - \hat{y}\sin\omega t), \qquad 2.4.5$$

Driving each component 90-degrees out of phase in the x and y coordinates of the laboratory frame is called a quadrature drive [11]. When simulating the RF coils, magnetic fields (H_x, H_y and H_z) are saved in FDTD and MATLAB code, which are used to compute either B_1^+ or B_1^- based on the following equations

$$B_t^+ = B_{tx} + iB_{ty}, \qquad 2.4.6$$

$$B_t^- = B_{tx} - iB_{ty}, \qquad 2.4.7$$

where B_t^+ is the positive and B_t^- is the negative circularly polarized components.

2.5 Quadrature Driving

Excitation of nuclear magnetization can be achieved by applying circularly polarized RF rotating in the direction of Larmor precession of the spins. It can be shown that if the coil is required to function in a quadrature mode, it should have two decoupled resonant modes, which can generate orthogonal magnetic field components. The quadrature mode requires two feeding ports on the coil and uses a circuit that splits the excitation power in quadrature as shown in Figure 2.5-1. The coil should be correctly connected to the quadrature interface box in order to generate B_1^+ rather than B_1^-. The field generated by linearly polarized coils may change in magnitude and the direction inside the sample or region of interest due to attenuation or wave effects. Therefore, combining the field from two elements of coil may produce elliptic polarization in the ROI [12].

A circularly polarized magnetic field is generated when driving the RF coil in quadrature mode, which is efficient in exciting the spins during MRI experiments. Whereas, driving the coil in a single mode will produce a linearly polarized

magnetic field that is only half as efficient in rotating the spins. It means the SNR increases by this factor. It therefore requires half of the transmitter RF power compared to the signal drive. This mode also potentially allows a receive sensitivity gain by a factor of $\sqrt{2}$.

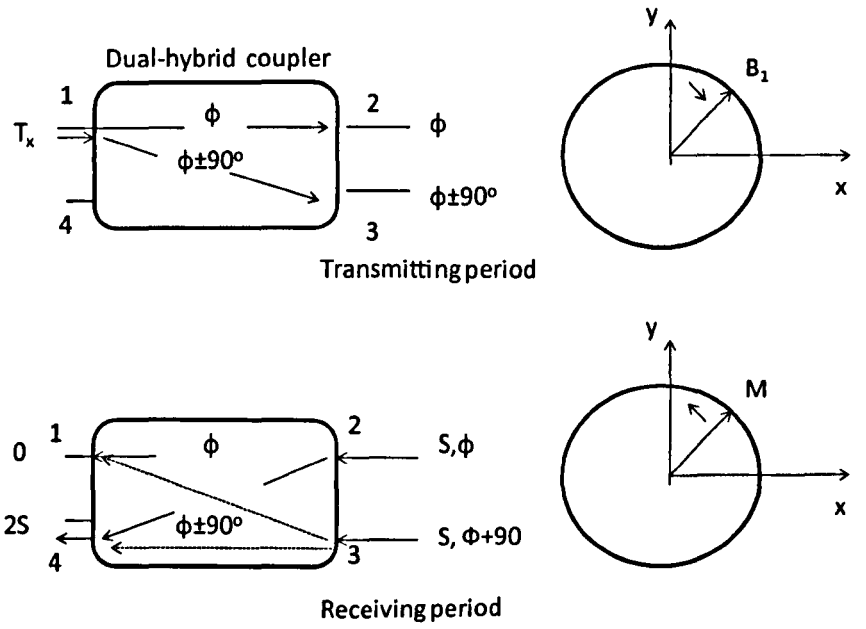

Figure 2.5-1: The transmitter pulse on port 1 is divided into quadrature modes to port 2 and 3, and used to generate a rotating magnetic field. In receive mode, if the generated magnetization is in the same direction as the Larmor precession, it induces voltages (S), in quadrature which are summed at port 4.

2.6 PIN Diode

A PIN diode is a special kind of semiconductor diode. PIN diodes can be used to control RF power in circuit such as switches, phase shifters, attenuators and modulators. There is a difference between the PIN diode forward bias and reverse bias. An ideal switch device acts as low or zero impedance to current flow in the ON state and high impedance to current flow in the OFF state. The PIN diode acts

as low impedance for RF under forward bias and high impedance under reverse bias. The characteristics of the PIN diode will be utilized when building and designing probes such as the wrist coil which functions as an RF receiver coil. By using a PIN diode the coil may be de-tuned during transmit periods.

2.7 Switching

An RF probe may sometimes be used as both a transmitter and receiver where a switching device allows double functioning of the coil. Lowe and Tarr, (1968) stated that the 'switch' is easily made by means of crossed diodes and quarter wavelength lines as shown in Figure 2.7-1. The crossed diodes should be connected in series with the transmitter. High series impedance is presented when the transmitter is off. A quarter wavelength transmission line works as a transformer, which translates its output impedance as shown in the following equation:

$$\text{Z input} = \frac{Z_o^2}{Z_{output}}. \qquad 2.7.1$$

During pulses, when the shunt diodes are acting as a short circuit, the input impedance of the quarter wavelength line is infinite and the receiver is effectively disconnected from transmit circuit. Conversely when the coil is receiving very low signal amplitudes from the coil, then the diodes are high impedance and the coil is effectively connected directly to the pre-amplifier.

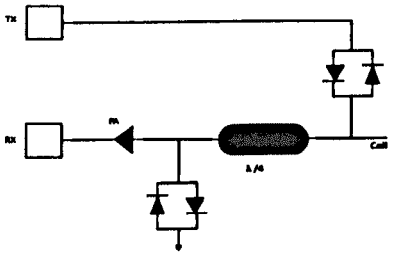

Figure 2.7-1: The Transmit/receive and switching network, Tx transmitter, Rx receiver, PA preamplifier.

2.8 Instrumentation

The MRI instrument consists of a radio transmitter and receiver, magnetic field gradient coils, and a main magnet as shown in Figure 2.8-1. Firstly, for MRI the main static magnetic field might be in the range from 0.5 T to 9.4 Tesla. Secondly, the gradient coils are used to determine the location of MRI signals to obtain an image. Finally, an r.f field is needed for excitation of the transverse magnetization in the sample, this can be achieved by RF coils.

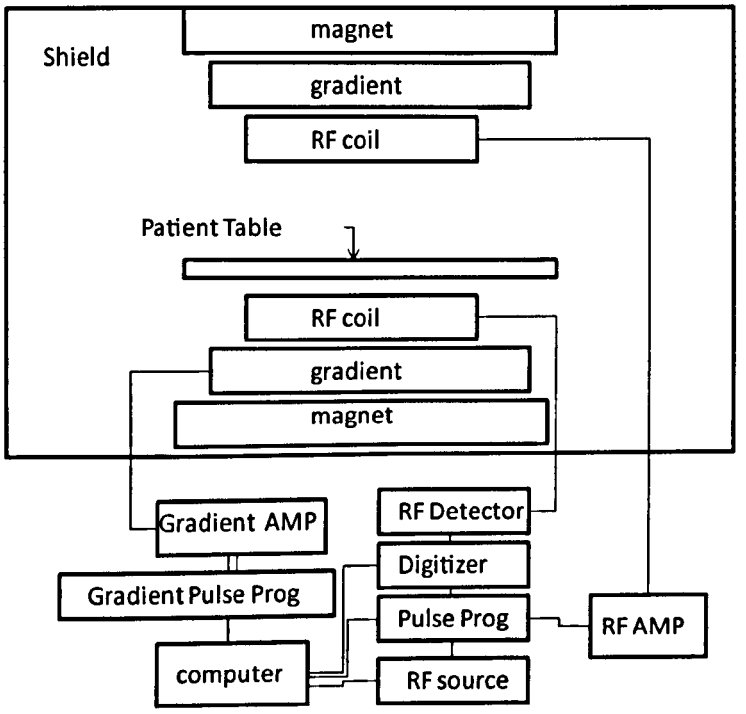

Figure 2.8-1: The schematic diagram of an MRI unit.

2.9 Main Magnetic Field

The main static magnetic field B_o is needed to produce the longitudinal magnetization in the sample. The direction of the static magnetic field is usually in the *z*-axis direction. From theory, the signal to noise ratio SNR is a function of the static magnetic field and usually increases linearly with field strength at above 1.5T [13]. The main static magnetic field that extends outside the scan room is

decreased by active shielding. The fringe field decreases rapidly at a distance of r from the main magnetic, as given by:

$$B_{FF} \propto \frac{B_o}{r^3}, \qquad 2.9.1$$

The fringe field has radial components (x, y) and the axial field is in z direction [14]. The latter will be greater than the radial field at any distance. The main magnetic field should be homogeneous to obtain a good quality image. A good homogeneity is needed and better than 5 ppm or more is required. It can be computed using the following equation:

$$Homogeneity\ (ppm) = \left(\frac{field\ strength_{max} - field\ strength_{\ min}}{field\ strength_{average}}\right) \times 10^6. \qquad 2.9.2$$

2.10 Gradient Coils

The magnetic field gradient coils consist of three coils. The coils generate magnetic fields, where the B_Z components vary linearly with position, and hence they are able to generate a systematic variation in frequency. It can be said that the gradients are additional fields produced by gradient coils and the gradient fields add or subtract from the static magnetic field B_0. In the absence of gradient fields, all protons precess at the same frequency with only small variations caused by the magnetic field heterogeneity, as well as differences in chemical shift. The gradient coil is an essential component in the MRI system in order to distinguish between signals emitted from the voxels in different locations in the sample or tissues. Three orthogonal magnetic fields gradient of B_z can be defined as:

$$G_x = \frac{\partial B_z}{\partial x}, G_y = \frac{\partial B_z}{\partial y}\ and\ G_z = \frac{\partial B_z}{\partial z}, \qquad 2.10.1$$

These are designed to generate varying magnetic fields varying in three dimensions in x, y and z directions.

2.11 Frequency Encoding, Phase Encoding and Slice Selection

Three of the steps towards localization in order to construct an MRI image as pixels in matrix are: slice selection, phase encoding and frequency encoding.

The first step in MRI imaging is the localization of the RF excitation to a plane of interest, in order to excite the protons there and recorded the resulting signal. This is obtained by utilizing a technique known as slice selection which is applied to isolate a signal slice in the sample [3]. A magnetic field gradient is generated normal to the plane direction causing the frequency of spins to vary in this direction. A band-limited RF pulse is then applied and only spins in the desired plane will be excited.

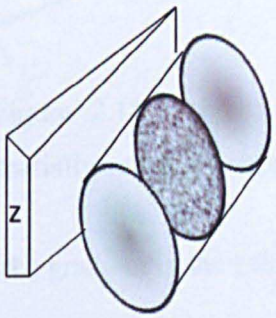

Figure 2.11-1: Slice selection.

The slice thickness is determined by the gradient amplitude G_{ss} and the bandwidth of frequencies ($\Delta\omega=\gamma\Delta$ (G_{ss} × thickness)). Where $\Delta\omega$ is fixed, therefore the slice position is varied by adjusting the varying the central frequency which is computed by ($\omega_i = \gamma (B+G.r_i)$). Where ω_i is the frequency of the spin at r_i and G is total gradient amplitude.

During reception of the signal the Larmor frequency of a spin is linearly proportional to its position when the static magnetic field is a spatial linearly varying field. This variation is usually very small compared with the magnitude of the static field, so the frequency offset is proportional to position. The aim of using this readout gradient or frequency encoding is to encode the position of the spin. A new equation that expresses the magnetic field in a z gradient can be written as

$$B_z(z,t) = B_o + zG_z(t), \qquad 2.11.1$$

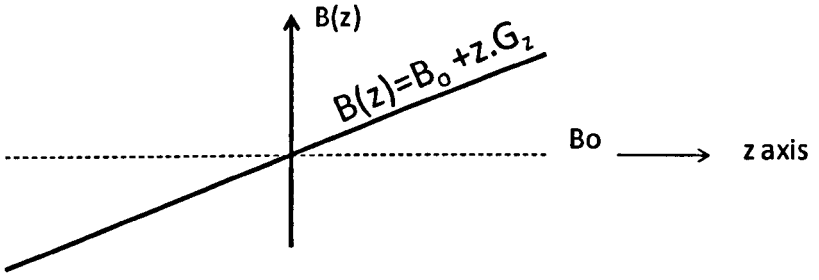

Figure 2.11-2 shows how gradient coils generate the spatially varying component of the B_0 magnetic field.

Where G_z is the gradient in the z direction:

$$G_z = \left(\frac{\partial B_z}{\partial z}\right). \qquad 2.11.2$$

Figure 2.11-2 shows that the static magnetic field is high at one end of the gradient axis and low at the other end, while in the centre it should be equal to B_0. It can be described as the variation in the frequency of the spins as:

$$\omega(z,t) \equiv \omega_o + \omega_G(z,t). \qquad 2.11.3$$

It encodes the MRI signal in the phase encoding direction. A similar process is used for the phase encode direction as this is the same as frequency encoding except sampled in discrete steps. All the information necessary to reconstruct an image is stored in the raw data matrix an alternative way to describe the raw data matrix is called the *k* space and then a Fourier transform is used to generate the MRI images [2].

References:

1. Bloch, F., The principle of nuclear induction, in Nobel Lecture 1952.
2. Brown, M. and R. Semelka, MRI Basic Principles and Applications 2003: Wiley Liss.
3. McRobbie, D.W., et al., MRI From Picture to Proton 2007, United States of America: Cambridge Press.
4. Gibbs, M.L., Nuclear Magnetic Resonace, 2007: Georgia Institute of Technology, School of Physics, Atlanta.
5. Morris, P., Nuclear Magnetic Resonance Imaging in Medicine and Biology 1986, USA: Oxford University Press New York.
6. Hoult, D.I., The Principle of Reciprocity in Signal Strength Calculations. Magnetic Resonance, 2000. **12** (4): p. 173-187.
7. Levitt, M.H., Spin dynamics: Basics of Nuclear Magnetic Resonance 2008: John Wiley and Sons Ltd.
8. Freeman, R., A Handbook of Nuclear Magnetic Resonance 1997, Singapore Longman Singapore
9. Donald, G. and S. Cohen, MRI PRINCIPLES 2004, USA.
10. Mansfield, P. and P.G. Morris, NMR imaging in biomedicine 1982: Academic press, INC. (London).
11. Haacke, E.M., et al., Magnetic Resonance Imaging Physical Principles and sequence design 1999: John Wiley and Sons.
12. Sled, J.G. and B. Pike, Understanding Intensity Non-uniformity in MRI, McGill University: Canada.
13. Tamer, S., et al., Effect of RF coil excitation on field inhomogeneity at ultra high fields: A field optimized TEM resonator. Magnetic Resonance imaging, 2001. **19**: p. 1339-1347.
14. Liney, G., MRI from A to Z 2005: Cambridge University

Chapter 3

RF Circuits and Electromagnetic Modelling Theory

3 Introduction

This chapter will focus on the electric circuit design and properties of elements such as: ba-luns, probe tuning and matching; behaviour of coax cable; plus the coupling and decoupling techniques used in this thesis. The signal to noise ratio, quality factor, and the method used to simulate the RF coils and modelling the pelvis will be detailed. The specific of FDTD modelling and how it is used to determine MRI related parameters such as SAR and B_1^+ is discussed.

3.1 Tuning and Matching

MRI coils are composed of three main electrical elements: inductor (L), capacitor (C) and resistor (R), as shown in Figure 3.1-1, in practice these are not components, as the reactive and resistive properties are distributed. The reason for using these components is that amounts of energy can be stored in the capacitors as electric fields and in the inductors as magnetic field. By applying Kirchhoff's laws to the circuit, the total series impedance can be computed as:

$$Z = R + jL\omega + \frac{1}{jC\omega} = R + j(L\omega - \frac{1}{C\omega}), \qquad 3.1.1$$

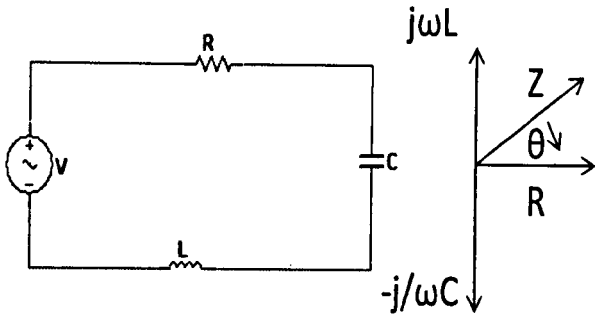

Figure 3.1-1: The series resonant circuit.

The electrical matching circuit is still a significant part of an RF probe. Circuits composed of capacitors are usually used to match any probe to the impedance of the receiver [1]. The impedance can be written in complex notation as:

$$Z=R+\mathrm{j}X, \qquad 3.1.2$$

Where R represents the real projection along the horizontal axis known as the resistive component and X represents the imaginary projection along the vertical axis known as the reactive component.

When the circuit is a pure resistance (X=0), the current and voltage are in phase. When this condition is met, the energy is exchanged back and forth, between the capacitor and the inductor and dissipates slowly in the resistor R, this occurs when the circuit is resonant.

However, there are two states, which should be considered: when X is greater than zero or less than zero then the imaginary component acts as an inductor or a capacitor respectively. In these cases the current and voltage must be out of phase.

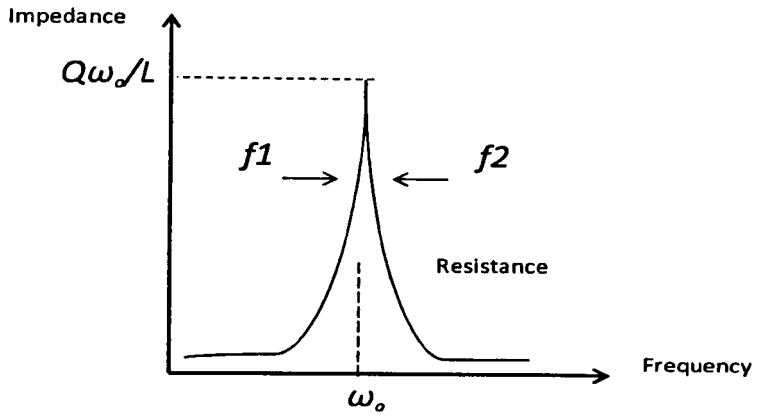

Figure 3.1-2: The real part of the coil impedance.

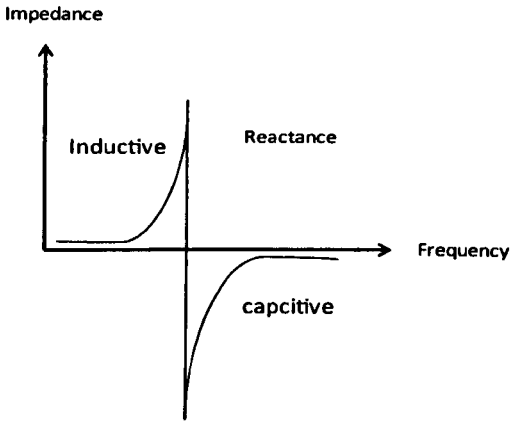

Figure 3.1-3: The imaginary part of the coil impedance [2].

3.2 Impedance matching

Research in the field of electrical power has developed the concept of impedance matching. To carry this out in a suitable way in an electronic laboratory the Smith Chart should be used, which was invented by Philip Smith (1905-1987). This chart was made, because impedance is a function of frequency. It defines the reflection coefficient Γ, which is a complex quantity which can be described by a magnitude and phase angle or a real part and an imaginary part:

$$\Gamma = |\Gamma| e^{j\theta} = \Gamma_r + j\Gamma_i , \qquad 3.2.1$$

Where

$$\Gamma_r = |\Gamma| \cos\theta , \qquad 3.2.2$$

$$\Gamma_i = |\Gamma| \sin\theta , \qquad 3.2.3$$

Where Γ is known as the reflection coefficient.

The Smith chart is usually used to represent a number of parameters such as impedance and complex reflection coefficient S_{nn}. It has become a principal presentation for displaying the performance of microwave circuit [3]. In this research, it was used to observe the behaviour of the RF coil and display the impedance matching of RF coils on a network analyzer. The input impedance of the probe should be matched to 50 ohms to minimize reflections and maximize power transfer [4]. The complex conjugate matching form that has been used to transfer power between a reactive source and a reactive load at a single frequency should be considered as expressed in:

$$Z_{Load} = Z^*_{Source}, \qquad 3.2.4$$

When the circuit resonates at its natural frequency, the reactance term should be equal to zero and the above form reduces to a purely resistive source and loaded impedance:

$$Z_{load} = Z_{source}. \qquad 3.2.5$$

Maximum power transfers from the signal source to the load when impedance of the signal source equal is to the complex conjugate of the load impedance. This is essential for high power transmit probes for example.

The idea is to use matching capacitors to vary the impedance of the probe until 50 ohms is obtained. Furthermore, a balanced matching network has been used. It consists of two matching capacitors connecting both ends of a simple probe, one to the ground and the second to the cable central connection. The values of these capacitors should be twice the matching capacitor, which is demonstrated in Figure 3.2-1 (B). The impedance of both capacitors will be equal, resulting in the same voltage, but the amplitude will be half. Compared to an unsymmetrical case, the symmetrical case has the advantage of reducing radiation losses.

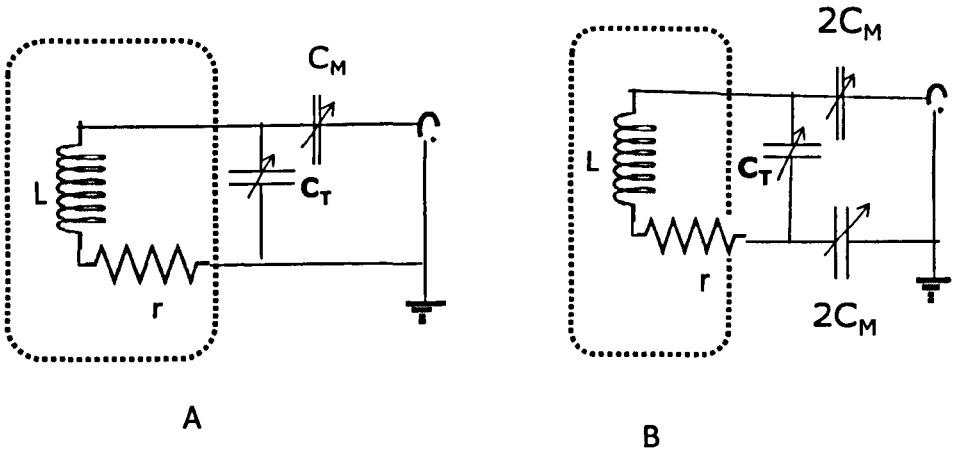

Figure 3.2-1: (A) the capacitive matching and (B) a simple balanced matching circuit.

3.3 Baluns

In the previous section we described the impedance matching circuit. In this section we present many types of the balun circuits, which is a type of electrical transformer, sometimes used to convert unbalanced to balanced signal. It was noted during the design of RF probes that a balun is very significant and sometimes needed in a probe circuit. It can remove currents on the outer shield of

the cable that induce RF signal into devices close to the probes and also reduce instability of the S parameter measurement. Figure 3.3-1 demonstrates the $\lambda/4$ balun that is called the Bazooka balun. Quarter wavelength transmission lines will present finite impedance at input. This type of balun acts as a 1:1 transformer, which means that the impedance at the balanced port is the same as the impedance at the unbalanced port. A half wavelength coax cable $(\frac{\lambda}{2})$ can be used as a balun circuit as shown in Figure 3.3-2; this type of balun acts as a 4:1 transformer, which means the impedance at the balance port is 4 times more than the impedance at the unbalanced port. The second type of balun is used with a coax cable as $\lambda/4$ a quarter wavelength and $3\lambda/4$ wavelength, connected with any cable length as shown in Figure 3.3-3.

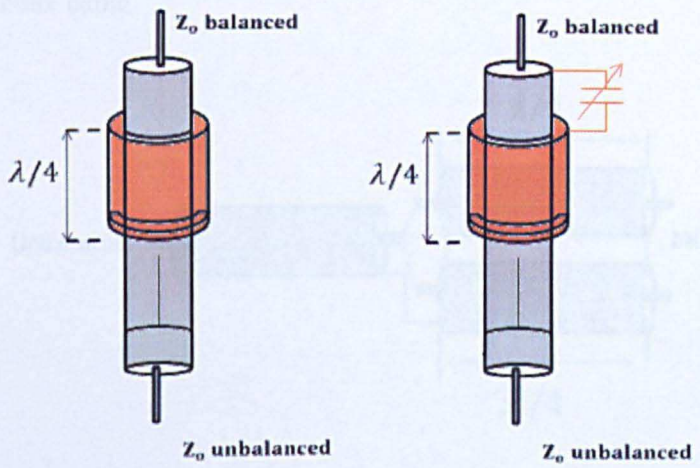

Figure 3.3-1: Narrow band balun transformers.

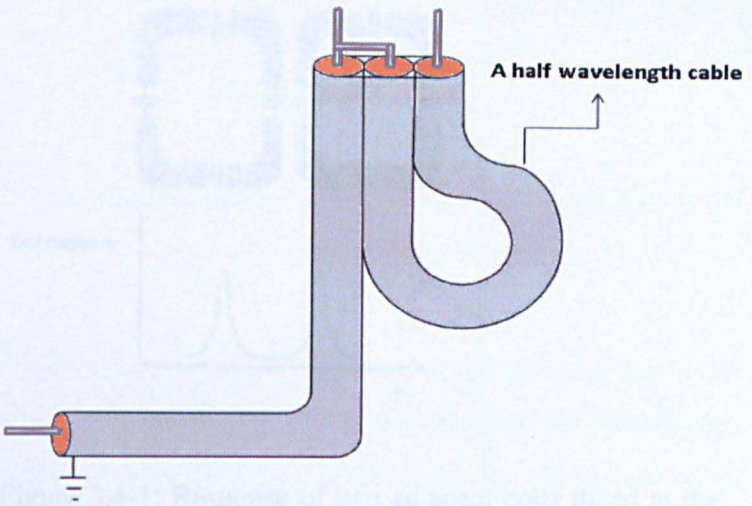

Figure 3.3-2: A balun consisting of a half wavelength coax cable.

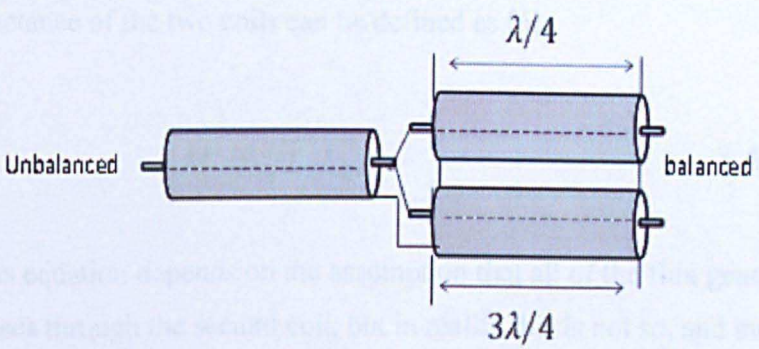

Figure 3.3-3: Balun circuit consists of quater and three quater wavelength.

3.4 Coupling and Decoupling

When two coils or more are placed near to each other and the coils are also tuned to the same resonant frequency, the mutual inductance of the coils will cause the resonant frequency to split into two peaks as shown in Figure 3.4-1. This will affect the coil operation, as the sensitivity of the probe at frequency f_0 is significantly decreased.

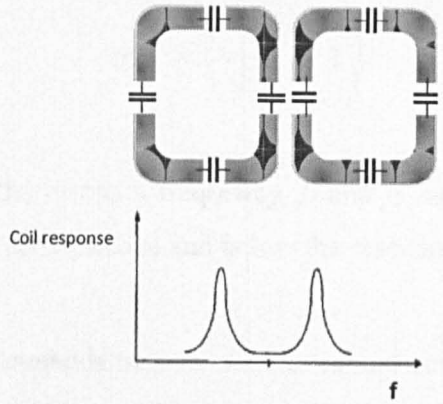

Figure 3.4-1: Response of two adjacent coils tuned at the same frequency, the frequency split into two peaks [5].

This is called coupling between the coils. It is a common problem and affects the operation of the coil array and disrupts it transmitting and receiving patterns. The mutual inductance of the two coils can be defined as [6]:

$$M = \sqrt{L_1 L_2}, \qquad 3.4.1$$

The previous equation depends on the assumption that all of the flux generated by one coil passes through the second coil, but in reality this is not so, and the mutual impedance should be less than that provided by the above equation. The mutual inductance (M) can be defined as a function of the coupling constant k and self inductance L_1 and L_2 of the coils

$$M_{12} = k\sqrt{L_1 L_2}, \qquad 3.4.2$$

Where k is the coupling coefficient and lies between $0 \leq k \leq 1$. The coupling constant k can be computed by using the equation:

$$\pm k = \left(\frac{f_o^2}{f_{1,2}^2} - 1 \right), \qquad 3.4.3$$

where f_o is the resonant frequency, f_1 and f_2 are the frequencies of the first and second split peaks, above and below the resonant frequency [7, 8].

Decoupling methods may be used to minimize the mutual inductance (M). Each method is based on a different principle and is used for different applications. Decoupling between neighbouring elements can be minimized using different methods such as overlapping elements, adding decoupling capacitors, adding inductors between the elements or connecting each element to a low input impedance preamplifier. The circular loop coils can be placed overlapping by 0.75 × their diameter and square loops coils by 0.9 × diameter [5] as shown in Figure 3.4-2. However, this does not always work so well at high frequencies.

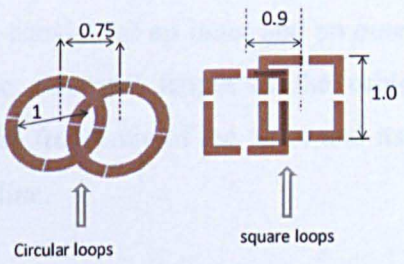

Figure 3.4-2: Mutual inductance reduces to zero by overlapping circular loops and square loop.

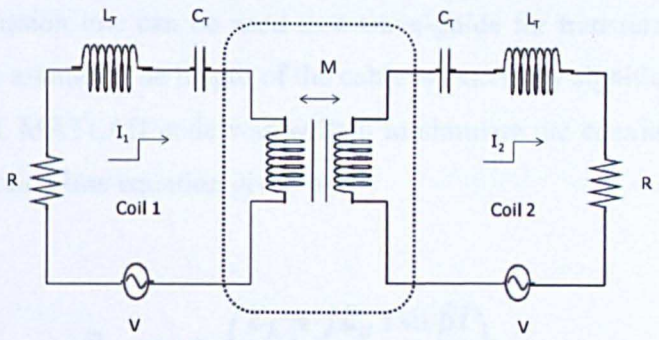

Figure 3.4-3: Mutual inductance created by two adjacent coils.

3.5 Coaxial Cable

The designers and builders of probes need to know about properties of transmission lines. In order to decouple elements using a low impedance preamplifier, the length of the cable is extremely critical. The aim of this section is to describe the behaviour of a coaxial cable. As shown in Figure 3.5-1 the coaxial cable consists of an inner and an outer conductor isolated by a dielectric insulator. The electrical length of the cable is measured in wavelength and depends on the frequency of the wave and its velocity as it propagates along the transmission line.

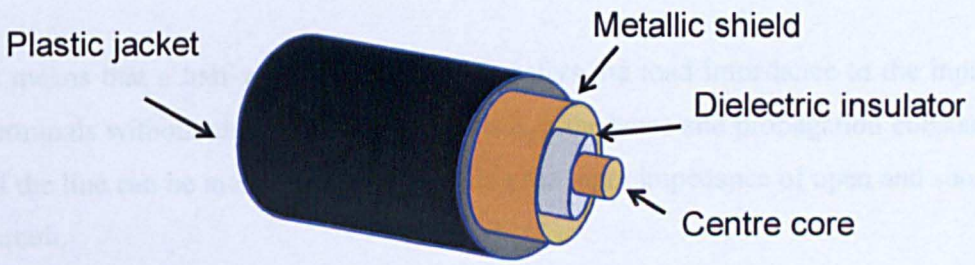

Figure 3.5-1: Schematic view of the coaxial cable, it has an inner conductor of radius a, and outer conductor of radius *b*, the spacing between the conductors has permittivity ε, permeability μ and conductivity σ.

The transmission line can be used as a wave-guide for transferring signals from one point to another. The length of the cable is extremely significant for matching impedances. MATLAB code was written to simulate the coaxial cable based on the transmission line equation given by:

$$Z_{in} = z_o\left(\frac{Z_L + jZ_o \tan \beta l}{Z_o + jZ_L \tan \beta l}\right), \qquad 3.5.1$$

Where Z_{in} is the input impedance of a lossless line of length l, z_L is the load impedance and $\beta = \frac{2\pi}{\lambda}$ is the phase constant of the line. The equation 3.5.1 can be considered as a half wave section ($l = \frac{\lambda}{2}, \beta l = \pi$), once the length of a line is an integral multiple of $\frac{\lambda}{2}$, $l = n\frac{\lambda}{2}$ $(n = 1,2,3,\ldots)$ [9].

$$\beta l = \frac{2\pi}{\lambda}\left(\frac{n\lambda}{2}\right) = n\pi. \qquad 3.5.2$$

So equation 3.5.1 reduces to:

$$z_{in} = z_L. \qquad 3.5.3$$

It means that a half-wave lossless line transfers the load impedance to the input terminals without change. The characteristic impedance and propagation constant of the line can be measured by determining the input impedance of open and short circuit.

$$z_o = \sqrt{z_{io} z_{is}}, \qquad 3.5.4$$

$$\gamma = \frac{1}{l} tanh^{-1} \sqrt{z_{is}/z_{io}}, \qquad 3.5.5$$

Where ($z_{io} = -jz_o \cot \beta l$) is the input impedance of an open circuit and ($z_{is} = jz_o \tan \beta l$) is the input impedance of a short circuit [10]. The line can be purely inductive or purely capacitive; relying on the value of βl. Transmission line parameters for a coax cable can be defined in the table below [3]:

Parameters	Coaxial cable	unit
R′	$\frac{R_s}{2\pi}(\frac{1}{a}+\frac{1}{b})$	Ohm/m
L′	$\frac{\mu}{2\pi}\ln(b/a)$	H/m
G′	$\frac{2\pi\sigma}{ln(b/a)}$	S/m
C′	$\frac{2\pi\varepsilon}{ln(b/a)}$	F/m

Where R', L', G' and C' are the resistance, inductance, conductance of insulation medium and capacitance per unit length respectively. A coax cable was simulated in MATLAB. The code was written to explain the properties of the cable as shown in Figure 3.5-2. This gave an idea of how the coaxial cable behaves. Figure 3.5-2 shows that a change in the length of cable causes a change in the reactance. Therefore, the input impedance of the cable can be either purely inductive or purely capacitive, depending on the value of βl. The code was written in MATLAB, the length of the cable is fixed at 68 cm while varying the frequencies. Equation 3.5.1 is used to compute the input impedance so the impedance can be calculated versus frequency as shown in Figure 3.5-3. At specific points, the input impedance of the cable should be equal the impedance of the capacitor.

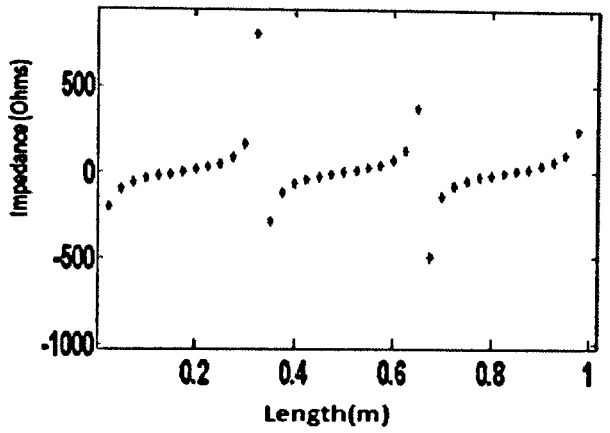

Figure 3.5-2: The input impedance of the transmission line versus with length of the cable.

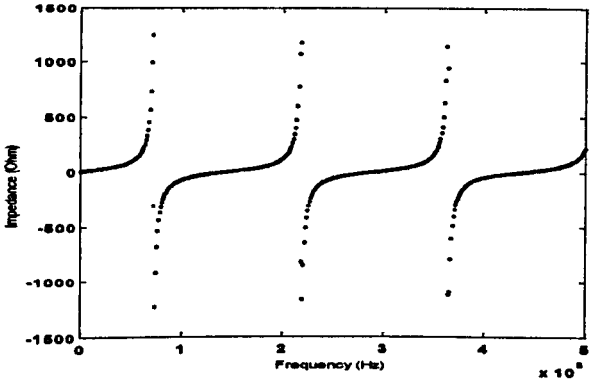

Figure 3.5-3: The input impedance versus with frequency.

3.6 Signal Noise Ratio (SNR)

Signal to noise ratio (SNR) is an important parameter and should be measured to determine performance of a probe. If the SNR is not high enough, it is very difficult to differentiate tissues from one another or from the background, which means a good coil design, should have a high SNR. We can obtain high SNR and high spatial resolution at a higher magnetic field strength B_0 because SNR is proportional to B_0. The spins inside the human body induce an *emf* at the coil, proportional to Larmor frequency, which depends on the strength of the magnetic field and also the coupling between the coil and the nuclei.

It was noted that the signal received from a small volume element is proportional to B_1 (B_1 is the field perpendicular to the static B_0 field, which is assumed to be along the z axis). SNR is proportional to the MRI signal and also depends on the voltage of the thermal noise of the probe. SNR can be defined based on Hoult and Richard's expression [11].

$$SNR \propto \frac{\omega_0^2 (B_1/i) V_{sample}}{R_{eff}}, \qquad 3.6.1$$

Where ω_o is the resonant frequency, V_{sample} is a small volume element (voxel), B_1 is the transverse linearly polarized magnetic field for unit current in the coil and R_{eff} is the effective resistance. It has contributions from the coil itself, electronics, and the sample or patient.

$$R_{eff} = \sqrt{R_{coil}^2 + R_{tissue}^2 + R_r^2}, \qquad 3.6.2$$

Where R_{coil}, R_{tissue} and R_r are resistance of the coil itself, coupled tissue losses, and radiation resistance respectively [12].

RF losses in MRI can be divided into tissue losses and coil losses. The latter can be divided into impedance losses to the coil itself R_{coil} and radiation losses R_r. The ohmic resistance of the probe consists of the real resistance of the probe conductor R_L and real capacitor loss R_C. Both of them dissipate RF power as heat in the probe circuit. The ohmic resistance at resonant frequency can be calculated by:

$$P_{\Omega\, loss} = \left(\frac{I^2}{2}\right) R_\Omega, \qquad 3.6.3$$

$$R_\Omega = R_L + R_C, \qquad 3.6.4$$

Radiation loss is considered as RF loss to the probe environment, a sample or the human body. Moreover, the radiated power can be calculated as the difference between the input power and ohmic losses in the probe:

$$P_{r\,loss} = P_{in} - (I^2/2)R_{\Omega}. \qquad 3.6.5$$

Tissue losses are caused by the B_1 field induced eddy currents in the tissue. It is very important to consider these losses because at a high frequency the probe becomes more important. Loss to the sample conductor or the tissue conductor increases with the frequency. This is potentially due to the tissue conductivity σ increasing with frequency, which generates eddy current $J_e = \sigma E = -j\omega\sigma\mathbf{A}$ and displacement current $J_d = -j\omega\varepsilon E = \omega^2\varepsilon\mathbf{A}$ [13].Where $\mathbf{A}$ is the vector potential which defines the magnetic field such that $\mathbf{B} = \nabla \times \mathbf{A}$.

The total power loss density P_{loss} can be determined by:

$$P_{Total\,loss} = 0.5 \int (J.J^*/\sigma)\, dv \qquad 3.6.6$$

$$for \quad J = J_e + J_d.$$

3.7 Noise

Note that the noise in the MRI signal is thermal noise produced in the probe and sample, and that the noise voltage in the circuit is proportional to the square root of the total resistance in the circuit. As a result, the noise is proportional to the square root of the power dissipated in the circuit. This is defined by the Nyquist formula [14].

$$R_{noise} = \sqrt{4k_B T \Delta f R_{coil}}, \qquad 3.7.1$$

Where k_B is the Boltzmann constant, T is the absolute temperature of the sample and Δf is the receiver frequency bandwidth. Hence, an efficient probe has low effective resistance either in transmit or receive mode.

3.8 Quality Factor (Q)

To determine the performance of any MRI coil, the quality factor should be measured. It has a number of definitions such as:

$$Q = 2\pi \frac{Maximum\ energy\ stored\ in\ magnetic\ field}{Energy\ dissipated\ per\ cycle}, \qquad 3.8.1$$

It can be shown that for a simple circuit, the quality factor is equal to the ratio of the reactive and resistive parts of the inductor impedance and is defined as

$$Q = \frac{2\pi f L}{R}, \qquad 3.8.2$$

Where f is resonant frequency, L is the inductance of the coil and R is the resistance of the coil. Note that the quality factor is proportional to the inductance of the coil and inversely proportional to the resistance of the coil.

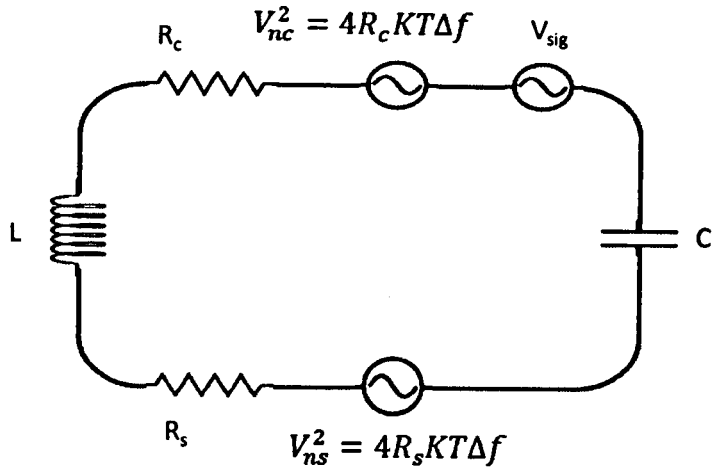

Figure 3.8-1: A circuit of sample loaded resonant loop, where V_{sig}, V_{ns} and V_{nc} are the detected MRI signal voltage, the noise voltage produced from the sample and the noise voltage generated from resistance of the coil respectively [15].

The ratio of the loaded to unloaded quality factor can be computed as [14]:

$$\frac{Q_L}{Q_U} = \frac{R_{Coil}}{R_{Coil} + R_{Sample}} . \qquad 3.8.3$$

It was found that the effective resistance of the probe when the sample or patient is under loaded conditions is more than when the probe is unloaded. This means that the quality factor will be very high when the coil is unloaded whereas it will decrease when the coil is loaded by a sample. Another factor that may decrease the quality factor is the resistance of the solder joints. It can be determined by cutting the resonant loop, then soldering it back together and calculating the change in the quality factor. The resistance is

$$R_{solder} = \omega L\left(\frac{1}{Q_2} - \frac{1}{Q_1}\right), \qquad 3.8.4$$

Where Q_1 and Q_2 are the quality factor Q before and after soldering. There is a simple approach used to compute Q according to the following expression

$$Q = \frac{f_o}{\Delta f}, \qquad 3.8.5$$

Where Δf is the bandwidth which the signal is at least half its amplitude and can be measured by using a network analyzer.

3.9 Power Efficiency

The power sensitivity of the unloaded and loaded coil, which requires generating field strength B_1 at a specific point, can be calculated by using the following equations [16]:

$$S_{Po} = \frac{B_1}{\sqrt{P_o}}, \qquad 3.9.1$$

$$S_{PI} = \frac{B_1}{\sqrt{P_p + P_o}} = S_{po}\sqrt{\frac{Q_I}{Q_o}}, \qquad 3.9.2$$

Where P_o is the power dissipated in the resistance R_o when the coil is empty and P_p is the power dissipated in the equivalent resistance R_p of the phantom or the human body.

The power efficiency of the coil η can be written as a function of the power sensitivity of the unloaded and loaded coil and also as a function of the quality factor

$$\eta = P_P/(P_P+P_o), \qquad 3.9.3$$

$$\eta = (L_F - 1)/L_F, \qquad 3.9.4$$

Where L_F is the ratio of unloaded and loaded quality factor. To obtain high power efficiency, we should increase L_F, which is affected by the design of the coil [17].

3.10 Specific Absorption Rate (SAR)

There is an energy transfer to a biological tissue when radiofrequency electromagnetic wave passes through the tissue. This causes an increase in the temperature of the region of interest and will result in heating of the tissue. Therefore, the Specific Absorption Rate (SAR) is a measurement of the energy that is dissipated in a biological sample. SAR can be defined as:

$$SAR = \frac{Total\ RF\ energy\ dissipated\ in\ sample\ (Joules)}{Exposure\ time(s).sample\ weight(Kg)}, \qquad 3.10.1$$

$$SAR = \frac{\sigma |E|^2}{\rho}, \qquad 3.10.2$$

Where σ is the conductivity of the tissue, E is the *r.m.s* electric field and ρ is mass density (kg/m^3) [18]. To acquire the whole body average SAR, the absorption rate in each cell should be calculated and divided by the mass of the whole body. When the SAR in the cell i is equal to S_i, the whole body average SAR can be computed based on the equation:

$$\overline{S} = \sum_{i=1}^{N} S_i \rho_i \left(\sum_{i=1}^{N} \rho_i\right)^{-1}, \qquad 3.10.3$$

Where N is the number of cells in the body [19].

In 2008 International Electrotechincal Commission (IEC) reported that the mass to determine the local SAR should be 10 grams. Table 3.10-1 shows ranges of values of whole body SAR, partial body SAR, and head SAR. For whole-body SAR, these values are valid at environmental below 24 °C but at high temperature the values should be reduced depending on the actual environmental temperature and humidity [20].

Table 3.10-1

Average time	6 min		
Body region	Whole body	Partial body SAR	Head
Operating mode	(W/kg)	(W/kg)	(W/kg)
normal	2	2-10[a]	3.2
First level controlled	4	4-10[a]	3.2
Second level controlled	>4	>(4-10[a])	>3.2

a The limit scales dynamically with the ratio "exposed patient mass/patient mass"
Normal operating mode:
Partial body SAR=10 W/kg-(8 W/kg* exposed patient mass/patient mass)
First level controlled operating mode:
Partial body SAR=10 W/kg-(6 W/kg* exposed patient mass/patient mass)
Second level controlled operating mode:
Partial body SAR=10 W/kg-(6 W/kg* exposed patient mass/patient mass)

3.11 Finite Difference Time Domain (FDTD) Method

The purpose of the next few sections is to describe the electromagnetic theory used in this research to model the behaviour of electromagnetic waves. The interaction of RF field with human anatomy can be modelled using the Finite Element (FE) method. In this research, the Finite Difference Time Domain Method (FDTD) is used for EM simulation. Kane Yee was the first researcher to publish the method in the original FDTD paper in 1966 [21]. The numerical Maxwell equations solutions are competed in this work by using the commercial XFDTD software package (Remcom Inc). This method can simulate the time varying magnetic and electric fields of exact geometry such as a surface coil and dipoles. It can also compute the magnetic flux density, electric field, current distribution and the Specific Absorption Rate (SAR). The calculated magnetic and electric fields are saved and used to determine B_1^+ and B_1^- by using additional MATLAB programs. The electric and magnetic fields are governed by a set of

four laws, known as Maxwell's equations. We can introduce these equations in integral and differential forms.

3.12 Maxwell's Equations in Three Dimensions

In the following pages, Maxwell's equations are expressed in terms of vector differential operators in the rectangular coordinate system. Gauss' law is one of Maxwell's equations for the electric field, which describes how the electric charge gives rise to an electric field and also that the total of electric flux out of a closed surface is equal to the net electric charge enclosed by that surface. This is shown by:

$$\oint \vec{E} \cdot d\vec{s} = \iiint \rho \, dv. \qquad 3.12.1$$

Gauss's law for the magnetic field describes the net magnetic flux out through a Gaussian surface is zero; which means that there are no isolated magnetic poles:

$$\oint \vec{B} \cdot d\vec{s} = 0. \qquad 3.12.2$$

Faraday's law of induction was discovered by Michael Faraday in 1831. It describes a varying magnetic flux induces an electric field, i.e. a time varying magnetic field gives rise to an electric field. Specifically, the electromotive force around a closed path is equal to the time rate of increase of the magnetic flux.

$$\oint \vec{E} \cdot d\vec{l} = -\frac{d\phi_B}{dt}, \qquad 3.12.3$$

Therefore, any change in the magnetic flux ϕ_B will induce an EMF. This law is the basis for electric generators. Ampere's law states that the integral line of **B** and *dl* around a closed path is μ_o multiplied by the current enclosed by that loop:

$$\oint \vec{B} . d\vec{l} = \mu_o i + \frac{1}{c^2}\frac{\partial}{\partial t}\oint \vec{E} . d\vec{s}. \qquad 3.12.4$$

Maxwell's equations in differential form can be written as follow:

$$\vec{\nabla} . \vec{D} = \rho, \qquad 3.12.5$$

$$\vec{\nabla} . \vec{B} = 0, \qquad 3.12.6$$

$$\vec{\nabla} \times \vec{E} = -\mu \frac{\partial \vec{H}}{\partial t}, \qquad 3.12.7$$

$$\vec{\nabla} \times \vec{H} = \sigma \vec{E} + \varepsilon \frac{\partial \vec{E}}{\partial t}. \qquad 3.12.8$$

These differential equations state that at any point in a given medium, the divergence of the displacement flux is equal to the volume charge density. The divergence of the magnetic flux density is equal to zero. The curl of the electric field is equal to the temporal derivative of the magnetic field intensity, and the curl of the magnetic field intensity is equal to the sum of current density (σ**E**) and the rate of change of the displacement flux density (ε**E**).

3.13 Converting Differential Vectors Equations to Differential Scalar Equations

The FDTD method is based on Faraday's and Ampere's laws and provides a system of equations that form an independent set of coupled relationships between time varying electric and magnetic fields. Therefore, differential vector equations can be converted into differential scalar equations as:

$$\vec{\nabla} \times \mathbf{E} = -\mu \frac{\partial \mathbf{H}}{\partial t}, \tag{3.13.1}$$

$$\vec{\nabla} = \frac{\partial}{\partial x}\,\hat{x} + \frac{\partial}{\partial y}\,\hat{y} + \frac{\partial}{\partial z}\,\hat{z}, \tag{3.13.2}$$

$$\mathbf{E} = E_x\,\hat{x} + E_y\,\hat{y} + E_z\,\hat{z}, \tag{3.13.3}$$

$$\begin{aligned}\vec{\nabla} \times \mathbf{E} = &\left(\frac{\partial E_z}{\partial y} - \frac{\partial E_y}{\partial z}\right)\hat{x} \\ &- \left(\frac{\partial E_z}{\partial x} - \frac{\partial E_x}{\partial z}\right)\hat{y} \\ &+ \left(\frac{\partial E_y}{\partial x} - \frac{\partial E_x}{\partial y}\right)\hat{z},\end{aligned} \tag{3.13.4}$$

$$\mathbf{H} = H_x\,\hat{x} + H_y\,\hat{y} + H_z\,\hat{z}, \tag{3.13.5}$$

$$\frac{\partial \mathbf{H}}{\partial t} = \frac{\partial H_x}{\partial t}\,\hat{x} + \frac{\partial H_y}{\partial t}\,\hat{y} + \frac{\partial H_z}{\partial t}\,\hat{z}, \tag{3.13.6}$$

$$\begin{aligned}-\mu \frac{\partial \mathbf{H}}{\partial t} = -\mu\Bigg(&\frac{\partial H_x}{\partial t}\,\hat{x} + \frac{\partial H_y}{\partial t}\,\hat{y} \\ &+ \frac{\partial H_z}{\partial t}\,\hat{z}\Bigg),\end{aligned} \tag{3.13.7}$$

Now, comparing equation 3.13.4 and 3.13.6 equation and three differential scalar equations can be written as the follows:

$$\left(\frac{\partial E_z}{\partial y} - \frac{\partial E_y}{\partial z}\right) = -\mu \frac{\partial Hx}{\partial t}, \qquad 3.13.8$$

$$\left(\frac{\partial E_x}{\partial z} - \frac{\partial E_z}{\partial x}\right) = -\mu \frac{\partial Hy}{\partial t}, \qquad 3.13.9$$

$$\left(\frac{\partial E_y}{\partial x} - \frac{\partial E_x}{\partial y}\right) \hat{z} = -\mu \frac{\partial Hz}{\partial t}, \qquad 3.13.10$$

$$\begin{aligned} \vec{\nabla} \times \mathbf{H} = & \left(\frac{\partial H_z}{\partial y} - \frac{\partial H_y}{\partial z}\right) \hat{x} \\ & - \left(\frac{\partial H_z}{\partial x} - \frac{\partial H_x}{\partial z}\right) \hat{y} \\ & + \left(\frac{\partial H_y}{\partial x} - \frac{\partial H_x}{\partial y}\right) \hat{z}, \end{aligned} \qquad 3.13.11$$

$$\begin{aligned} \sigma \mathbf{E} + \varepsilon \frac{\partial \mathbf{E}}{\partial t} & \\ & = \sigma E_x \hat{x} + \sigma E_y \hat{y} + \sigma E_z \hat{z} \\ & + \epsilon \frac{\partial E_x}{\partial t} \hat{x} + \epsilon \frac{\partial E_y}{\partial t} \hat{y} \\ & + \epsilon \frac{\partial E_z}{\partial t} \hat{z}, \end{aligned} \qquad 3.13.12$$

$$\frac{\partial E_x}{\partial t} = \frac{1}{\varepsilon}\left[\left(\frac{\partial H_z}{\partial y} - \frac{\partial H_y}{\partial z}\right) - \sigma E_x\right], \qquad 3.13.13$$

$$\frac{\partial E_y}{\partial t} = \frac{1}{\varepsilon}\left[\left(\frac{\partial H_x}{\partial z} - \frac{\partial H_z}{\partial x}\right) - \sigma E_y\right], \qquad 3.13.14$$

$$\frac{\partial E_z}{\partial t} = \frac{1}{\varepsilon}\left[\left(\frac{\partial H_y}{\partial x} - \frac{\partial H_x}{\partial y}\right) - \sigma E_z\right], \qquad 3.13.15$$

Where μ is the permeability, ε is the permittivity and σ is the conductivity of the medium.

The current density **J** can be defined as σ.**E**, where **E** is a vector in three dimensions. Hence the total current density can also be written as: $\mathbf{J} = \sigma_x E_x \hat{x} + \sigma_y E_y \hat{y} + \sigma_z E_z \hat{z}$. In our simulations of tissue, σ is considered isotropic so can be reduced to a scalar quantity.

3.14 Yee Cell

The Yee cell is used for the FDTD method, which can be used for very complicated, inhomogeneous dielectric structures. It is a computer modelling technique applied to simulate Maxwell's equations, and it was introduced by Kane S. Yee in 1966. It is based on Maxwell's curl equations, and Figure 3.14-1 shows the standard Yee cell. Each cell has six field components: three electric fields E_x, E_y and E_z and three magnetic fields H_x, H_y and H_z in x, y and z directions. Note that the electric fields are along edges and magnetic fields are through the cell surface. The diagram below shows that the **H** field is offset by half a cell from the **E** field:

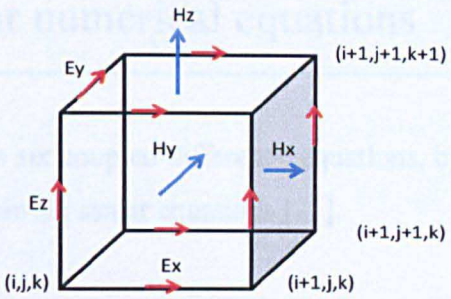

Figure 3.14-1: The standard Yee cell and arrangement of field components (Electric fields **E** and magnetic fields **H**).

The grid coordinates of the space can be described as $(i, j, k) = (i\,\Delta x, j\,\Delta y, k\,\Delta z)$, where Δx is the dimensions of the cell in x direction, Δy is the dimensions of the cell in y direction, and Δz is the dimensions of the cell in z direction. We apply central finite difference, which is an approximation of mathematical expression that is used to convert differential equations to numerical equations. Any function of space and time is written as $\mathbf{F}(i\,\Delta x, j\,\Delta y, k\,\Delta z, n\,\Delta t) = \mathbf{F}n\,(i, j, k)$, where n is the number of time steps. Function **F** can be written by using central finite difference approximation:

$$\frac{\partial \mathbf{F}^n(i,j\,k)}{\partial x} = \frac{\mathbf{F}^n(i+1/2,j,k) - F^n(i-1/2,j,k)}{\delta}, \qquad 3.14.1$$

$$\frac{\partial \mathbf{F}^n(i,j,k)}{\partial t} = \frac{\mathbf{F}^{n+\frac{1}{2}}(i,j,k) - \mathbf{F}^{n-\frac{1}{2}}(i,j,k)}{\Delta t}. \qquad 3.14.2$$

we can obtain six coupled difference equations, by applying equations 3.14.1 and 3.14.2 to obtain six scalar equations [21].

$$
\begin{aligned}
&{E_x}^{n+1}\left(i+\frac{1}{2},j,k\right)\\
&\quad = A_{i+\frac{1}{2},j,k}{E_x}^{n}\left(i+\frac{1}{2},j,k\right)\\
&\quad + B_{i+\frac{1}{2},j,k}\left[{H_z}^{n+\frac{1}{2}}\left(i+\frac{1}{2},j+\frac{1}{2},k\right)\right.\\
&\quad - {H_z}^{n+\frac{1}{2}}\left(i+\frac{1}{2},j-\frac{1}{2},k\right)\\
&\quad + {H_y}^{n+\frac{1}{2}}\left(i+\frac{1}{2},j,k-\frac{1}{2}\right)\\
&\quad \left. - {H_y}^{n+\frac{1}{2}}\left(i+\frac{1}{2},j,k+\frac{1}{2}\right)\right],
\end{aligned}
\qquad 3.14.3
$$

$$
\begin{aligned}
&{E_y}^{n+1}(i,j+1/2,k)\\
&\quad = A_{i,j+\frac{1}{2},k}{E_y}^{n}\left(i,j+\frac{1}{2},k\right)\\
&\quad + B_{i,j+\frac{1}{2},k}[{H_x}^{n+\frac{1}{2}}\left(i,j+\frac{1}{2},k+\frac{1}{2}\right)\\
&\quad - {H_x}^{n+\frac{1}{2}}\left(i,j+\frac{1}{2},k-\frac{1}{2}\right)\\
&\quad + {H_z}^{n+\frac{1}{2}}\left(i-\frac{1}{2},j+\frac{1}{2},k\right)\\
&\quad - {H_z}^{n+\frac{1}{2}}\left(i+\frac{1}{2},j+\frac{1}{2},k\right),
\end{aligned}
\qquad 3.14.4
$$

$$E_z{}^{n+1}(i,j,k+1/2) = A_{i,j,k+\frac{1}{2}} E_z{}^{n}\left(i,j,k+\right.$$

$$12+Bi,j,k+12Hyn+12i+12,j,k+12-Hyn+12i$$

$$-12,j,k+12+Hxn+12i,j-12,k+12-Hxn+12i,$$

$$j+12,k+12, \qquad 3.14.5$$

$$H_x{}^{n+\frac{1}{2}}\left(i,j+\frac{1}{2},k+\frac{1}{2}\right) = H_x{}^{n-\frac{1}{2}}\left(i,j+\frac{1}{2},k+\right.$$

$$12+\Delta t\mu\delta$$

$$[E_y{}^{n}\left(i,j+\frac{1}{2},k+1\right) - E_y{}^{n}\left(i,j+\frac{1}{2},k\right)+$$

$$E_z{}^{n}\left(i,j,k+\frac{1}{2}\right) - E_z{}^{n}\left(i,j+1,k+\frac{1}{2}\right), \qquad 3.14.6$$

$$H_y{}^{n+\frac{1}{2}}\left(i+\frac{1}{2},j,k+\frac{1}{2}\right) = H_y{}^{n-\frac{1}{2}}\left(i+\frac{1}{2},j,k+\right.$$

$$12+\Delta t\mu\delta$$

$$[E_z{}^{n}\left(i+1,j,k+\frac{1}{2}\right) - E_z{}^{n}\left(i,j,k+\frac{1}{2}\right)+ \qquad 3.14.7$$

$$E_x{}^{n}\left(i+\frac{1}{2},j,k\right) - E_x{}^{n}\left(i+\frac{1}{2},j,k+1\right)].$$

$$H_z{}^{n+\frac{1}{2}}\left(i+\frac{1}{2},j+\frac{1}{2},k\right) = H_z{}^{n-\frac{1}{2}}\left(i+\frac{1}{2},j+\right.$$

$$12,k+\Delta t\mu\delta$$

$$[E_x{}^{n}\left(i+\frac{1}{2},j+1,k\right) - E_x{}^{n}\left(i+\frac{1}{2},j,k\right)+$$

$$E_y{}^{n}\left(i,j+\frac{1}{2},k\right) - E_y{}^{n}\left(i+1,j+\frac{1}{2},k\right), \qquad 3.14.8$$

Where A and B are defined as - $A(i,j,k) = 1 - \frac{\sigma(i,j,k)}{\varepsilon(i,j,k)}$, $B(i,j,k) = \frac{\Delta t}{\varepsilon(i,j,k)\delta}$

$\varepsilon(i,j,k)$ is the effective permittivity of the medium and σ is the conductivity [22]. By using these equations and applying the boundary conditions, all field components E_x, E_y, E_z, H_x, H_y and H_z are calculated in each time step Δt. And also

the input power can be calculated by using the following integration equation [23].

$$P_{input} = P_{abs} + P_{rad} = \iiint \frac{\sigma(\vec{r})}{2} |\mathbf{E}|^2 dV + \frac{1}{2} \iint (\mathbf{E} \times \mathbf{H})\, ds, \qquad 3.14.9$$

Where P_{abs} and P_{rad} are the absorbed and radiated power, **E** is the electric field; **H** is the magnetic field, $\vec{r}$ is the coordinates of the pixel in FDTD and $\sigma(\vec{r})$ is the conductivity of each cell. The absorbed power in the human body relies on a value of conductivity for each type of tissue. The absorbed power in tissue is extremely significant and can be computed numerically by changing the integration to the summation of each FDTD grid as follows:

$$P_{abs} = \sum_{i,j,k} \left(\frac{\sigma(i,j,k)}{2} \times \left(E^2_{x(i,j,k)} + E^2_{y(i,j,k)} + E^2_{z(i,j,k)} \right) \Delta x \Delta y \Delta z, \right. \qquad 3.14.10$$

Where $\sigma(i,j,k)$ the conductivity of each cell is at the (i,j,k) location in the x, y and z directions.

3.15 Poynting Vector

The time average Poynting vector can be obtained by using equation below

$$S_{av} = \frac{1}{2} R_e(\mathbf{E} \times \mathbf{H}^*), \qquad 3.15.1$$

Where **E** and **H** are the electric and magnetic fields respectively [24]. The Poynting vector can be computed pixel by pixel from the **E** and **H** fields using

MATLABE code. The following equation calculates the Poynting vector in three dimensions x, y and z. where **E** is the electric field and **H** is the magnetic field.

$$\mathbf{S}=(E_y H_z - E_z H_y)\, i-(E_x H_z - E_z H_x)\, j+(E_x H_y - E_y H_x)\, k, \quad 3.15.2$$

$$S_x=(E_y H_z - E_z H_y), \quad 3.15.3$$

$$S_y=(E_z H_x - E_x H_z), \quad 3.15.4$$

$$S_z=(E_x H_y - E_y H_x), \quad 3.15.5$$

$$\mathbf{S}=(S_x i+S_y j+ S_z k), \quad 3.15.6$$

$$S = \sqrt{s_x^2 + s_y^2 + s_z^2}. \quad 3.15.7$$

3.16 Grid Size and Stability

The grid size is extremely significant in the FDTD technique. To obtain accurate results the grid spacing $\Delta x, \Delta y,$ and Δz should be less than the wavelength. Usually is $\lambda/10$ used to excite the model [25]. Therefore, the maximum cell size may be determined by

$$L_{max} = \frac{c}{10 * f}, \quad 3.16.1$$

Where L_{max} is the maximum cell dimension, c is the speed of light in the vacuum defined as $C = C_\circ = {}^{1}/_{\sqrt{\mu_\circ \times \varepsilon_\circ}} = 3 \times 10^8 m/s$, the speed of light in a material medium is $C = {}^{1}/_{\sqrt{\mu \times \varepsilon}}$ and f is the frequency of excitation (Hz). The equation shows that if material is included in the computation in this case, the speed of light will be decreased in the material, which would lead to a reduction

of the FDTD cell size. The time step Δt can be calculated using the following equation, which is a function of the cell size in x, y and z directions and speed of light in medium [26]:

$$\Delta t \leq \frac{1}{c\sqrt{1/\Delta x^2 + 1/\Delta y^2 + 1/\Delta z^2}}, \qquad 3.16.2$$

This is called Courant condition and can be computed in one dimension written as $c\,\Delta t \leq \Delta x$. The time needed for the field to travel from nth to the $(n+1)$th node is a time step $\Delta t > (\Delta x/c)$.

3.17 Brief Description of XFDTD

Development and improvement of MRI systems needs powerful software to optimize any coil design. Several techniques have been used for modelling electromagnetic waves such as the method of moment and FDTD. It is a three dimensional full-wave electromagnetic analysis. It is based on the Finite Difference Time Domain method. FDTD is capable of simulating a wide variety of electric and magnetic materials in different shapes. We have used XFDTD by Remcom extensively in this project.

There are four main steps required to create a simulation in XFDTD. The first stage in any XFDTD simulation is to create the geometry. We must construct an object that represents a real device in the software in solid mode. This mode shows all the features of the object as a three dimensional object in x, y and z co-ordinates. Secondly, the mesh mode is used to create the mesh *i.e* the Yee cells. The third step is defining the run parameters. There are a wide variety of excitations such as voltage and current sources in XFDTD. The final step is requesting results such as electric fields, magnetic fields in x, y, and z directions, specific absorption rate (SAR) etc.

3.18 Electric Properties of Biological Material

The dielectric properties of materials can be obtained and determined from complex relative permittivity ε:

$$\varepsilon = \varepsilon' - j\,\varepsilon'', \qquad 3.18.1$$

Where ε' is the relative permittivity of the material and ε'' is the out phase loss factor $\varepsilon'' = {}^{\sigma}/_{(\varepsilon_o \omega)}$ the dielectric properties are calculated using σ, ε' and ε'' and these values are function of frequency [27].

3.19 High Field Effects

The effects of electromagnetic propagation in dielectric materials such as human tissue have been studied. The image quality in MRI depends on the homogeneity of the time varying electromagnetic field B_1. There are many parameters that affect the homogeneity of the magnetic field. The first parameter is RF penetration which affected at higher frequencies [28]. Reduced penetration depth at high frequencies such as 300 MHz is shown in Figure 3.19-4. The Larmor wavelength becomes considerably shorter in dielectric tissue. The calculation to find the value of wavelength in muscle and uterus tissue is based on this relation:

$$\lambda_{tissue} \propto \frac{1}{\sqrt{\varepsilon_r}} \lambda_{free\ space}, \qquad 3.19.1$$

Where ε_r is the relative permittivity. It can be said that as the electromagnetic field is attenuated, some of the energy is converted into heat due to conduction in the medium as the wave travels through a distance δ:

$$\delta = \frac{1}{\alpha}. \qquad 3.19.2$$

Some of the propagation parameters for many types of media can be summarized as lossless medium, low loss medium and good conductor [3].

Any medium	Lossless medium	Low loss medium	Good conductor
$\alpha = \omega\left\{\frac{\mu\varepsilon'}{2}\left[\sqrt{1+(\frac{\varepsilon'}{\varepsilon''})^2}\right]-\frac{\mu\varepsilon'}{2}\right\}^{1/2}$	0	$\frac{\sigma}{2}\sqrt{\frac{\mu}{\varepsilon}}$	$\sqrt{\pi f\mu\sigma}$
$\beta = \omega\left\{\frac{\mu\varepsilon'}{2}\left[\sqrt{1+(\frac{\varepsilon'}{\varepsilon''})^2}+1\right]+\frac{\mu\varepsilon'}{2}\right\}^{1/2}$	$\omega\sqrt{\mu\varepsilon}$	$\omega\sqrt{\mu\varepsilon}$	$\sqrt{\pi f\mu\sigma}$

The wavelength in water was computed at 128 MHz (3T) and 300 MHz (7T) as about 27 cm and 12 cm respectively [13]. The wavelength reduces by increasing the static magnetic field strength for MRI as shown in Figure 3.19-1. Therefore, interference patterns arise, which may cause inhomogeneity. It is very important to know that magnetic field homogeneity will be affected when designing and building RF coils at ultra high frequency. By Comparing Figure 3.19-2 and Figure 3.19-3, it can be seen that the conductivity increases with frequency, while the relative permittivity decreases with frequency. Figure 3.19-2 and Figure 3.19-3 demonstrate that muscle and uterus tissues are affected by increasing the frequency from low frequency at 64 MHz to 300MHz (7T). The conductivity and relative permittivity of each muscle tissue was calculated based on the database that was published by the Italian National Research Council [29]. The calculations show that there is a huge difference between these values in different magnetic fields. As static magnetic field increases, the conductivity of tissue will increase as well. This leads to induced currents, which produce magnetic fields, inducing an opposing EMF in the probe.

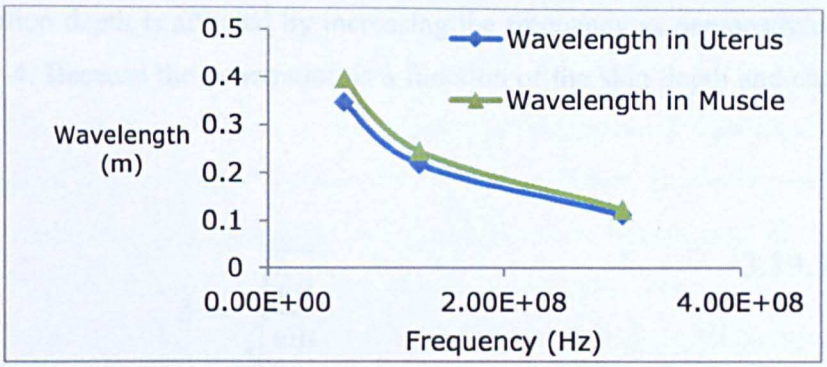

Figure 3.19-1: The wavelengths propagate in muscle and uterus reduces with increasing frequency.

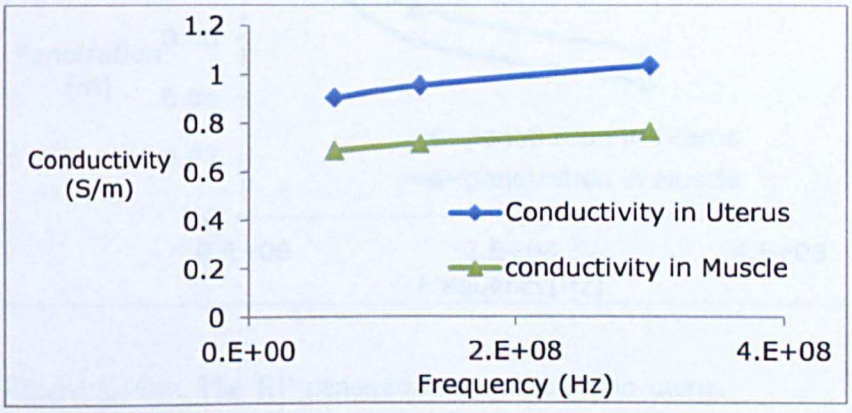

Figure 3.19-2: The conductivity of muscle and uterus increases with increasing frequency.

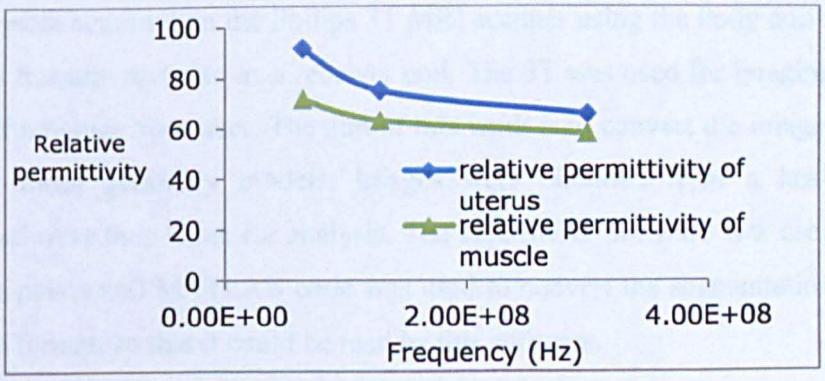

Figure 3.19-3: The relative permittivity of muscle and uterus decrease with increasing frequency.

The penetration depth is affected by increasing the frequency as demonstrated in Figure 3.19-4. Because the penetration is a function of the skin depth and can be defined as:

$$\delta = \sqrt{\frac{2\rho}{\omega\mu}}, \qquad 3.19.3$$

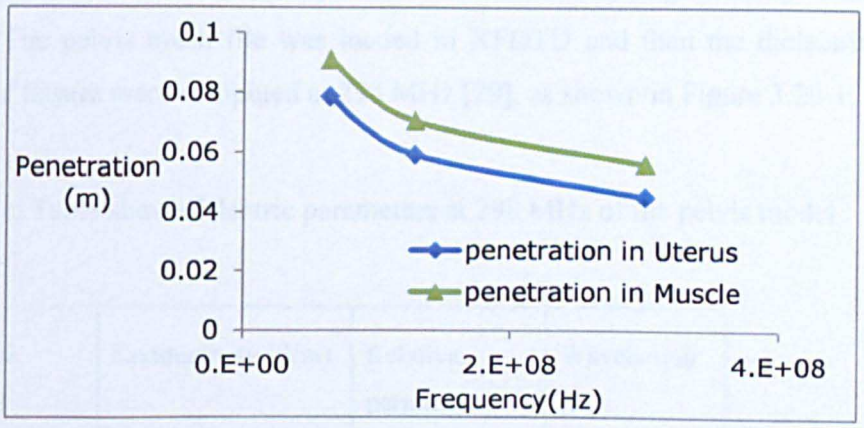

Figure 3.19-4: The RF penetration in muscle and uterus reduce with increasing frequency.

3.20 Image Segmentation

Image data were acquired on the Philips 3T MRI scanner using the body coil that functions as transmit and also as a receiver coil. The 3T was used for imaging of the pelvis of a human volunteer. The aim of this work is to convert the images to comparable mesh geometry models. Images were obtained from a healthy volunteer and were then taken for analysis. The ITK-SNAP software was used to segment the pelvis and MATLAB code was used to convert the segmentation to XFDTD file format, so that it could be read by this software.

A dielectric patient pelvis model was generated by dividing the healthy pelvis tissues into the most important dielectric tissue types such as fat, muscle, bladder, and inner air. The dielectric pelvis model was scaled to a $3 \times 3 \times 3\ mm^3$ cubic

grid. It can be said that a model resolution of $(3\ mm)^3$ provides a good detailed description of the pelvis anatomy and the boundaries can also be seen with high contrast. A high resolution model is needed to consider such as transverse B_1^+ variations and electric fields [30]. Using this model, valuable information will be acquired examples of interaction of RF with the pelvis and calculation of the SAR. There are two main parameters of biological material used, which are conductivity and permittivity. Electrical measurement of electrical properties in human tissue is a very complicated problem because of tissue inhomogeneity; the dielectric constant and conductivity of most media vary significantly with frequency. The pelvis mesh file was loaded in XFDTD and then the dielectric properties of tissues were computed at 298 MHz [29], as shown in Figure 3.20-1.

Table 3.20-1: Table show dielectric parameters at 298 MHz of the pelvis model.

Tissue name	Conductivity (S/m)	Relative permittivity	Wavelength (m)
Bladder	0.316	20.01	0.205
Fat	0.039	5.63	0.414
Muscle	0.77	58.23	0.123

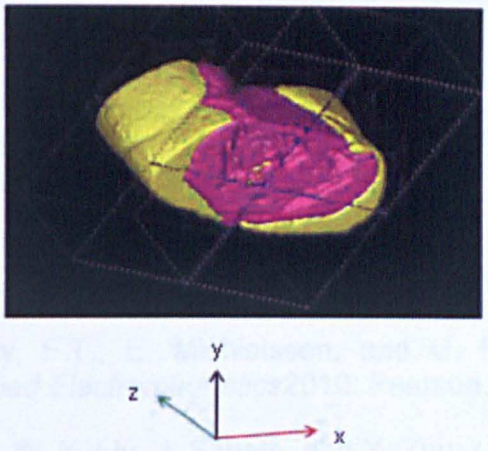

Figure 3.20-1: The segmentation of the pelvis model.

The purpose of making the pelvis model is to use it when we need to compute the distribution of B_1^+ and SAR. The dielectric pelvis model will be loaded into the coils and this be seen in modelling RF coils such as loop, strip line and dipoles in the next chapters.

References:

1. Andris, P. and I. Frollo, *Matching of RF Coils for NMR Measurements Using Inductors.* MEASUREMENT SCIENCE REVIEW, 2003. **3**.

2. Andris, P., *Matching and Tuning Rf Coils for NMR Tomograph.* MEASUREMENT SCIENCE REVIEW, 2001. **1**: p. 115-118.

3. Ulaby, F.T., E. Michielssen, and U. Ravaioli, *Fundamentals of Applied Electromagnetics*2010: Pearson.

4. Chu, X., Y. Liu, J. Sabate, and Y. Zhu, *Ultra-low Output Impedance RF Power Amplifier Array.* Magnetic Resonace in Medicine, 2009. **61**: p. 952-961.

5. ROEMER, P.B., P.S. Souza, and O.M. Mueller, *The NMR Phased Array.* MAGNETIC RESONANCE IN MEDICINE, 1990. **16**: p. 192-225.

6. Tomanek, B. and J.K. Saunders, *Dual Surface Coil with High-B1 Homogeneity for Deep Organ MR Imaging.* Magnetic Resonace Imaging, 1997. **15**: p. 1199-1204.

7. Lee, D., *Radio Frequency Probes for Ultra-High Field Magnetic Resonance Imaging*, in *Physics*2011, Nottingham.

8. Wei, J., J. Yuan, and G.X. Shen, *Effect of Tuning Capacitor Placement on Mutual Coupling for MRI Array Coils.* Magnetic Resonace Engineering, 2006. **29B**(1).

9. Cheng, D.K., *Field and Wave Electromagnetics*1989: Addison-Wesley.

10. Vaughan, J.T., H.P. Hetherington, O. Joe, and G.M. Pohost, *High Frequency Volume Coils for Clinical NMR Imaging and Spectroscopy.* Magnetic Resonance in Medicine, 2005. **32**(2): p. 206-218.

11. Hernandez, R., A. Rodriguez, P. Salgado, and F. Barrios, *Concentic dual loop RF coil for magnetic resonance imaging.* Revista Mexicana De FISCA, 2003. **49**(2): p. 107-114.

12. Hayes, C.E. and L. Axel, *Noise performance of surface coils for magnetic resonance imaging at 1.5 T.* Med. Phys., 1985. **12**: p. 604-607.

13. Robitaille, P.M. and L.J. Berliner, *Ultra high field Magnetic Resonance Imaging*2006, USA: Springer Science

14. Wright, A.C., H.K. Song, and F.W. Wehrli, *In Vivo MR Micro Imaging With Conventional Radiofrequency Coils Cooled to 77°K.* Magnetic Resonance in Medicine, 2000. **43**: p. 163–169.

15. Kumar, A., W.A. Edelstein, and P.A. Bottomley, *Noise Figure Limits for Circular Loop MRI Coils.* Magnetic Resonance in Medicine, 2009. **61**: p. 1201–1209.

16. Giulio, G. and A. Benassi, *Conductor Geometry and Capcitor Quality for Performace Optimization of Low-Frequency Birdcage Coils.* Magnetic Resonace, 2004. **26**: p. 9-16.

17. Vernickel, P., P. Roschmann, C. Findeklee, K.M. Ludeke, J. Overweg, U. Katscher, J. Grasslin, and K. Schunemann, *Eight-channel transmit/receive body MRI coil at 3T.* Magnetic Resonance in Medicine, 2007. **58**: p. 381–389.

18. Saunders, R. and C. Kowalczuk, *Biological effects of electromagnetic fields and radiation.* Radiology, 1991. **11**: p. 27-42.

19. Dimbylow, P.J., *FDTD calculations of the whole-body averaged SAR in an anatomically realistic voxel model of the human body from 1 MHz to 1 GHz.* Phys. Med. Biol., 1997. **42**: p. 479–490.

20. (IEC), I.E.C., *Medical electric equipment, Par 2-33: Particular requirements for the safety of magnetic resonance equipment for medical diagnosis*, 2008.

21. Yee, K.S., *Numerical solution of initial boundary value problems involving Maxwell's equations in Isotropic media.* IEEE, 1966. **14**: p. 802-807.

22. Chen, J., Z. Feng, and J.M. Jin, *Numerical Simulation of SAR and B1 Field Inhomogeneity of Shielded RF Coils Loaded with the Human Head.* IEEE TRANSACTIONS ON BIOMEDICAL ENGINEERING, 1998. **45**(5): p. 650-659.

23. Tang, L. and T.S. Ibrahim, *On the Radio-frequency Power Requirements of Human MRI.* PIERS ONLINE, 2007. **3**: p. 886-889.

24. Webb, A.G., C.M. Collins, M.J. Versluis, and N.B. Smith, *MRI and Localized Proton Spectroscopy in Human Leg Muscle at 7 Tesla Using Longitudinal Traveling Waves.* MAgnetic Resonance Med., 2010. **63**(2): p. 297-302.

25. Lutlf, E.Y., M.R. Gontijo, A.J. Orlando, and A.C. Migllano, *FDTD Analysis in a PCB Stripline Structure.* PIERS Proceedings, cambridge, 2010.

26. Yu, W., X. Yang, Y. Liu, and R. Mittra, *Electromagnetic Simulation Techniques Based on the FDTD Method*2009, New Jersey: John Wiley and Sons, Inc. .

27. Gabriel, C., S. Gabrriel, and E. Corthout, *The dielectric properties of biological tissues.* Phys. Med. Biol., 1996. **41**: p. 2231-2249.

28. Thomas, K.F., C. Hayes, and N.W. Kang, *Reduction of RF Penetration Effects in High Field Imaging.* magnetic resonanc in Medicine 1992. **23**: p. 287-301.

29. Andreuccetti, D., R. Fossi, and C. Petrucci. *Dielectric Properties of Body Tissues.* 2012 [cited 2012; Available from: http://niremf.ifac.cnr.it/tissprop/htmlclie/htmlclie.htm#atsftag.

30. Cornelis, A.T., L.W. Bartels, L.W. Bartels, B. Bergen, H. Kroeze, A.C. de Leeuw, B. Jeroen, and J. Lagendijk, *The use of MR B+1 imaging for validation of FDTD electromagnetic simulations of human anatomies.* Phys. Med. Biol., 2006. **51**: p. 4735–4746.

Chapter 4

The Wrist Coil

4 Introduction

In this chapter, an RF probe suitable for multichannel receive operating at 298 MHz has been simulated and built. The performance of the coil was demonstrated for high-resolution *in vivo* applications and was tested on the 7 T for wrist imaging.

There are many examples of multi-receiver probes that have been designed for field strengths in the range of 1.5 T to 3 T. However, there are fewer that have been designed for use at 7T, which can provide higher SNR and better spatial resolution such enhancements bring further clinical benefits [1, 2]. Modelling of the coil is carried out and design methodologies are reported. A one element coil detects signals only in very close proximity to the sample. By adding more than one element, the coil can pick up signals from a wider area surrounding the region of interest. The SNR intensity will be higher in regions of proximity. In simulations the image intensity shows a variation as a function of position, even for a uniform phantom. To show how this can be achieved, we simulated one and then two-element receive coils.

4.1 Simulation

We used the simulation to develop a new probe geometry that can be used to scan a human wrist. All simulations were performed using XFDTD (Remcom). Each element was simulated independently. In addition both elements were simulated

close to each other and loaded with a cylindrical phantom, which had properties (conductivity, relative permittivity) similar to that of human muscle tissue. Dielectric properties were computed at 298 MHz, which have been reported by the Italian National Research Council [3]. The coil consisted of two identical elements, each of which consisted of eight tuning capacitors.

Research in this field has noted that the sample and human tissue (dielectric) have the effect of decreasing the quality factor and the coil sensitivity. This is due to parasitic capacitance appearing between the ground through the sample dielectric and the probe [4]. These capacitors appear in parallel with the coil tuning capacitor as shown in Figure 4.2-1 [5]. This effect can be measured and noted by comparing different quality factors with different loads. The finite conductivity of the sample contributes to the losses in the coil.

4.2 Simulation of a One Element and Two Elements Wrist Coil

In this section we present a small search loop coil that was used to simulate and excite the tuned circuits. The search loop coil is one of the key challenges that was used in this study. It becomes an equivalent to the signals that are detected from the spins to generate electromotive force (EMF) in each element. The search loop coil will induce the current on the receiver and then receiver produces the electromagnetic fields. The fields in each cell will be used to generate B_1^-, and hence a measurement of the coil sensitivity.

With regard to Faraday's law, a time varying magnetic field will induce an electric current. The loop will excite the element to generate a current to produce magnetic field, which means that the small loop coil will act as a transformer that transfers electrical energy from the search loop coil to the main receiver through inductively coupled conductors (PEC in the simulation). Varying magnetic field induces a varying EMF or voltage in the receiver.

In this chapter we present a two element receiver coil, it was simulated as shown in Figure 4.2-2, by exciting two circuits as shown in Figure 4.2-4. The coil strips

were simulated using a Perfect Electric Conductor (PEC) in XFDTD. The coil was driven with a Gaussian pulse as the source waveform to provide a wide bandwidth frequency response. The simulation was run using the Gaussian pulse to determine the resonant frequency of the coils; the coil resonated at 300 MHz by varying the values of the capacitors. There was no appearance of coupling in the spectrum, because the mutual inductance was very small and it was not enough to split the main peak into two peaks. However, as we will see in the coil construction section, coupling appeared in the electronic laboratory when two elements were placed close to each other and connected to the network analyzer.

Each element was tuned at 300 MHz, by allowing the current to flow in the circuit that consisted of eight tuning capacitors. Therefore, a small loop will induce a current that flows in each element. The first element was tuned but the second element acted as an open circuit. It means that high impedance was produced in the second element, which prevented the current flow in this element.

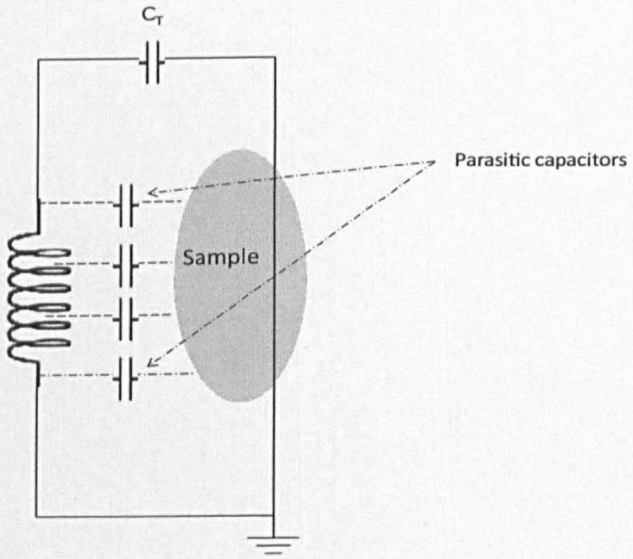

Figure 4.2-1: The parasitic capacitance introduced between the coil and a conductive sample.

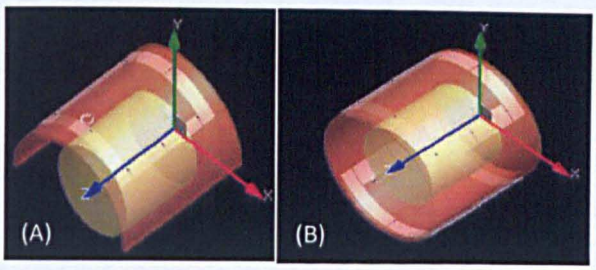

Figure 4.2-2: (A) A single element structure in XFDTD and (B) the two-element structure in XFDTD.

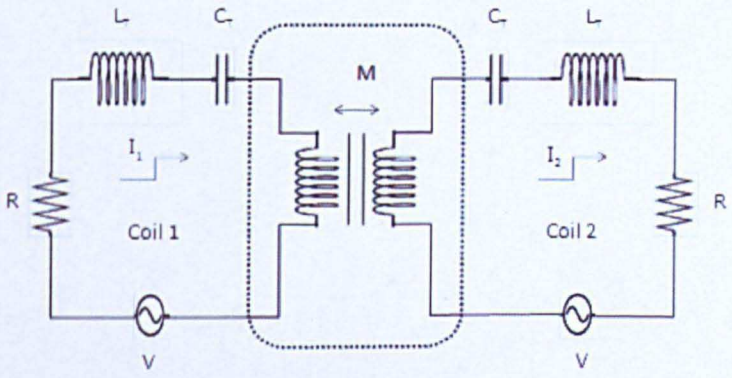

Figure 4.2-3: The circuit diagram representing the two-element coil and mutually coupled inductors.

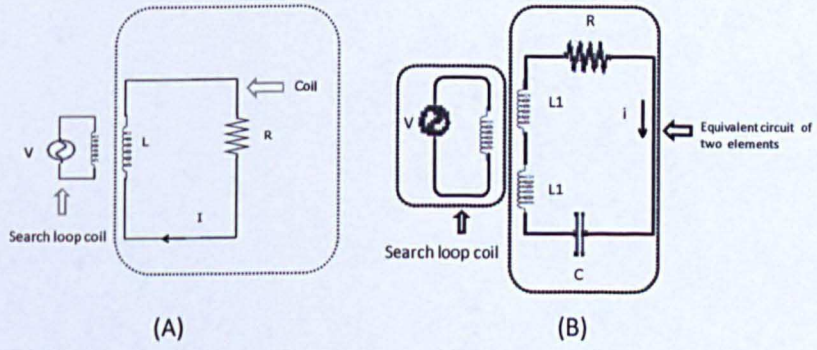

Figure 4.2-4: The circuit diagram, which represents: (A) the one-element coil and (B) the circuit interacting with search loop coil.

4.3 B_1^- Mapping

After the coil simulations were tuned at 300 MHz then the coil was driven with a current source (10 A) and the simulation was continued until the system reached a steady state. The magnetic fields (H_x, H_y and H_z) were saved in XFDTD and then MATLAB code was used to compute the B_1^-. In this research, four comparison studies were performed as the following: The B_1^- mapping produced from an individual element was computed, produced from both elements together and as well as that B_1^- generated by adding two images together, it means that the coil is fully decoupled numerically. The magnitudes of the negative B_1^- magnetic fields were computed using the following equation [6]:

$$B_1^- = (B_x - i\,B_y)/2. \qquad 4.3.1$$

Figure 4.3-1 and Figure 4.3-2 compare the generation of one element and two elements simultaneously in the simulation. It can be seen that more magnetic field was found to be close to the surface of each element and less in the centre of the phantom.

Simulation imaging results showed that the receptive field B_1^- distribution produced from the first element and the second element seemed to be uniform, as shown in Figure 4.3-2. The B_1^- generated from individual elements decayed away from each element. The profiles are taken in the x-direction, the field intensity was very high close to the coil, but fell away further into the phantom. The B_1^- reached a peak of 0.055 (μT/A) close to the surface of the receiver coil and then the B_1^- dropped away and reached a minimum value 0.03 (μT/A) close to the second element, as shown in Figure 4.3-2 (A) and Figure 4.3-2 (B). Moreover, adding more than one element increased the field of view, as more B_1^- will be detected when using this design. The B_1^- values demonstrated in Figure 4.3-2 (C) that B_1^- increased in the centre of the coil, and the B_1^- in this probe become more uniform. The B_1^- from the individual elements was combined by using root of the sum of squares method as shown in Figure 4.3-2 (D).

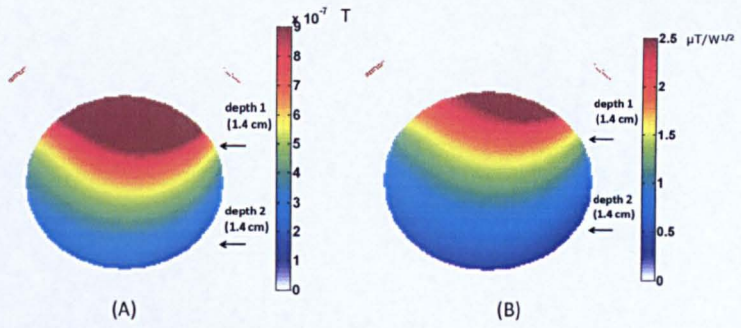

Figure 4.3-1: The B_1^- mapping and sensitivity of the one-element in the *x-y* plane, in linear scale and normalized for 1 W delivered power. The phantom is 6 cm in diameter.

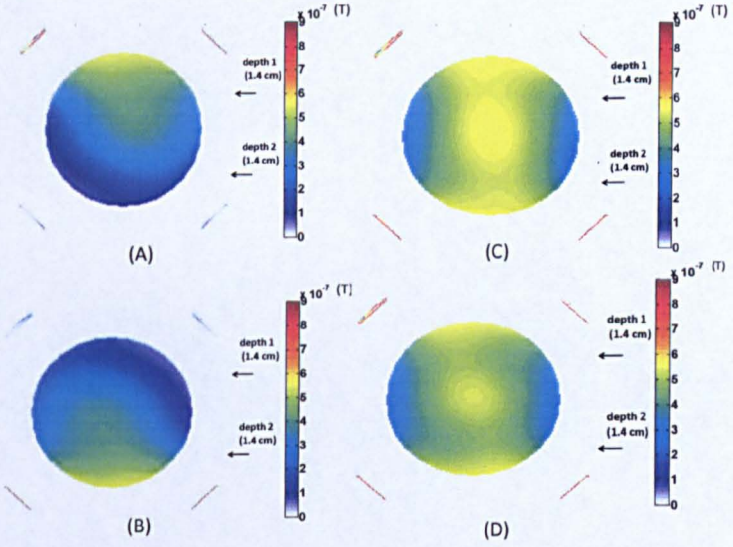

Figure 4.3-2: The B_1^- mapping generated: (A) the first element, (B) second element, (C) two elements simultaneous and (D) adding two elements.

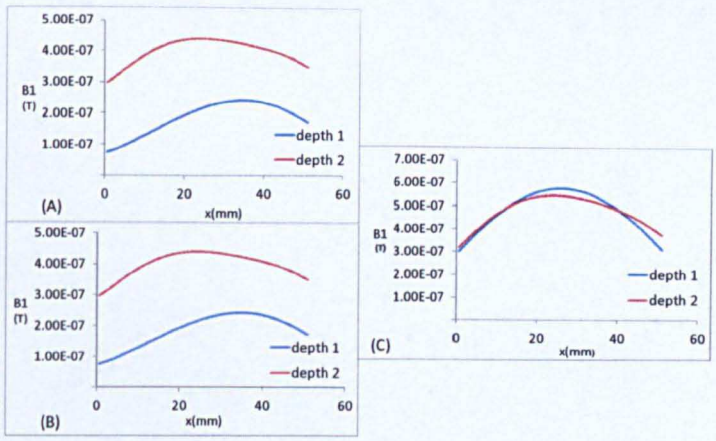

Figure 4.3-3: The line cross of the B_1^- mapping: (A) the first element, (B) second element and (C) two elements simultaneously.

As far as the magnetic field uniformity is concerned, it is computed by using the following equation [7]:

$$U = (B^-_{max} - B^-_{min}) / (B^-_{max} + B^-_{min}). \qquad 4.3.2$$

The image uniformity values for each individual element appeared approximately identical. The uniformity of the first and second element were about 0.696 and 0.716 respectively, whereas combing two elements together reached at 0.466, a lower value indicates to higher uniformity within the region of interest. Therefore, two-element close to each other is the key to acquiring good uniformity and coverage.

4.4 Sensitivity

Once the B_1^- is obtained, the sensitivity can then be computed. The coil sensitivity should be considered to obtain good quality images by improving the coil design, because non-uniform sensitivity generates problem in image quality. It can be said that the signal to noise ratio proportional to B_1^- and the intensity of B_1^- depend on the tissue's location. The image intensity will vary as a function of

position, even for a homogenous sample or tissue. Simulation results demonstrated that the coil sensitivity varied with depth as shown in Figure 4.4-1 (A and B).

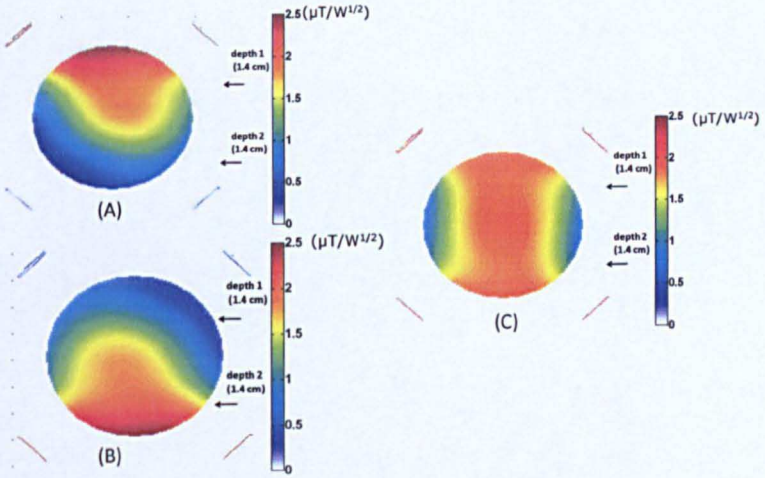

Figure 4.4-1: The sensitivity mapping computed: (A) the first element, (B) second element and (C) two elements simultaneous, in linear scale and normalized for 1 W delivered power.

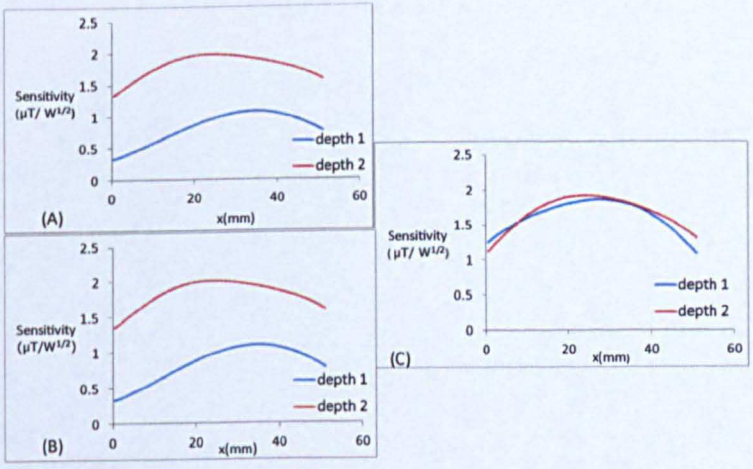

Figure 4.4-2: The line cross of the sensitivity mapping: (A) the first element, (B) second element and (C) two elements together, normalized for 1 W delivered power.

4.5 Results

The performance of this coil has been characterized by XFDTD software and phantom studies were used to compare the designs. This comparison indicates that the magnetic field was stronger near the first element, but weaker near the second element and vice versa. The B_1^- field is computed by analyzing the H_x and H_y data set produced in XFDTD. The B_1^- was calculated for each coil and then for the two elements simultaneously in order to predict the B_1^- uniformity after the B_1^- combination of two elements, therefore uniformity calculations showed improvement in homogeneity when adding two elements. Simulation calculated very little coupling between elements but in reality coupling was certainly present.

4.6 Coil Construction

The coil was constructed in the electronic laboratory for imaging a phantom and a human wrist. A coil with two identical elements was built as shown in Figure 4.6-1. Each element was made of copper tape (10 *mm* wide and 55 *mm* long) and placed on a Perspex tube with an inner diameter of 92 *mm*. This is constant throughout this study. Each element consisted of 8 tuning capacitors and 1 capacitor for matching impedance.

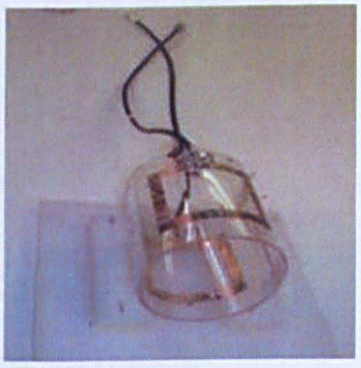

Figure 4.6-1: A photograph of the coil.

As described in the simulations section, the reason for having multiple tuning capacitors is to reduce electrical coupling with the wrist. This coupling is due to

parasitic capacitances that occur between the coil and the phantom or human wrist. Distributed capacitors reduce the electrical length of the coil. By adding more tuning capacitors to the coil, the sensitivity of the coil is improved. It means that the quality factor should be increased. The coil consists of two electrical circuits; the first circuit consists of a large loop with eight tuning capacitors and the second circuit has a capacitor for matching impedance and a PIN diode.

In order to reduce coupling between the transmitter coil and the receiver coil, the receiver coil must be sufficiently detuned when the transmitter coil is tuned for transmission [8]. Therefore, the PIN diode is used as an electronic gate [9]. One advantage of this configuration is that when the PIN diode becomes reverse biased, the coil behaves as a receiver. During transmission the PIN diode becomes forward biased and presents a very low resistance, it acts as a switching device detuning the circuit and the currents induced only in the small circuits in each element generated small amount of magnetic fields that add or subtract from the main exciting RF field produced by the head coil.

4.7 Electric Circuit of the Coil

The electrical components of a single element are shown in Figure 4.8-1. The large circuit consists of equivalent inductance(L_2) that is made of eight segments of copper tape. The equivalent capacitor is C_3 (8 capacitors were distributed) in a single element. Two capacitors (C_1 and C_2) were used for varying tuning frequency and matching impedance respectively. The resonant frequency of each element was adjusted to be 298 MHz. When element one was put close to element two, their frequency response split into separate frequencies due to electromagnetic coupling between the elements. This means that inductive coupling (M) between the element was created [10]. In this study, a low input impedance pre-amplifier was used to decouple the elements as shown in Figure 4.7-1. The output port of the receiver coil is connected to the low input impedance preamplifier. A lower input impedance preamplifier can obtain very good decoupling; usually the impedance of the preamplifier lies between 1 and 2 ohm.

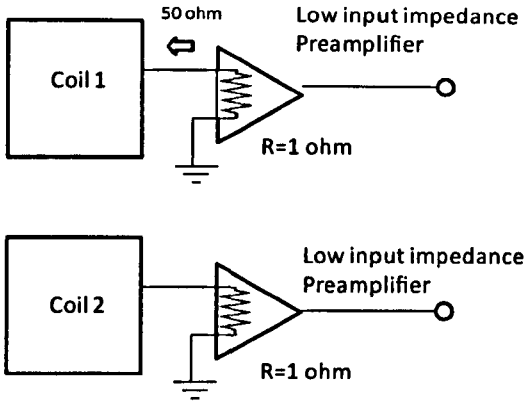

Figure 4.7-1: Block diagram of the decoupling of two elements by connecting them to a low input impedance preamplifier.

4.8 Decoupling Techniques

Decoupling between neighbouring elements can be minimized by using different methods, such as adding decoupling capacitors, adding inductors between the elements [11, 12] or connecting each element to low input impedance pre-amplifier [13]. In this study, a low input impedance pre-amplifier (typically 1 ohm) was used to decouple multiple elements. Elements will function independently and receive signals from a single region only. Each element of the coil was fed by a coaxial cable and in order to decouple elements using low impedance pre-amplifiers, a precise length of 50 ohm cable was used, as shown in Figure 4.8-1. A search coil was used to introduce a small signal into the line and the output of the amplifier was monitored.

The coaxial cable was simulated and obtained the precise length for use at 300 MHz as already shown in chapter three. The cable length (one plus an eighth wavelength) was determined by connecting one end of it to a low input impedance preamplifier and the other end to the coil with only the match capacitor in circuit.

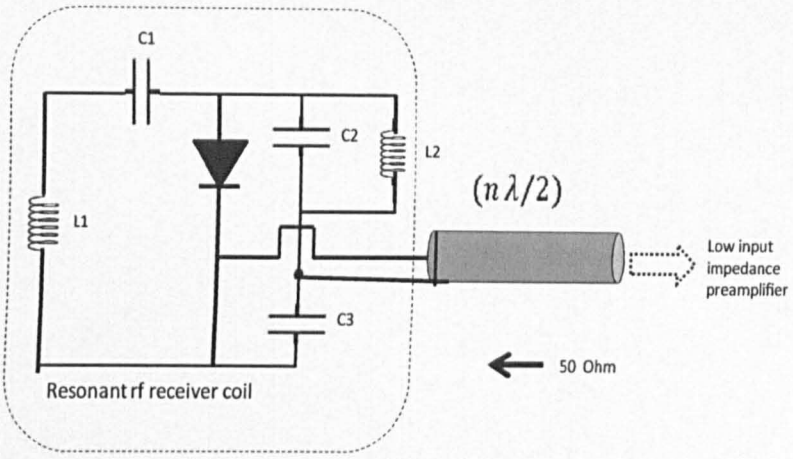

Figure 4.8-1: The schematic illustration of the electric circuit of a single element.

The line length is correct when this part of the circuit tunes to 298 MHz. the transmission line equation gives:

$$Z_{in} = Z_o[(Z_1 + jZ_o \tan \beta l)/(Z_o + jZ_1 \tan \beta l). \qquad 4.8.1$$

If Z_l is the pre-amplifier low real impedance then for an electrical length just greater than a wavelength an impedance equivalent to an inductor is generated, which forms the tuned circuit, which then gives rise to high impedance across the capacitor and de-tunes the probe. For a signal picked up by the probe, then Z_l (now the coil source impedance) is equal to 50 ohms and the length of the cable is not important.

The pre-amplifiers see the coil as 50 ohms, in order to demonstrate that the decoupling is working, a signal is introduced by a search coil into the probe and the signal at the amplifiers monitored.

The coils were tuned and evaluated at 298 MHz on a work bench using a Network analyzer as shown in Figure 4.8-2. The coils were loaded with a cylindrical plastic bottle 6 *cm* in diameter and 11 *cm* long, containing KCl and $CuSO_4$. It was found that during the experiments in the electronic lab, the phantom provided similar RF

loading to the human wrist. The frequency response of a single element showed a characteristic double peak. The operating frequency was located between the two peaks [1] as shown in Figure 4.8-2. The probe tuning and balanced matching ensures that the coils were intrinsically balanced so no additional bal-un circuit was required. Note that although the frequency of operation appears to be at a minimum, this is the point of optimum noise-match.

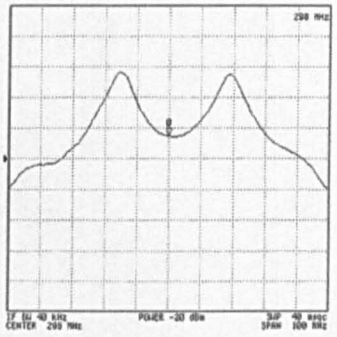

Figure 4.8-2: The operating frequency lies between the two peaks at 298 MHz.

4.9 Quality Factor

It is important to test the coil on the workbench before it is used in the MRI scanner. Its behaviour can be assessed in the presence of the sample loading such as by a phantom. The quality of MRI images depends on the probe used to detect the signal emitted from the phantom or patient. The receiver coil should have a high quality factor to generate a good signal to noise ratio [14]. Q-factor is measured as the ratio of the resonance frequency to the full width half maximum. The unloaded and loaded quality factors Q for each individual element were measured using a network analyzer. The first and second elements had an unloaded Q_o to loaded Q_L ratio [15]: L_{f1}=103/27 and L_{f2}=109/33 respectively. Where the L_f is the loaded factor and affected by designing of the coil and can be increased by increasing distance between the coil and the load [16]. Therefore, the sensitivity of the first element and second element equal to 3.8 and 3.3 respectively.

4.10 Phantom Imaging

Two comparison studies were performed by imaging with each of elements individually and both elements together. MRI experiments were performed on the 7T Philips scanner, localized images were acquired by using 2 channels out of the 16 channel receiver box and the volume transmitter coil. The receiver coil had to be placed parallel to the main magnetic field B_o, its sensitive direction was transverse to Bo. Therefore, the receiver coil was placed in a head transmitter coil and the phantom was placed in the receiver coil and then images were obtained from a homogenous cylindrical phantom (6 *cm* diameter, 11 *cm* in length).

Figure 4.10-1 shows an axial slice, which displays good image quality. A Fast Field Echo (FFE) technique was used to image the phantom with imaging parameters: TE/TR=4.92/30 *ms*, FOV= 120×15×120 mm^3. Moreover, each element has its own channel for signal reception. Images are obtained from each element and then combined in one image. Therefore, saving raw data is very significant, as it can be used to reconstruct the image from different channels after the scan. The images shown in Figure 4.10-1 (A) were obtained from the reconstruction of combining channels one and two, while images Figure 4.10-1 (B and C) were acquired from the channel one and channel two respectively. Images were reconstructed for each channel and the volume of interest was fully covered.

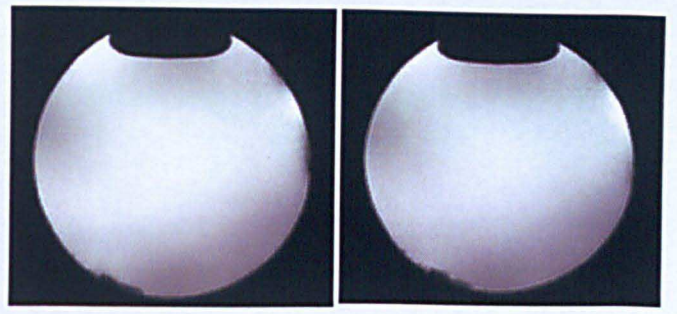

(A) channel 1 and channel 2

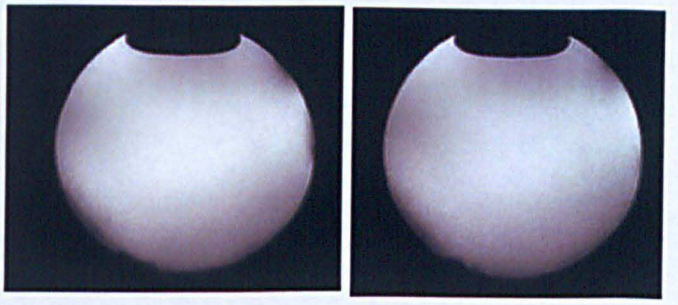

(B) Channel 1

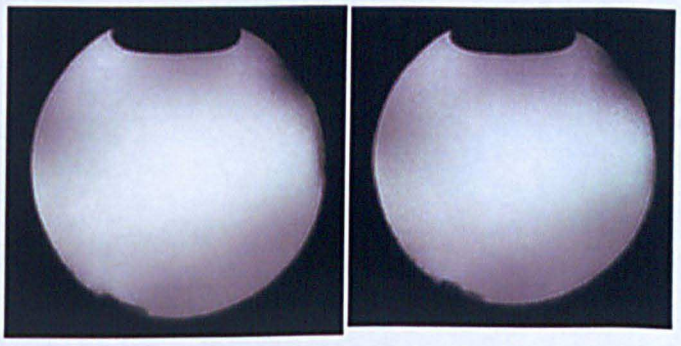

(C) channel 2

Figure 4.10-1: The image of the phantom (6 *cm* diameter, 11 *cm* in length) obtained from the combination of both elements (A), from a delayed reconstruction of channel 1 (B), from a delayed reconstruction of the channel 2 (C).

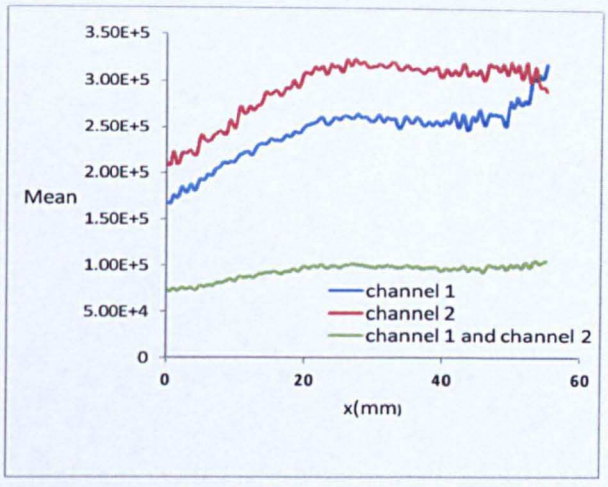

Figure 4.10-2: The line cross in the middle of the image obtained from channel one, channel two, from channel one and two.

In this study, the delayed reconstruction method was used. Therefore, we can compare the mean signals that were obtained from the wrist coil by detection with signals from both elements simultaneously, as shown in Figure 4.10-2. The values were calculated in the same slice and a line in the middle of each image was chosen. It seems from the figures that the coil had very good reception. We obtained good detection from element one (channel one) and element two (channel two). It was noted that there was a little difference between the values shown in Figure 4.10-2. This is because the phantom should have been in the centre of the wrist coil and exactly between the two elements, and the wrist coil should also been in the centre of the transmitter.

4.11 Signal to Noise Ratio (SNR)

It is very important to compute the signal to noise ratio (SNR). If the SNR is not high enough, it becomes impossible to differentiate tissues from each other or the background. We can calculate the SNR by computing the ratio of the mean signal in a sub-region within the region of interest (ROI) with the standard deviation in the background electrical noise [17]. The SNR can be defined as follows [18]:

$$\text{SNR} = \frac{\text{Mean signal}}{\text{Standard deviation}}.$$

SNR may be influenced by using several parameters such as spin echo (SE) and fast spin echo (FSE) sequences, a long repetition time (TR) and short echo time (TE), the narrowest receive bandwidth, a flip angle of 90 degree, slice thickness, and size of the coil and tuning.

To calculate the SNR, ImageJ software is involved to obtain the average signal intensity of the ROI and the background noise. If no background noise appears in the images the same scan should be repeated with the same parameters and then the subtraction of two images to obtain the noise in the images; the noise is the standard deviation (random variation in pixel intensity) in the ROI in the subtracted image [4]. Figure 4.11-1 shows the SNR of two elements combined together. Therefore, this configuration provides improved SNR in the centre. This study showed that the intensity is higher in the region where the elements were closest to the phantom. This is because the magnetic field induced voltage picked up close to the element and weaker further away from the element as shown in simulations.

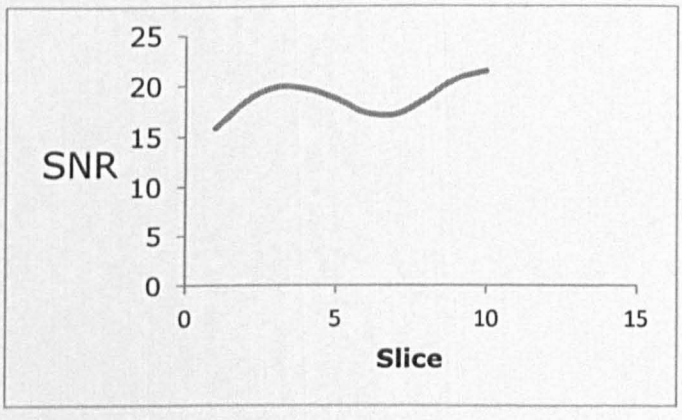

Figure 4.11-1: Turbo Spin Echo sequence (T_R/T_E= 3000/100 *ms* and a flip angle=90^0) was used to obtain SNR from two elements simultaneously loaded with phantom.

4.12 *In Vivo* Imaging

Localized anatomical images were acquired successfully from a two-element receiver coil. A quadrature transmitter head coil was used and a two-channel receiver coil was connected to 2 channel of the 16 receiver box. High-resolution images of the wrist were acquired using T1W-TSE (Turbo Spin Echo) sequence TE/TR=23/800 *ms*, a 90-degree flip angle and FOV= $80 \times 92 \times 80\ mm^3$ and the images resolution was about 0.5 mm^3, some of the *in vivo* MRI images of the human wrist are presented in Figure 4.12-1. Many anatomical features of a human wrist can be recognised such as muscle and bone. Various imaging methods were attempted to image a human wrist. Images were performed on the 7T to scan the same volunteer (right wrist). The FFE sequence was used with the following parameters: TE/TR=4.93/500 ms, a flip angle=20°, FOV=$80 \times 47.5 \times 80\ mm^3$.

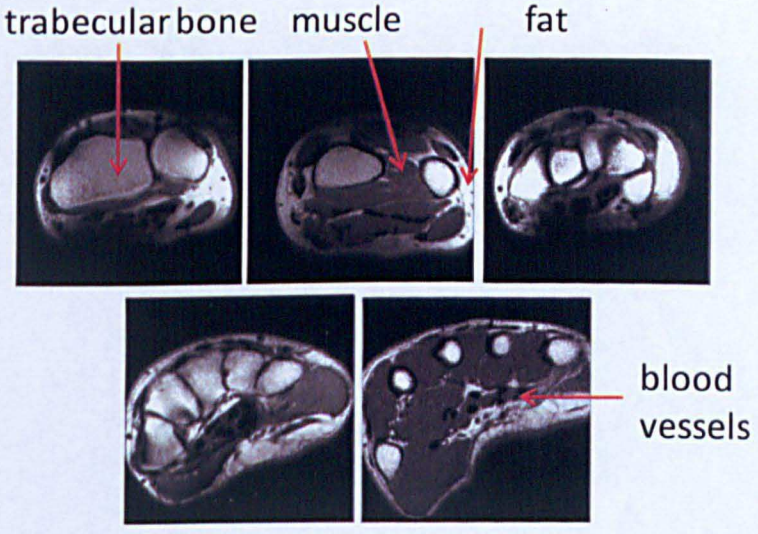

Figure 4.12-1: *In vivo* wrist cross-section obtained in transverse slices using a two element receiver coil and the T_1-weighted Turbo Spin Echo sequence was used with following parameters: TE/TR=23/800 *ms*, a 90-degree flip angle and FOV=$80 \times 92 \times 80\ mm^3$.

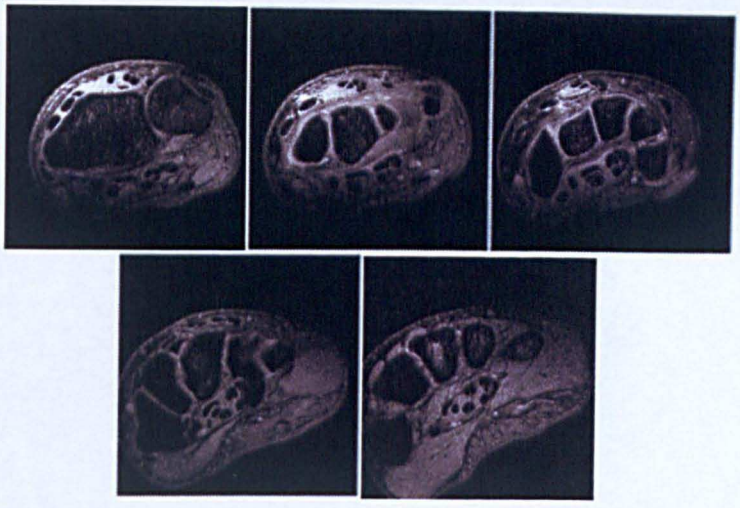

Figure 4.12-2: The human wrist images obtained in transverse slices using a two element receiver coil. FFE sequence was used with following parameters: (T_E/T_R) = (4.93/500) *ms* and a flip angle=20°.

4.13 Discussion and Conclusion

A two-channel array coil for imaging of the wrist was designed. Two elements were simulated individually and had the same dimensions and also the same structure. The phantom was placed in the middle of the coil. One of the main advantages of this method was that the receptive field distribution could be observed individually. The results of this study demonstrated that one element is insufficient for wrist detection, but adding two elements has a larger coverage. Modelling and experiments showed that the desired improvement in SNR and homogeneous coverage compared to a one element design. The noise correlation should be measured when adding *n* elements, the noise will affect the SNR and homogeneity. It can be measured by using the noise covariance matrix (NCM) from raw data by using the following expression:

$\rho_{ij}=N_i\ N_j\ \cos(\Phi_i - \Phi_j)/\sqrt{(<N_i>^2<N_j>^2)}$. Where N is max noise amplitude, Φ_i is the angle between the B_1 and **m** is the magnetic moment of the voxel for element i [4]. It can be said that the B_1^- generated from two elements appeared to be more uniform. The result of simulation is quite agreeable with measurements.

Therefore, the two-element design could be used as a fully decoupled pair of elements for multi-channel data acquisition at 7T.

References:

1. Nordmeyer, J.A., N. De Zanche, and K.P. Pruessmann, *Mechanically Adjustable Coil Array for Wrist MRI.* Magnetic Resonance in Medicine, 2009. **61**: p. 429 – 438.

2. Bjorn, B., S. Jorg, and W. Schneider, *MR imaging of the human hand and wrist at 7T.* Skeletal Radiology, 2009. **38**: p. 911-917.

3. Andreuccetti, D., R. Fossi, and C. Petrucci. *Dielectric Properties of Body Tissues.* 2012 [cited 2012; Available from:http://niremf.ifac.cnr.it/tissprop/htmlclie/htmlclie.htm#atsftag.

4. Kwok, W.E., J. Z, and G. Seo, *A four element phased array coil for high resolution and parallel MR imaging of the knee.* Magnetic Resonance imaging, 2003. **21**(9): p. 961-967.

5. Mispelter, J., M. Lupu, and A. Briquet, *NMR Probeheads for biophysical and biomedical experiments* 2006: Imperial college.

6. Hoult, D.I., *The Principle of Reciprocity in Signal Strength Calculations.* Magnetic Resonance, 2000. **12**(4): p. 173-187.

7. Kocharian, A., M.C. Adkins, K. Amrami, and L.P. Felmlee, *Wrist : Improved MR Imaging with Optimized Transmit-Receiver Coil Design.* Radiology, 2002: p. 870-876.

8. Vaughan, J.T., G. Adriany, M. Garwood, E. Yacoub, and K. Ugurbil, *Detunable Transverse Electromagnetic (TEM) Volume Coil for High-Field NMR.* Magnetic Resonace in Medicine, 2002. **47**: p. 990-1000.

9. Wiggins, G.C., A. Potthast, and L. Wald, *Eight-Channel Phased Array Coil And Detunable TEM Volume Coil for 7 T Brain Imaging.* Magnetic Resonace in Medicine, 2005. **54**: p. 235-240.

10. Guclu, C.C., E. Boskamp, T. Zheng, R. Becerra, and L. Blawat, *A Method for Preamplifier-Decoupling*

Improvementin Quadrature Phased-Array Coils. MAGNETIC RESONANCE IMAGING, 2004. **19**: p. 255–258.

11. Adriany, G., T. Vaugha, and K. Ugurbil, *Transmit and receive Transmission Line Array for 7 Tesla Parallel Imaging.* Magnetic Resonance Medicine, 2005. **53**: p. 434-445.

12. Zhang, X. and A. Webb, *Design of a capacitively decoupled transmit/receive NMR phased array for high field microscopy at 14.1 T.* Magnetic Resonance, 2004. **170**: p. 149-155.

13. Ray, F.L., O. Giaquinto, and C. Hardy, *Coupling and Decoupling Theory and Its Application to the MRI Phased Array.* Magnetic Resonance Medicine, 2002. **48**: p. 203-213.

14. McVeigh, E.R., M.J. Bronskill, and R.M. Henkelman, *Phase and sensitivity of receiver coils in magnetic resonace imaging.* Med. Phys., 1986. **13**(6): p. 806-814.

15. Hayes, C.E., W.A. Edelstein, and M. Eash, *An Efficient, Highly HOMOGENOUS radiofrequency coil for Whole-body NMR imaging at 1.5T.* magnetic Resonance, 1985. **63**: p. 622-628.

16. Vernickel, P., P. Roschmann, C. Findeklee, K.M. Ludeke, J. Overweg, U. Katscher, J. Grasslin, and K. Schunemann, *Eight-channel transmit/receive body MRI coil at 3T.* Magnetic Resonance in Medicine, 2007. **58**: p. 381–389.

17. Gomerner, F.L. and G.D. Clarke, *Measuring signal-to-noise ratio in partially parallel imaging MRI.* Medical Physics, 2011. **38**: p. 5049-5057.

18. Nallo, A.M., O. Ortenzia, and M.D. Arienzo, *MRI Quality Control Tools for Procedures and analyses.* J. Exp. Clin Cancer Research, 2006. **25**.

Chapter 5

Microstrip Line Coils

5 Introduction

This chapter describes the development of coils consisting of one element and two element striplines. The microstrip transmission line has been used in various types of non-MRI applications such as antenna feed lines and computer network cables. Recently it has been widely used in the field of designing MRI RF probes. In this research, RF stripline coils were designed and build that can be used to transmit and receive the signals. We designed and built one-strip and two-strip line coils close to each other, which will be detailed in the following sections. One-strip line and two-strip line were loaded with the muscle tissue phantom for the simulations. Further study was carried out for one-strip and two-strip coils loaded with the dielectric model of the human pelvis to compute the SAR and B_1^+.

5.1 Microstrip Line Theory

This section will give a brief overview of microstrip line theory. The simplest structure of the microstrip line is composed of a thin strip of conductor, usually made of copper, and a ground plane separated by a dielectric layer as illustrated in Figure 5.1-1. It can usually be assumed that most of the electric field resides within the substrate [1].

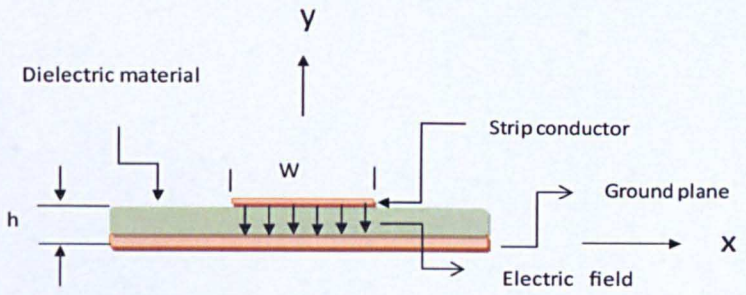

Figure 5.1-1: The microstrip line, where L is the length of the strip line, W is the width of the strip conductor; h is the thickness of the substrate.

The transmission line circuit parameters are distributed and defined as:

- the capacitance parameter C (F/m), which is the capacitance per unit length between the strip conductor and the ground
- the inductance parameter L (H/m), which is the loop inductance per unit length
- the resistance R (Ω/m), which is the series resistance per unit length

Therefore, R, C and L are the transmission line parameters, which can be represented in terms of the electric and magnetic fields, as follows

$$R = \frac{R_s}{|I|^2} \int \boldsymbol{J}.\boldsymbol{J}^* \, dl, \qquad 5.1.1$$

$$C = \frac{\epsilon'}{|V|^2} \int \boldsymbol{E}.\boldsymbol{E}^* \, ds, \qquad 5.1.2$$

$$L = \frac{\mu}{|I|^2} \int \boldsymbol{H}.\boldsymbol{H}^* \, ds, \qquad 5.1.3$$

Where **E** and **H** are the electric and magnetic fields, R_s is the resistance of the conductors and ϵ' is the permittivity.

Moreover, it can be assumed that the resonant wavelength of the microstrip line is $= \lambda_o/\sqrt{\varepsilon_{eff}}$, where λ_o is the wavelength of the magnetic field in free space and ε_{eff} is the effective dielectric constant [2]. To determine the characteristic impedance of a microstrip line, the following parameters need to be considered:

- the relative dielectric constant ε_r,
- the dielectric substrate thickness h,
- the width of the strip conductor W,

Based on the follows equations and in this theory the interaction with a body is neglected [3, 4], the characteristic impedance, effective dielectric constant and a fundamental or primary resonance frequency can be computed this occurs when the physical length of the strip conductor is roughly half the wavelength:

$$Z_o = \frac{60}{\sqrt{\varepsilon_{eff}}} ln\left(\frac{8h}{W} + \frac{W}{4h}\right) \quad \text{when} \quad w/h \leq 1, \qquad 5.1.4$$

Where:

$$\varepsilon_{eff} = \frac{\varepsilon_r+1}{2} + \frac{\varepsilon_r-1}{2\sqrt{1+\frac{12h}{W}}} + 0.02(\varepsilon_r - 1)(1 - \frac{W}{h})^2. \qquad 5.1.5$$

Otherwise:

$$Z_0 = \frac{120\pi}{\sqrt{\varepsilon_r}\left\{\frac{W}{h}+1.393+0.667\ln\left(\frac{W}{h}+1.444\right)\right\}} \quad \text{When} \quad W/h \geq 1, \qquad 5.1.6$$

Where:

$$\varepsilon_{eff} = \frac{\varepsilon_r+1}{2} + \frac{\varepsilon_r-1}{2\sqrt{1+\frac{12h}{w}}}, \qquad 5.1.7$$

$$f = \frac{c}{2L\sqrt{\varepsilon_{eff}}}. \qquad 5.1.8$$

5.2 Current Distribution in the Flat-Strip

The current density in a flat conductor is highest at the surface of a conductor and decays exponentially from its value at the surface. The distribution of the current on a flat-strip conductor is given by

$$j(x) = \frac{I}{2\pi}\frac{1}{\sqrt{b^2 - x^2}} \qquad -b < x < b, \qquad 5.2.1$$

Where I represent the total current and b is the width of the strip. The magnetic field at any point on the surface of the strip line, as shown in Figure 5.2-1 can be determined by using the following equation:

$$dB(x') = \frac{\mu_o}{2\pi}\frac{j(x)}{(x - x')}. \qquad 5.2.2$$

The total magnetic field at any point can be defined by:

$$B(x') = \frac{\mu_o}{2\pi}\left(-\int_{x=-b}^{x'-\varepsilon}\frac{j(x)}{|x-x'|}\,dx + \int_{x'+\varepsilon}^{x=b}\frac{j(x)}{|x-x'|}\,dx\right). \qquad 5.2.3$$

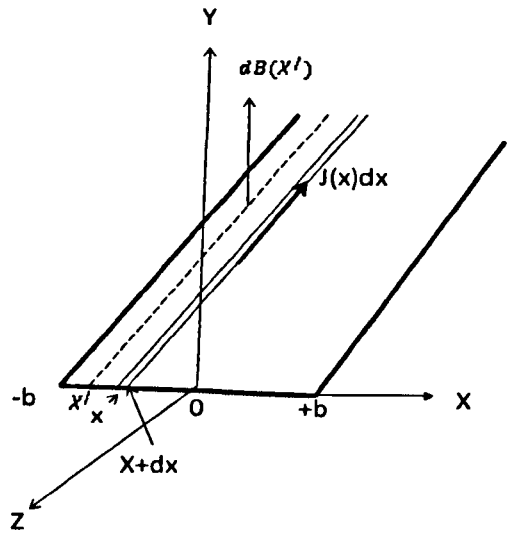

Figure 5.2-1: The magnetic field generated by the flat conductor which is produced by a current filament $j_Z(x)\ dx$.

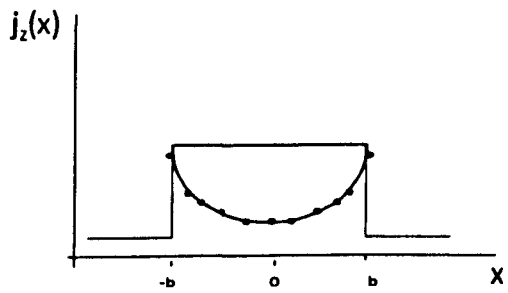

Figure 5.2-2: The current distribution of the flat-strip line.

A net increase of the current close to both edges of the strip-line conductor can be observed, whereas there is a uniform lower distribution near the centre of the conductor as shown in Figure 5.2-2. The current density can be described as a set of discrete longitudinal current filaments I_k positioned at a certain location x_k. The magnetic field generated by all currents can then be calculated as [5]:

$$B_{ij} = \frac{\mu_o}{2\pi}\left(\sum_{k(x_j>x_k)} I_k \frac{1}{|x_j - x_k|} - \sum_{k(x_j<x_k)} I_k \frac{1}{|x_j - x_k|}\right). \quad 5.2.4$$

It can be concluded from this section that the total magnetic flux density across the strip conductor has two peaks, both of which appear on the edges of the element. Therefore, it can be estimated that the majority of the current flow is close to the edges of the conductor. The current distribution over the flat-strip surface shows a significant increase of current close to the edges therefore increasing the net resistance of the conductor. To evaluate these formulas numerically, the current conduction magnitude (CCM) is computed and plotted in section 5.5.

5.3 Simulations

The strip-line coil was simulated as one strip and two strips close to each other using XFDTD. The purpose of this study was to design an array coil that can provide higher SNR and increases the FOV compared with one element coil. The simulation can be described as follows: each element consisted of two plates made of Perfect Electric Conductor (PEC). The first plate was a thin-strip conductor and the second was used as a ground plate. The width of the strip was chosen as 2 cm and the distance between the strip lines and ground plate was approximately 0.5 cm. There were also two capacitors used in each element. The first capacitor was used as a tuning capacitor and placed at one end of the strip conductor, and the other was used for matching impedance and placed at the other end of the strip conductor as shown in Figure 5.11-1.

Simulations of One Element and Two Elements Loaded with Muscle Tissue Phantom

5.4 One-Strip Line and Two-Strips Coils

The one-strip line coil and two strip lines were loaded with the muscle tissue phantom filled with a dielectric of human tissue ($\varepsilon_r = 58$), the distance between the surface of the coils and the surface of phantom being 10.5 *mm*. Two elements were driven with Gaussian pulse to provide a bandwidth frequency response. The coils were tuned individually at 298 MHz. Coupling between strips was noted in the simulation by exciting one element with a voltage source and recording the voltage induced in the second element.

The coil was driven in quadrature mode by two unit power sources, 90 degrees out of phase with a sinusoidal voltage source of 300 MHz to produce steady state electric and magnetic fields inside the phantom. At 300 MHz, the wavelength in the phantom was 13.1 *cm*. The main advantages of this simulation were being able to observe the electromagnetic behaviour in the dielectric material, to consider the SAR distribution and to compare the one-strip with the two–strip coil. Furthermore, we were able to investigate if there was an increase in the efficiency of the coil when two elements driving zero and 90 degrees out of phase and also whether the field of view was increased by adding more than one element.

We tried to minimize the mutual inductance by increasing the distance (D) between the two elements to reduce the generation of an *emf* in the second element and vice-versa. The results obtained from the simulation showed that there was a little current flowing in the second element due to the magnetic field produced by the first element. It means that coupling between two elements was finite. Figure 5.5-3 (A and B) shows that the current distribution over the flat-strip surface showed a significant increase of current close to the edges. This study shows that the simulation agrees well with the theoretical equations mentioned in section 5.2.

5.5 The B_1^+ and Efficiency

Figure 5.5-4 demonstrates a comparison of the B_1^+ produced by one element and two elements driven simultaneously. Calculations were performed in such a way as to make a useful comparison between one-element and two-element.

One of the most interesting observations was that more B_1^+ was generated close to the surface of the phantom, there were two bright areas under the elements, which had high magnetic field intensity and then dropped in the middle of phantom as shown in Figure 5.5-5. It can be said that the coils have high efficiency in a near field region, because high magnetic field was produced exactly under the strip line, but the efficiency rapidly dropped off further away. When the electric fields and then the SAR were calculated, it was noted that high electric fields and SAR were located in the same area, and there was lower electric field and SAR between two elements as shown in Figure 5.5-7. Two elements approximately covered the entire phantom, and less B_1^+ appeared between the two elements, and the magnetic fields cancelled each other between the elements.

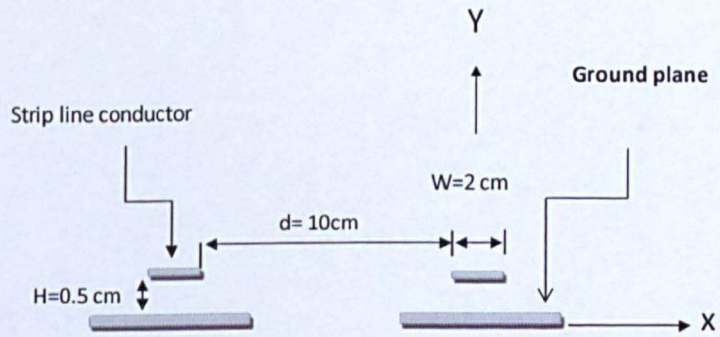

Figure 5.5-1: The schematic of a two-strip line coil

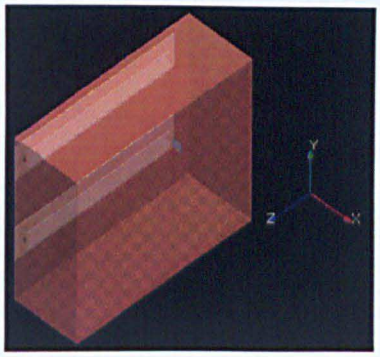

Figure 5.5-2: The two-element strip line modelled in XFDTD

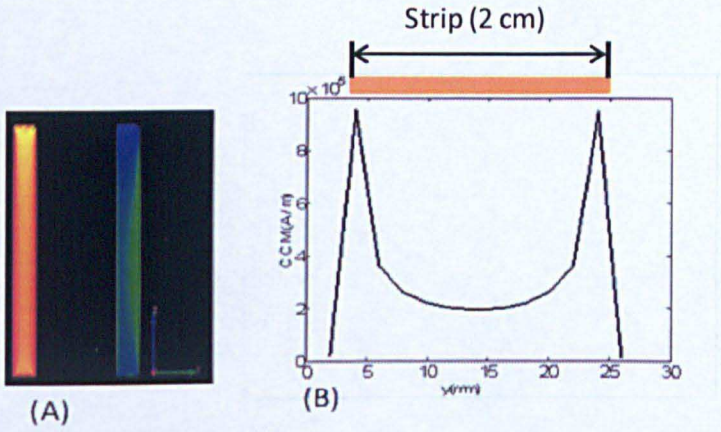

Figure 5.5-3: (A) The Conduction Current Magnitude (CCM) fields and (B) plot CCM versus distance and reached a peak on the edges of the PECs.

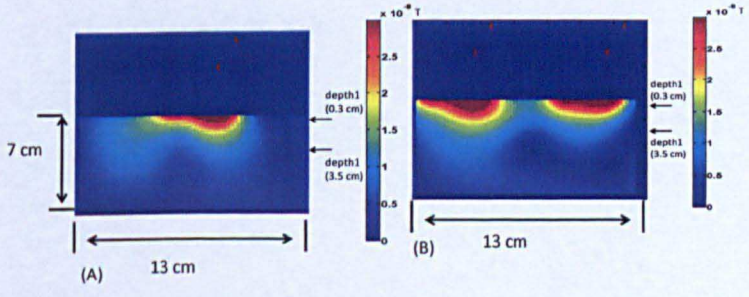

Figure 5.5-4: Simulated B_1^+ distribution inside the phantom: (A) one strip and (B) two strips.

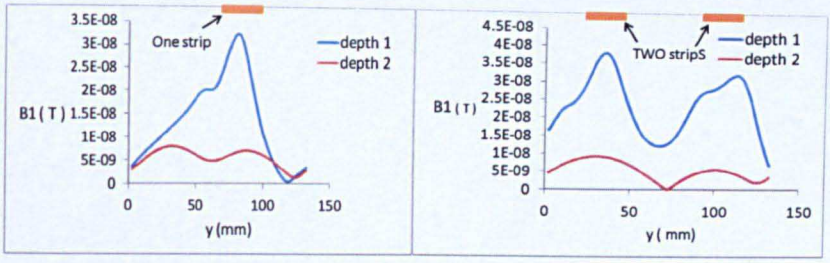

Figure 5.5-5: Simulated in depth B_1^+ profiles: (A) one strip and (B) two strips.

The B_1^+ inhomogeneity generates variation in the efficiency, and for this reason it should be computed. Figure 5.5-6 demonstrates a comparison of the uniformity it was found that two-element provides better uniformity than one element, therefore an increase in the number of elements could further enhance the homogeneity.

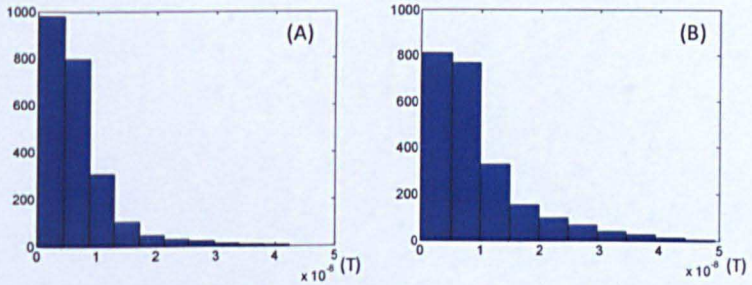

Figure 5.5-6: The histogram shows the distribution of data values (B_1^+) generated: (A) one strip and (B) two strips.

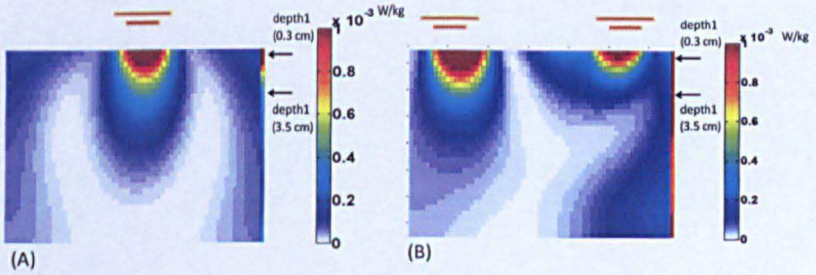

Figure 5.5-7: The SAR mapping: (A) one strip and (B) two strips.

5.6 Results of Simulation

The B_1^+ distribution shows that there was good homogeneity of the RF field close to the coil, which reached a peak at the centre of each strip element and that the transverse field also dropped off away from the centre of each element. Therefore, the RF field reduced between the coils as expected and because of this a small amount of signal will appear in the images, when used as a transmit and receive coil.

With regard to the SAR, the maximum SAR was generated directly below both the one-strip and two-strip line coils. The SAR profile produced by one element and two elements taken in the x-direction showed that the maximum SAR/B_1^{+2} reached a peak at 1.27 $(W/kg)/\mu T^2$ produced by one element and about 0.28 $(W/kg)/\mu T^2$ and 0.77 $(W/kg)/\mu T^2$ produced by two-element simultaneously. The maximum SAR/B_1^{+2} were higher for one element than two elements. Note that the efficiency of the coil in *x* direction was increased by adding the second element. Two elements can be used to increase the field of view and a two coil emit more B_1^+ in *x* direction.

5.7 One Strip and Two Elements loaded with the Human Pelvis

Figure 5.7-1 (A and B) demonstrates one element and two-element were loaded on the human pelvis model and then were tuned individually at 300 MHz. It was noted that the amplitude of tuning frequency was slightly different. This is due to two coils being placed in inhomogeneous dielectric materials and also the distance between the coils and from the shape of the pelvis to the surface of each element being different. This will affect the impedance of the coils. Note: when the adaptive mesh was used in the regions of the coil and closed to the pelvis, more cells would be generated in these regions. It would affect the actual shape of the pelvis and it stretched in vertical direction, but we are interested in the pixel's values.

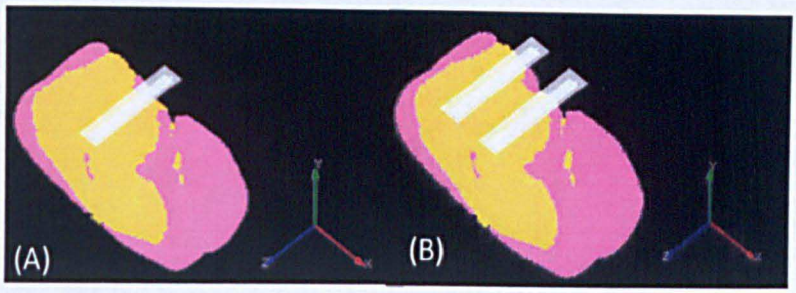

Figure 5.7-1: (A) One element loaded with the pelvis and (B) two elements loaded with the pelvis.

5.8 The B_1^+ Mapping and Efficiency

The B_1^+ comparison in the human pelvis showed that one element and two-element produced a uniform transverse magnetic field. Comparing Figure 5.8-1 (A and B), it can be seen that the field of view was increased by adding two elements and almost completely covered the pelvis region. The efficiency for one element and two elements was computed as shown in Figure 5.8-3 (A and B). These calculations explain that the coil had a higher efficiency in the near field region. Therefore, the efficiency was increased in *x* direction. However, it seems that the efficiency dropped away in y direction for one strip and two strips as well.

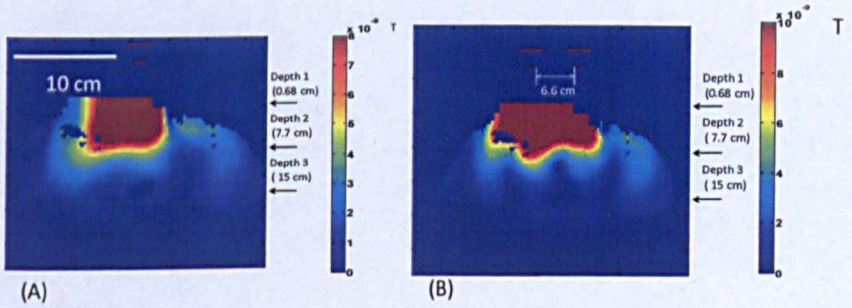

Figure 5.8-1: (A) The B_1^+ produced by one strip and (B) the B_1^+ produced by two strips. Note: the actual shape of the pelvis model affected by the adaptive mesh, more pixels generated in vertical direction and the pelvis model stretched in vertical direction.

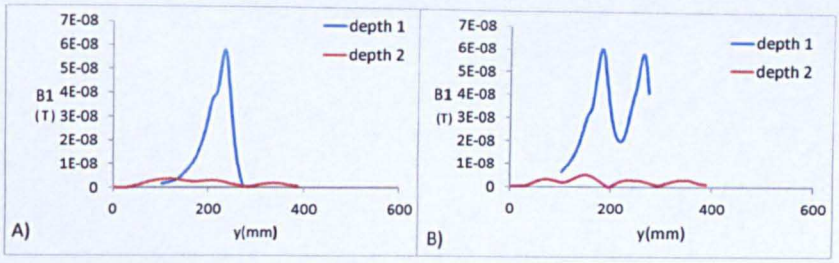

Figure 5.8-2: Computed in depth B_1^+ profiles generated: (A) one element and (B) two elements.

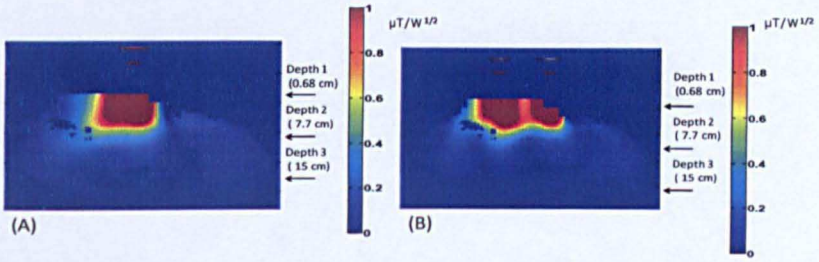

Figure 5.8-3: The efficiency mapping for the one-strip line coil (A), two elements (B) normalized for 1 W delivered power.

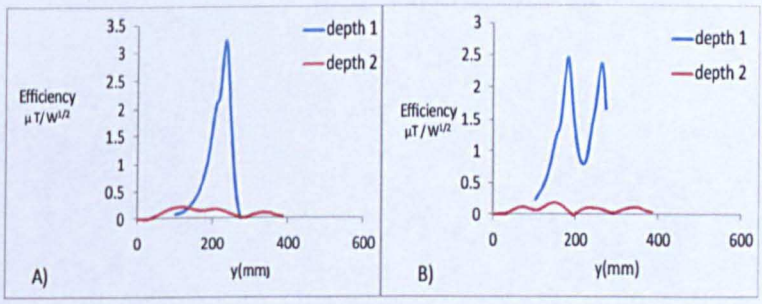

Figure 5.8-4: Calculated in depth efficiency profiles generated: (A) one element and (B) two elements, normalized for 1 W delivered power.

5.9 Electric Field

The electric fields in three dimensions *x*, *y* and *z* can be computed by saving XFDTD output data and then analyzing it to create the image in two dimensions

such as the *x-y* plane, as shown in Figure 5.9-1. These images demonstrate the total electric field generated in each pixel inside the human model. It can be seen that a higher peak electric field appears between the surface of the pelvis and the coil.

Electromagnetic waves generated by the coils will create electric and magnetic fields perpendicular to each other. As electromagnetic waves travel in free space no reflections should occur, but there is a boundary between free space and dielectric material. This can cause some electromagnetic waves to reflect back and some of these waves will be absorbed into the tissue and some will also travel in free space. It depends on the type of the material and depths. The absorption of electromagnetic wave should be considered, because it can increase the temperature of the materials. For safety reasons, the coil should be placed as close as possible to the area under examination but should not directly touch the patient's skin as it may become warm during examination. A small foam pad (2 cm thick) placed between the skin surface and the coil is sufficient insulation.

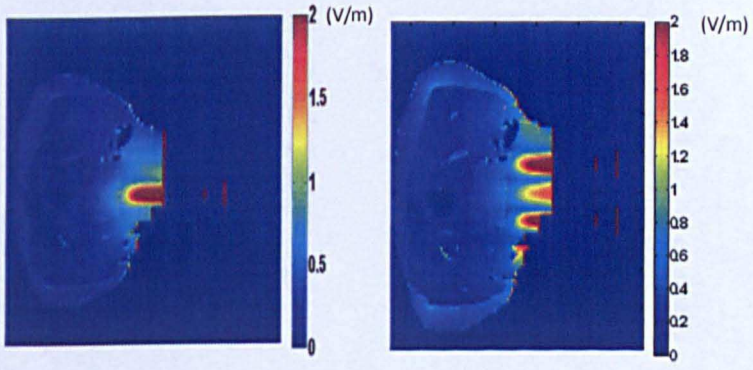

Figure 5.9-1: E_T produced: (A) one strip and (B) two strips. Note that because the adaptive mesh was used it affects the shape of the pelvis on this graphic.

5.10 The Specific Absorption Rate (SAR)

The SAR and SAR/B_1^{+2} were calculated for one and two element coils loaded with the pelvis as shown in Figure 5.10-1 (A and B) and Figure 5.10-2 (A and B).

It can be noted that the two-element coil created a higher SAR compared with one element. This was due to the inhomogeneity of electric fields that was generated by two elements. It can be seen from images that hot spots appeared in the surface of the pelvis. Therefore, most of the energy absorbed in this area, which would cause an increase in temperature. Plots of the SAR/B_1^{+2} produced inside the pelvis model by the one-strip and two-strip coil show the locations of the highest SAR/B_1^{+2} were on the surface of the pelvis, which was very close to the coils and reached a peak of 17.09 $(W/kg)/\mu T^2$ for the one-strip, 21.9 $(W/kg)/\mu T^2$ for two-strip coils respectively, as demonstrated in Figure 5.10-4 (A and B).

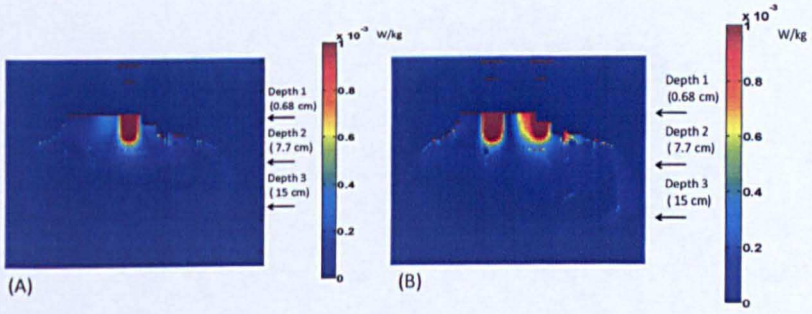

Figure 5.10-1: The SAR distributions generated: (A) the one-strip line and (B) two strips.

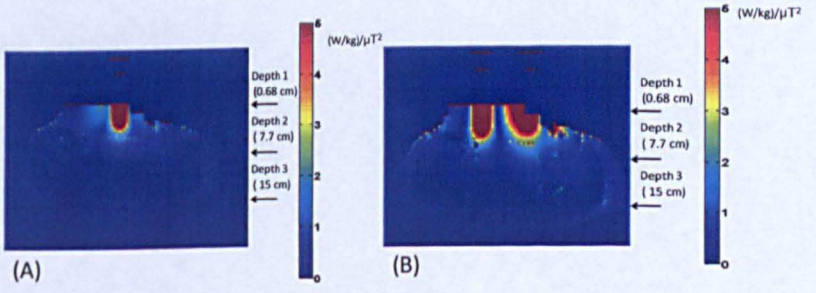

Figure 5.10-2: The SAR per B_1^{+2} distributions generated: (A) the one-strip line and (B) two-strips.

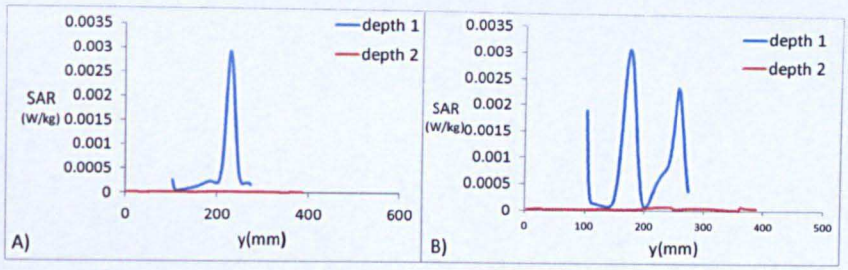

Figure 5.10-3: The line profile of SAR in depth generated: (A) the one-strip line and (B) two strips lines.

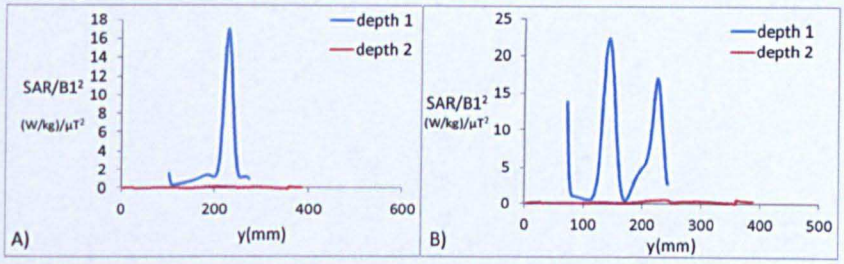

Figure 5.10-4: The line profile of SAR/B_1^{+2} in depth generated: (A) the one-strip line and (B) two strips lines.

5.11 Coil Construction

A two-channel transceiver coil was built based on the transmission line principle. The coil consisted of two identical elements that could be driven in quadrature. Each element was individually tuned at 298 MHz and matched to 50 ohms by using high power capacitors varying from 1 pF to 10 pF. The reason for using two elements was to enhance the signal to noise ratio (SNR) and also to obtain a larger field of view.

The elements were isolated and covered by a safety sheet made from perspex. Therefore, each element should be used individually or both together by connecting them with a linking piece of perspex, as shown in Figure 5.11-2. The coil can be placed on the phantom or a human pelvis and the field of view can be increased by increasing the distance between the elements. The link will allow

movement or rotation of the elements to any angle. The coil was connected to the network analyzer, and it was noted that no coupling existed between the elements.

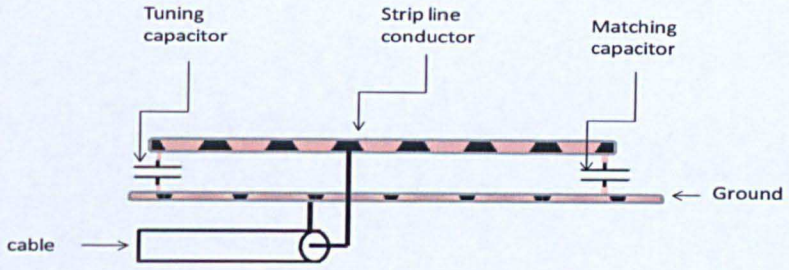

Figure 5.11-1: The schematic view of the strip line coil.

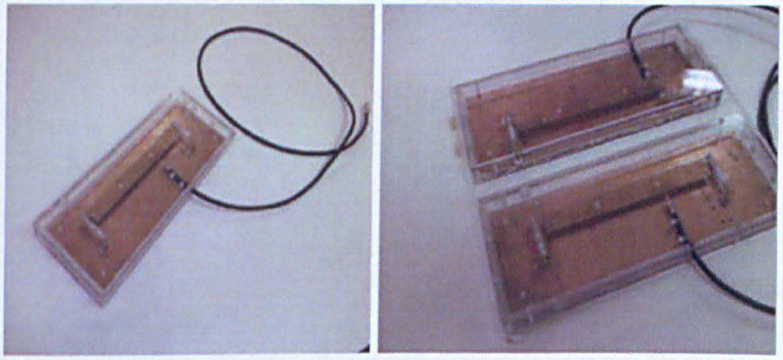

Figure 5.11-2: A photograph of the coils.

5.12 Phantom Imaging (One Strip and Two Strips)

The probe was placed parallel to the z axis of the magnet B_0, which guaranteed that the transverse component of the magnetisation was perpendicular to the probe and maximum signal was generated. The probe loaded with three phantoms (8.5 *cm* diameter, 17 *cm* in length). The first and second elements were independently connected to the linear interface box. We then obtained the images from each element as shown Figure 5.12-1 (A and B). Then both elements were driven in quadrature together to produce a circular polarized field by driving two elements at 90 degrees out of phase as shown Figure 5.12-1 (C). It can be noted that the field of view was increased when two elements placed close to each other and

loaded with the phantom as shown in the simulation. Moreover, the maximum signals were generated at driving points. Figure 5.12-1 shows the strip lines coils cover only the near field regions.

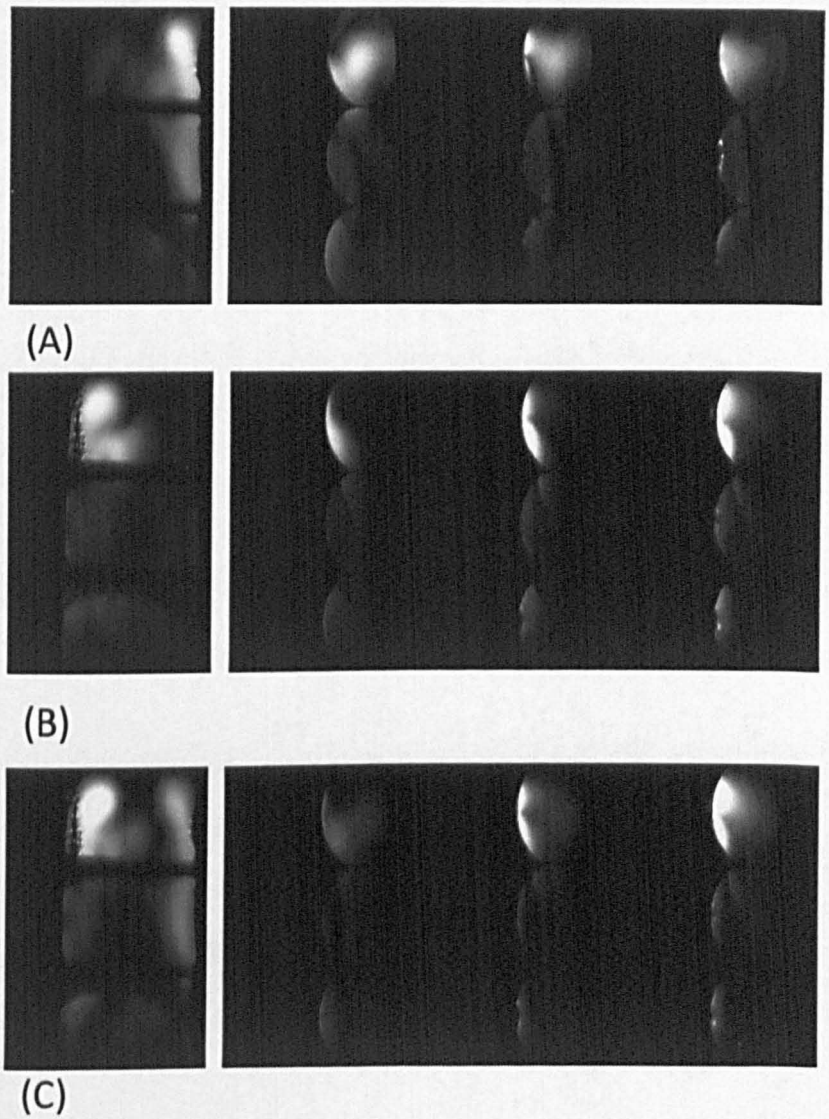

Figure 5.12-1: Coronal phantom images that obtained from (A) Left element, (B) right element and (C) combined two elements together. A cylindrical phantom (8.5 *cm* diameter, 17 *cm* in length) was scanned.

5.13 Discussion and Conclusion

Two strip line coils were simulated and constructed in the laboratory. The B_1^+ was very weak between the elements and decays away from centre of each element. It was found that the efficiency of two strips coil was higher than the one strip coil and also the field of view was increased when adding two elements. When two elements were tested on the work bench, there is no coupling apparent on the network analyser. While in the simulation, a weak coupling appeared without splitting the main resonance frequency. By driving the first element with voltage source and second element which was connected with 50 ohm and data were recorded such as CCM on the surface of each element. It was noted that the current flowed in the second element. The simulation result showed that there was a weak coupling between the elements and can be minimized by increasing the distance between two elements. In this study, two elements were driven 90^o out of phase and more simulations are required to be carried out to calculate the effect of changing the phase difference on the B_1^+. It can be concluded that the strip line coil will not be used as a surface coil because interference patterns and reflection from the ground plane occurred when a sample was placed close to the coil; the strip line coil generated high local SAR levels at the capacitors locations. It was noted that the SAR/B_1^{+2} produced by one strip line less than produced by two elements in the pelvis. We did not use the coil to scan a human pelvis, because we found that the strip line coil generated a high SAR/B_1^{+2} level in the region of interest.

References:

1. Hoefer, W.J., *The Transmission-Line Matrix Method-Theory and Applications*. IEEE, 1985. 33: p. 882-893.

2. Zhang, X., K. Ugurbil, and W. Chen, *A microstrip transmission line volume coil for human head MR imaging at 4T*. Magnetic Resonace 2003. 161: p. 242-251.

3. Zhang, X., K. Ugurbil, and W. Chen, *Microstrip RF Surface Coil Design for Extremely High Field MRI and Spectroscopy*. Magnetic Resonance in Medicine, 2001. 46: p. 443-450.

4. Ray, F.L., C.R. Westgate, R.G. Weiss, and P.A. Bottomley, *Planar Strip Array (PSA) for MRI*. Magnetic Resonace in Medicine, 2001. 45: p. 673-683.

5. Mispelter, J., M. Lupu, and A. Briquet, *NMR Probeheads for biophysical and biomedical experiments* 2006: Imperial college.

Chapter 6

Loop coils

6 Introduction

Research continues to show improvements in and uses of a radio frequency coil designs such as the simple and conventional loop coil. There are many applications of the loop coil that are widely used such as imaging of a knee. In this chapter single and dual loop coils were modelled for uses at high frequency for transmit. In the following sections, the basic theory of the loop coil is described, and a detailed study of how to design and fabricate one and two element coils. Also shown is how to decouple two elements in the simulation using XFDTD software when loaded with both the phantom and the human pelvis model. To make a comparison between the coils, the B_1^+ field, efficiency, field of view and a measure of homogeneity will be calculated. A difference in the B_1^+, efficiency and SAR generated by one and two elements can be observed. The purpose of this work is to design coils to increase the field of view (FOV), improve the homogeneity and efficiency, whilst preserving low SAR.

The loop coil will be used to transmit and receive the signals required to construct an image of the sample. Ideal coils would be easy to use, safe, and also have good quality factor. The loops should have adequate coverage and provide excellent B_1^+ near the coil. It is useful for detecting signals near the surface of the sample. The coil will be placed over the desired anatomical region such as the knee. It is necessary that consideration should be given to the safety aspects. Therefore, the SAR should be computed in order to validate the coils. Detailed calculations and measurements will be provided in the validation sections. Since there are a

number of problems associated with ultra high frequency, it can be said that it is impractical to design and build a single coil to cover all possible circumstances.

6.1 Background Theory for Loop Coils

In this section a brief overview of the loop coil has been provided. We can consider a circular loop coil of radius a placing in the x-y plane, and carrying current I as shown in Figure 6.1-1.

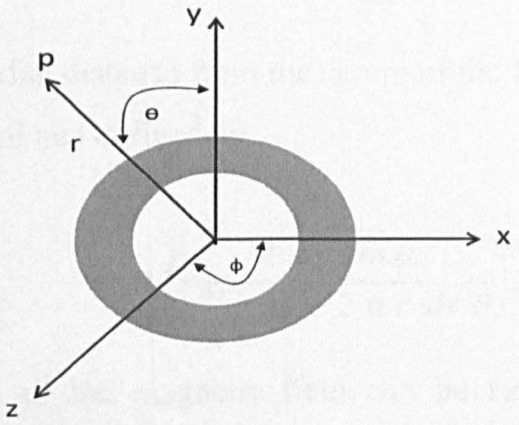

Figure 6.1-1: A circular loop coil of radius a in the x-y plane.

The current density **J** has a component in the Φ direction as defined in the following equation:

$$J_{\emptyset} = I\frac{\delta(r'-a)}{a}. \qquad 6.1.1$$

Where r is radial distance, θ is polar angle and Φ is azimuthal angle.

The above equation represents the distribution of the current on the surface of the conductor as defined using the delta functions, the current distribution will be

explained later and plotted in two dimensions in the simulation in the section 6.7. The current density **J** and the vector potential **A** can be written as

$$\mathbf{J} = -x\, J_{\emptyset} \sin \emptyset' + y\, J_{\emptyset} \cos \emptyset', \qquad 6.1.2$$

$$A_{\emptyset}(r,\theta) = \frac{\mu_o}{4\pi} \frac{4Ia}{\sqrt{a^2+r^2+2\,a\,r\,sin\,\theta}} \times \ldots$$

$$\ldots\left[\frac{(2-k^2)K(k)-2K(k)}{K^2}\right], \qquad 6.1.3$$

Where r is the radial distance from the centre of the loop coil and K is the elliptic integral and defined as:

$$K = \left(\frac{4\,a\,r\,sin\,\theta}{a^2 + r^2 + 2\,a\,r\,sin\,\theta}\right).$$

The components of the magnetic field can be expressed in three directions in the spherical coordinate system as [1]:

$$B_r = \frac{1}{r\,sin\,\theta}\frac{\partial}{\partial\theta}(sin\,\theta\, A_{\emptyset}), \qquad 6.1.4$$

$$B_{\theta} = -\frac{1}{r}\frac{\partial}{\partial r}(rA_{\emptyset}), \qquad 6.1.5$$

$$B_{\emptyset} = 0. \qquad 6.1.6$$

According to the Biot-Savart law, the linear polarized magnetic field of a loop coil an axis can be defined as:

$$B_1(z) = \frac{\mu_o I\, a^2}{2\,(a^2 + z^2)^{\frac{3}{2}}}, \qquad 6.1.7$$

Where a is the radius of the coil, z is the depth of observation point and μ_0 is the permeability of the free space. Equation 6.1.7 would be equivalent to Equation 6.2.4 for $\theta = 0$ and $r = z$.

6.2 SNR

The Signal-to-Noise Ratio that is generated by a loop coil can be computed as defined in the following expression:

$$SNR(r) = \frac{V_s |M(r).\boldsymbol{B_1}(r)|}{\sqrt{8kT\Delta f(P_A + P_B)}}, \qquad 6.2.1$$

Where M is the magnetization, k is Boltzmann's constant, T is the absolute temperature, Δf is the receiver bandwidth and P_A and P_B are power losses within the coil and sample respectively [2, 3]. These can be defined as follows

$$P_A = \frac{8\,a\,l^2}{\sigma\,\delta^2}, \qquad 6.2.2$$

$$P_B = \sigma\ \omega^2\ \Big(\int_0^{2\pi} \int_0^{\frac{\pi}{2}} \int_0^{b} |A|^2\, r^2\, sin(\theta)\, dr\, d\theta\, d\emptyset + \int_0^{2\pi} \int_0^{\frac{\pi}{2}} \int_b^{\infty} |A|^2 r^2\, sin(\theta)\, dr\, d\theta\, d\emptyset \Big), \qquad 6.2.3$$

Where **A** is the vector potential, ω is the Larmor frequency, σ is the sample conductivity and δ is the coil thickness.

$$SNR = \frac{\omega V_s M B_1(r)/I}{\sqrt{8KT\Delta f\left(\frac{I^2 8b}{\sigma^2\delta^2} + \sigma\omega^2 \times \ldots\right) \ldots \left(\int_0^{2\pi}\int_0^{\pi/2}\int_0^b A^2 r^2 \sin\theta dr d\theta d\Phi + \int_0^{\pi}\int_0^{\pi/2} A^2 r^2 \sin\theta dr d\theta d\phi\right)}} \quad 6.2.4$$

Where M is the magnetization, k is Boltzmann's constant, T is the absolute temperature, Δf is the receiver bandwidth.

We can see that the SNR of a coil is related to its B_1^+ efficiency. However, at high frequencies this reciprocity relationship can be broken, because the receive coil observes the B_1^- component.

6.3 Simulation

The FDTD method was used to simulate the time varying magnetic and electric fields. Each element consisted of one capacitor for impedance matching and eight tuning capacitors, the perfect electric conductors were split into many parts with small gaps for the capacitors which were distributed at eight equally spaced intervals around the square loop. The reason for adding more than one tuning capacitor in the coil is that reduces the electrical coupling (parasitic capacitance) that occurs between the coil and the dielectric of the sample or human tissue [4]. Also the resonance frequency of 300 MHz can be more easily achieved. Moreover, reducing the sample losses caused by the displacement current can be achieved by distributing multiple tuning capacitors. However, resistive losses caused by eddy currents induced in the sample or human tissue are unavoidable [5]. Furthermore, reducing the size of the coil decreased the overall parasitic capacitance and increased the quality factor of the coil. The parasitic capacitance affected the matching impedance when the coil was built in the laboratory.

6.4 Simulation of One-loop and Two-loop Coils loaded with a Muscle Tissue Equivalent Homogeneous Phantom.

The model can be described as the follows: The resolution of the model was 0.5 *mm* in the x direction in the region of the coils and 1.3 *mm* in the y and z directions. All simulations were performed with same grid. The coil was driven with a Gaussian pulse as the source waveform to provide a wide bandwidth frequency response. The loops were simulated as 10 *mm* wide PEC tape and isolated from shorting together with insulating plastic sheet. The coil was loaded with a muscle tissue phantom with body equivalent dielectric properties (conductivity and relative permittivity had constant values of 0.77 S/m and 58.201 respectively). The coil was placed at 10 *mm* distance from the phantom surface. A homogenous phantom was preferred because the character of the electromagnetic field can be observed without perturbation by tissue heterogeneities, as an example the effect of RF inhomogeneity can be obtained with a uniform phantom. Adjusting the relative phase of the dual coil was required to obtain better signal-to-noise ratio (SNR) over a large field of view [6].

6.5 Coupling and Decoupling

Coil coupling has to be considered during the modelling process. When two elements are placed near each other, the magnetic fields from the first element will pass through the second element [7]. The changing magnetic field from the first element will induce an EMF in the second element and vice versa. According to Faraday's law, this is

$$\varepsilon = -(d\Phi_B/dt), \qquad 6.5.1$$

Where ε is the electromotive force EMF and Φ_B is the magnetic flux.

In addition electric fields will also introduce a degree of coupling, which means that the expected geometrical positioning at low frequencies cannot be used. This

problem can be overcome by connecting the first element by a voltage source (1 volt, 50 ohms) and the second element was set at 50 ohms impedance. Simulation results demonstrated that there was very strong coupling between two elements as shown in Figure 6.5-1 (D), which caused the main resonance frequency to split into peaks and it can be said that the mutual coupling between adjacent elements was strong enough to split the resonant peak. The coupling will add noise, decrease the signal to noise ratio and affect the image quality [8]. In the simulation, one of the most difficult tasks was to make two elements invisible to each other. Therefore, reducing the flux linkage from the closest neighbouring element was more challenging.

This was achieved by reducing the coupling between the elements. The literature suggests that the coupling between two elements such as square loops can be minimized to zero by proper overlapping of the elements as mentioned in chapter 3. We found that this could be achieved for square coils by separating the coils by a distance approximately equal to 90% of the side length, while loop coils are separated by approximately 75% of the circle diameter. The simulation shows that the overlap between coils could be adjusted to reduce the coupling as shown in Figure 6.5-1 (E). From the simulation results, the coupling constant k can be calculated based on results shown in Figure 6.5-1 and using the method described in Chapter 3. It was found that k lies between 0.2 and 0.3 with an average of 0.25. It was noted that the overlapping method works well for decoupling two elements as shown in Figure 6.5-1 (F). The coils were tuned to the same frequency, as when using only one element as shown in Figure 6.5-1 (B). This means that the mutual inductance of the elements would have been diminished ($M \cong 0$).

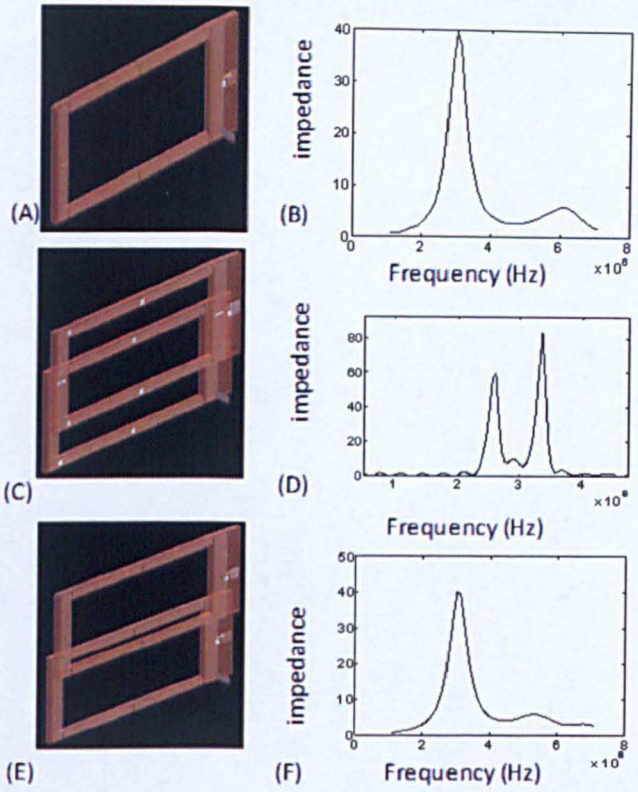

Figure 6.5-1: (A) A single element structure in XFDTD, (B) one element resonant at 300 MHz, (C) a two element structure in XFDTD, (D) the original resonance frequency split by the mutual inductance between two elements in the simulation, (E) a two element overlapping and (F) decoupled by the overlaping technique and resonating at 300 MHz.

6.6 The B_1^+ Mapping produced by One Loop and Two Loops

For safety validation, the B_1^+ distribution and SAR were performed at 298 MHz for one element and an overlapping two-element coil, with voltage source magnitude equal to 1 volt. For calculations with two voltage sources such as two loops, the same amplitude must be used. Net input power driving into one element and two elements were about 2.04×10^{-3} and $4.183 \times 10^{-3}\ W$ respectively. The total power absorbed in the phantom was computed in FDTD. The absorbed power P_{abs} depends on the conductivity of the phantom and is defined as the

following: $p_{abs} = \iiint \frac{\sigma}{2}|E|^2\, dV$. The FDTD simulation showed that the power dissipated in the phantoms are 1.96×10^{-3} and 4×10^{-3} watts which were generated by one element and two elements respectively.

Taking the simulation results a MATLAB program is used to process the results and show the B_1^+ map in Figure 6.6-1. All line profiles were calculated at the same depths for all simulations in order to be able to compare the results. The numerical calculation shown in this work offers a simple approach to make a comparison between one loop and two loops. It can be seen that the magnetic field was higher close to the coil and also that there was a large local B_1^+ generated above the PECs and less B_1^+ between the PECs. B_1^+ was reduced as we moved further away from the probe. An area of low B_1^+ intensity was found between the coils themselves as shown Figure 6.6-3.

Moreover, the magnetic fields cancelled each other out somewhere in the middle and also on the top right of the phantom, as shown in Figure 6.6-1. It can be assumed that when the coil is loaded with the phantom and scanned on the 7T, the same distribution of the B_1^+ will be produced. This will be shown in section 6.14. With regards to the two-loop coil, it had very good coverage in the middle of the phantom and better and more homogeneous penetration of the B_1^+ than the one-loop coil. This is because the fields from two loops are combined, and also the field of view was increased, it is approximately 15 *cm* and 25 *cm* for one element and two loops respectively. When two loops were loaded on a large phantom a good uniform magnetic field and high B_1^+ appeared above the PECs as the current flowed in this region, but less signals appeared between the PECs and also a null appeared in the centre of the coil. When adding two-loop, the null disappeared in the same area as shown in Figure 6.6-3.

It can be concluded that two loops behaved as a one-loop coil and also the magnetic field produced by two loops acted as three parallel strips just in this plane, as discussed in the previous chapter. The efficiency of the coil was calculated as shown in Figure 6.6-4 and Figure 6.6-5, using the equation

presented in chapter 3. As the efficiency is a function of transverse magnetic field, it has the same distributions of the B_1^+. The coil has high efficiency in the area near the PECs, directly below the elements and it decays between the PECs. The efficiency decreases more rapidly with increasing depth from the surface of the coil as shown in Figure 6.6-5.

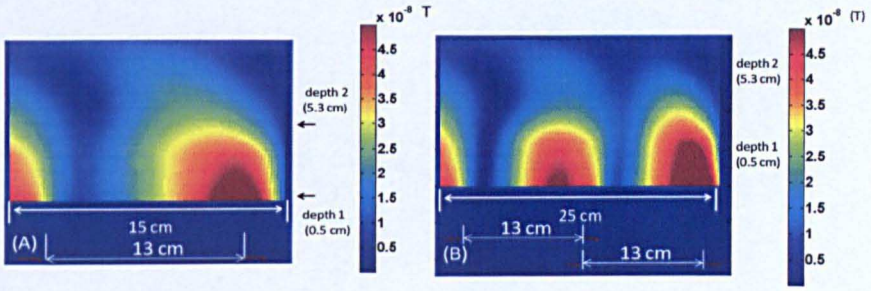

Figure 6.6-1: The B_1^+ generated: (A) one element and (B) two elements.

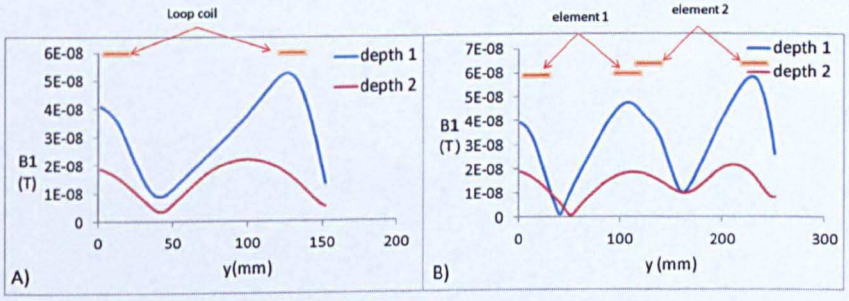

Figure 6.6-2: The line profiles of the B_1^+ in depth close to and further away from the coils, (0.5 *cm* and 5.3 *cm*, respectively).

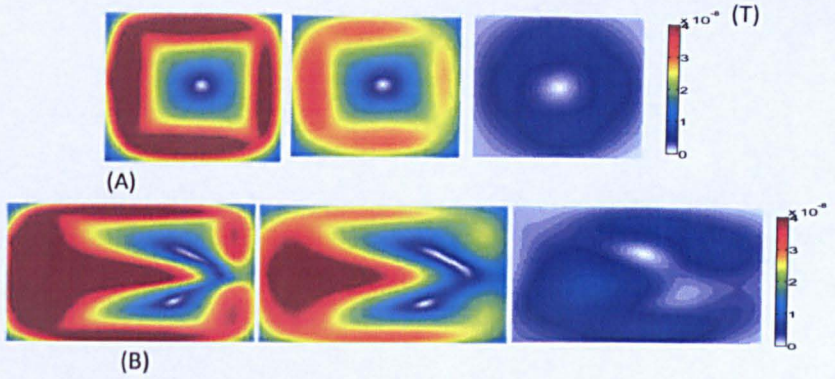

Figure 6.6-3: The B_1^+ generated in the coronal plane: (A) one element and (B) two elements (0 and 90 degree out of phase): in the surface of the phantom, in the middle of the phantom and in the end of the phantom.

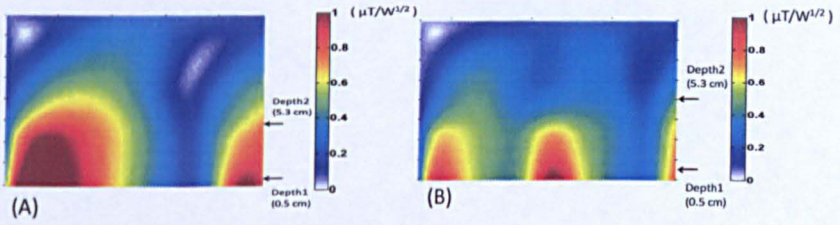

Figure 6.6-4: The efficiency mapping of one element and two elements in the transverse plane, in linear scale and normalized for 1W delivered power.

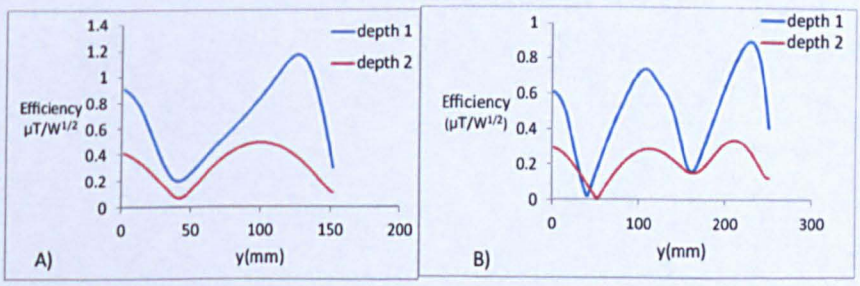

Figure 6.6-5: The lines cross of the efficiency mapping close to and further away from the coils generated by one loop and two loops.

We can now compare the results of the simulations. A comparison between one loop and two loops can be clearly seen when the coils were loaded in the homogenised phantom, a summary of these results is shown in Figure 6.6-6. However, it is useful to quantify the uniformity which can be a measure of the coils' RF fields. To do this a histogram of the B_1^+ is plotted. A good homogeneity would result in a narrow distribution. If we compare Figure 6.6-6 (A and B), note that the result from the two loops improves field homogeneity in comparison to one loop coil. Therefore, the improvement we can make to the field produced by the coil is to add a second identical element.

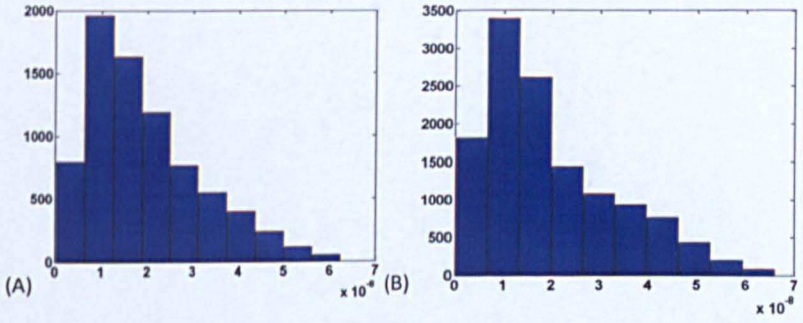

Figure 6.6-6: The histograms show the distribution of data values (B_1^+) generated: (A) one element and (B) two elements.

6.7 Conduction Current Magnitude (CCM)

As has been described in the previous sections it is important to know how the current flows on the surface of the coil conductors. In this section, we present the current distribution in two dimensions as the CCM mapping. The coil was driven in quadrature by two unit power sources 90 degrees phase difference with a sinusoidal waveform and frequency of 298 MHz. The simulation was run until the system reached a steady state. The CCM was obtained from data sets in XFDTD. Figure 6.7-1 shows the current distribution equally on the PEC. It can be seen that hot spots appeared in the regions where the capacitors are connected to the perfect electric conductors. In these areas a high potential difference between two points was generated. This caused an increase to the electric fields in these locations as

shown in Figure 6.7-2 and Figure 6.7-3. These are sometimes referred to as electric conservative fields as opposed to induced fields.

When distributing n capacitors in the loop coil, the voltage and electric field generated by each capacitor is v_i and E_i then the total voltage and electric field generated by each capacitor in the loop can be given by:

$$V_T = \sum_{i=1}^{n} v_{i,} \qquad 6.7.1$$

$$E_T = \sum_{i=1}^{n} E_i. \qquad 6.7.2$$

The above equations have described the physical principle. Therefore, by looking at the previous equations, we can make some important conclusions. Distributing more than one capacitor has the advantage of the result reported here. The electric fields can be distributed in many locations instead of in one place when using one capacitor [9]. This means that electric field generated in many locations is smallest because the total electric field should be divided by the number of capacitors distributed in the loop. Therefore, this will decrease the localised tissue heating in these locations and reduce electrical coupling with the tissue.

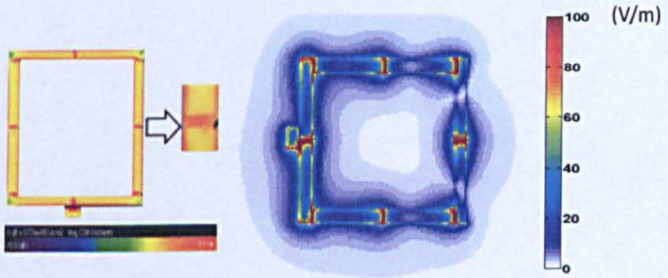

Figure 6.7-1: CCM (A/m) on the left and an electric field (V/m) on the right.

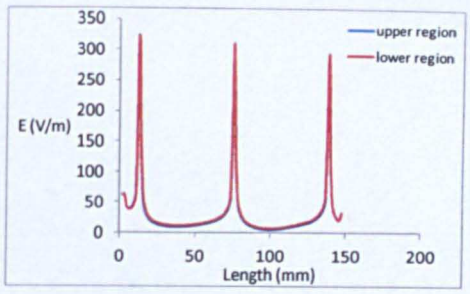

Figure 6.7-2: An electric field (V/m) line profile across three capacitors in the upper region and three capacitors in the lower region.

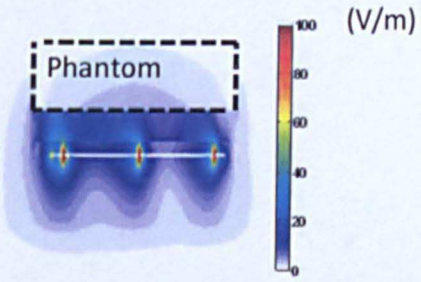

Figure 6.7-3: The electric fields generated in the locations of the capacitors. Cross section taken through the phantom and conductor.

6.8 SAR Generated by One Loop and Two Loops

SAR calculations for the simulations were performed for the phantom and also for the female pelvis model. Figure 6.8-2 (A and B) shows the distribution of the SAR for the simple phantom. There was a higher SAR produced for a B_1^+ of 1 μT above the PECs, which means that more electric fields were generated in this region and very low SAR appeared between the PECs in the y direction. The simulation results of two loops demonstrated that the locations of the highest SAR were on the surface of the phantom in the region close to the loops. Therefore, when we scan a human, the coil should be placed 1 *cm* from the tissue and spacer material should be put underneath the coil to avoid increasing the local SAR and

casing a temperature rise in the tissue. Attention should be paid to all the safely aspects.

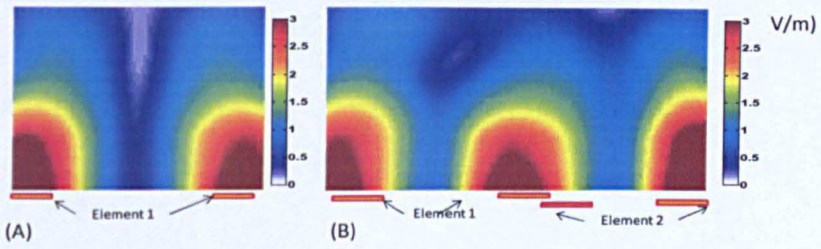

Figure 6.8-1: The Electric fields mapping in *x-y* plane and the maximum E directly below the elements produced by (A) one loop and (B) two loops. Each element was driven by 1 volt.

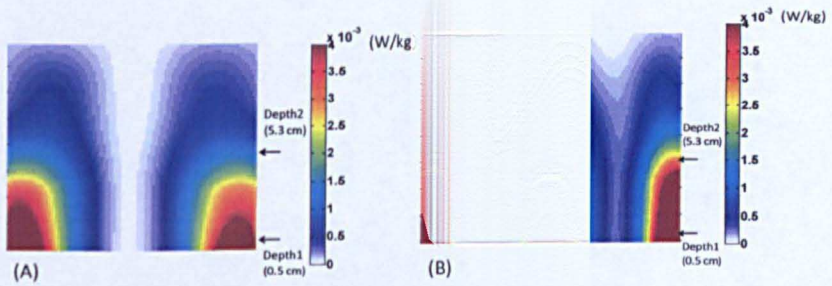

Figure 6.8-2: The SAR mapping in *x-y* plane with the maximum SAR directly below the elements produced by (A) one loop and (B) two loops.

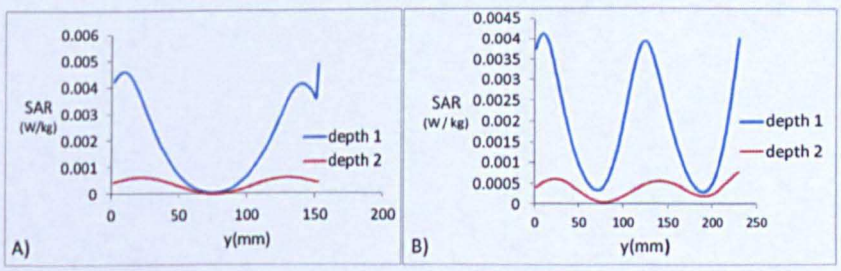

Figure 6.8-3: The line cross of the SAR mapping in depth close to and further away from the coil, (0.5 *cm* and 5.3 *cm*, respectively).

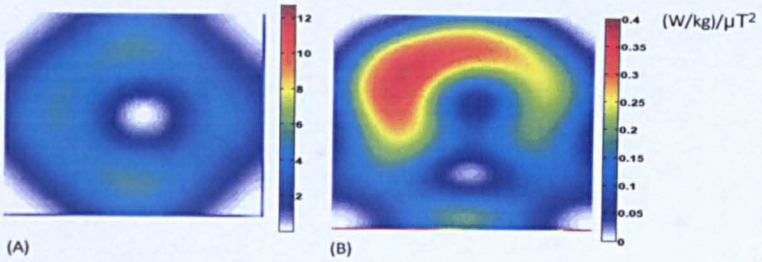

Figure 6.8-4: The local SAR per B_1^{+2} mapped in the coronal plane with the maximum SAR/B_1^{+2} directly below the PECs and capacitors produced: (A) one loop and (B) two loops: in the middle of the phantom.

6.9 The Loop Coil loaded with Human Pelvis Model

The loop coil was considered by loading it on the human pelvis model as shown in Figure 6.9-1.The loop dimensions were 14 by 14 cm^2 and made of PEC, and 8 tuning capacitors were used (7 capacitors = 7 pF and 1 capacitor = 5 pF and one capacitor for impedance matching =100 pF). The coil was placed very close to the surface of the pelvis at about 10 *mm* from the coil and then it was tuned at 300 MHz.

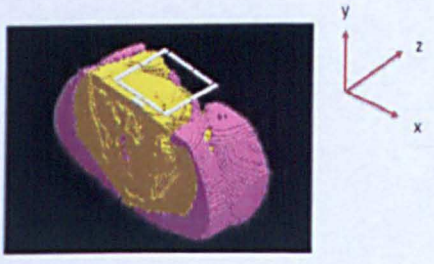

Figure 6.9-1: The loop coil loaded on the pelvis model.

6.10 The B_1^+ Mapping

The coil was driven in single mode at 300 MHz, so that the average wavelength in the pelvis was estimated at 13.1 *cm*. The simulation results showed that the magnetic field B_1^+ was strong close to the loop and it weakened as we moved

further away from the coil in the pelvis as shown in Figure 6.10-1 and Figure 6.10-2. It can be expected that during the reception, a voltage is induced in the loop by the precessing nuclei and the voltage will be very strong when the nuclei are closer to the loop, and as a result the amplitude of the magnetic field decreases as the distance between the loop and the pelvis increases and also the sensitivity distribution depends on the geometry of the coil as shown in Figure 6.11-1.

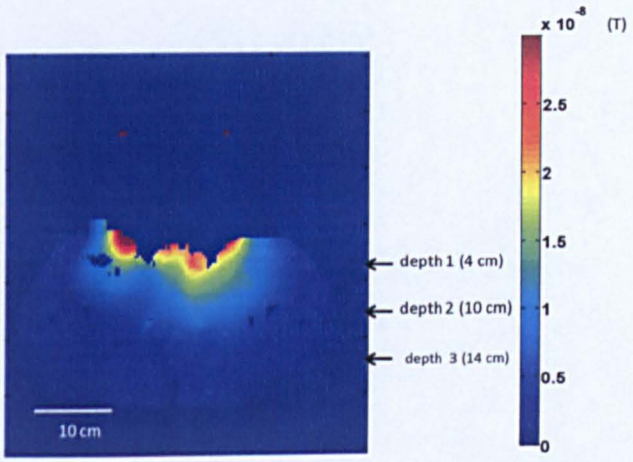

Figure 6.10-1: The B_1^+ produced by the loop coil.

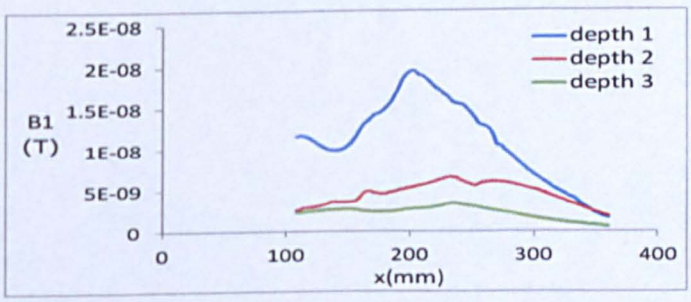

Figure 6.10-2: The line profile of B_1^+ in depth: depth (1) (4 *cm*), depth (2) in the middle of the pelvis (10 *cm*) and depth (3) in the end of the pelvis (14 *cm*).

6.11 Efficiency

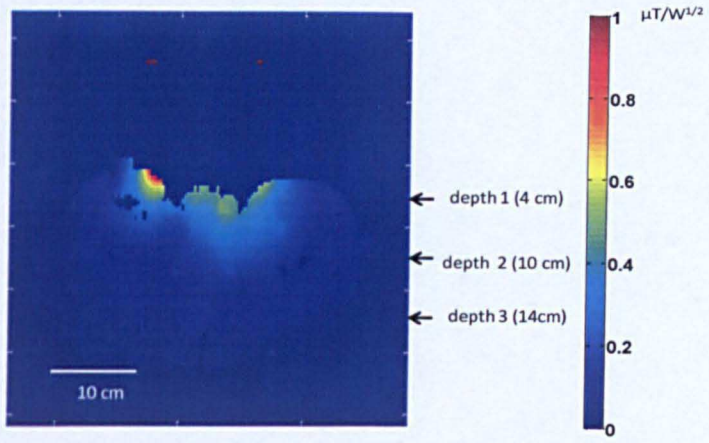

Figure 6.11-1: The efficiency in the transverse plane of the loop coils, in linear scale and normalized for 1W delivered power.

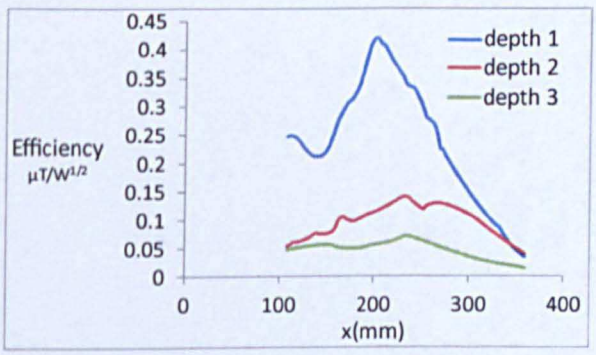

Figure 6.11-2: The line profile of efficiency in depth, normalized for 1W delivered power.

6.12 Specific Absorption Rate (SAR)

The plots of the SAR produced by the loop coil inside the pelvis model show that the highest the SAR were generated in near field region. Therefore, the locations of the highest SAR were on the surface of the pelvis, and in the area close to the loop coil. It is necessary to introduce a maximum of the SAR; the profiles are taken in the regions of the SAR maximum and in depth. It can be seen that the

amount of SAR reached a peak and then dropped dramatically from 2E-3 (watt/kg) close to surface of the pelvis to 2E-4 (watt/kg) in the end of pelvis as shown in Figure 6.12-2.

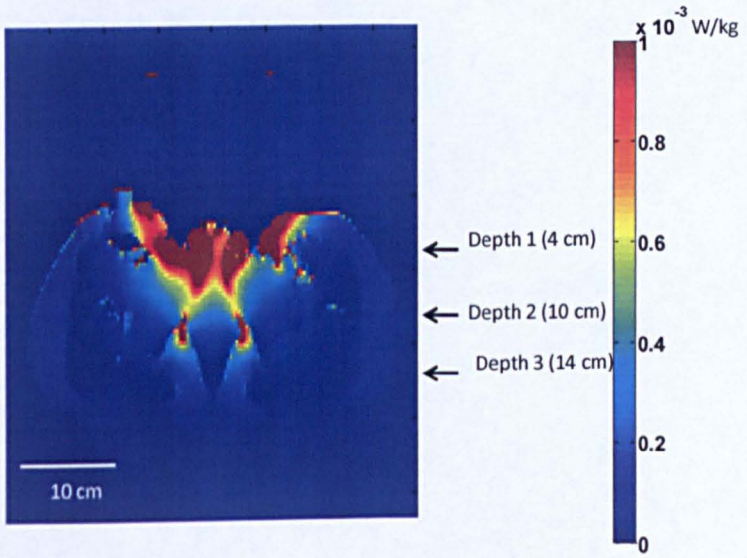

Figure 6.12-1: The SAR mapping on the pelvis.

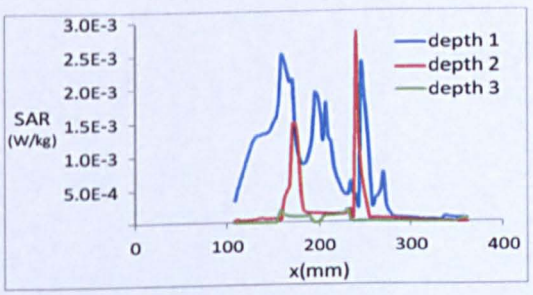

Figure 6.12-2: The line profile of SAR in three regions: near field (4 *cm*), middle (10 *cm*) and in the end of the pelvis (14 *cm*).

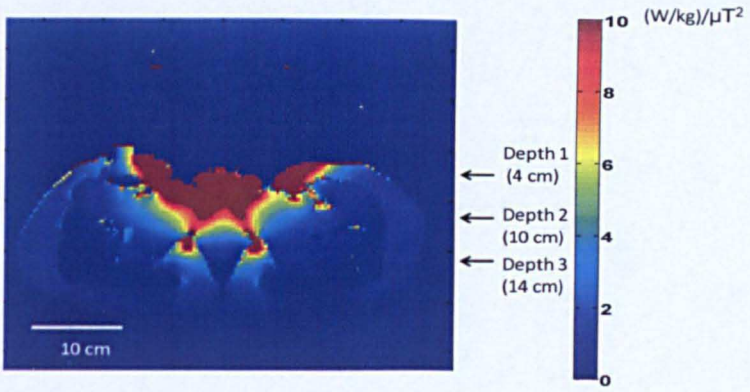

Figure 6.12-3: The SAR per B_1^{+2} distributions on the surface of the pelvis.

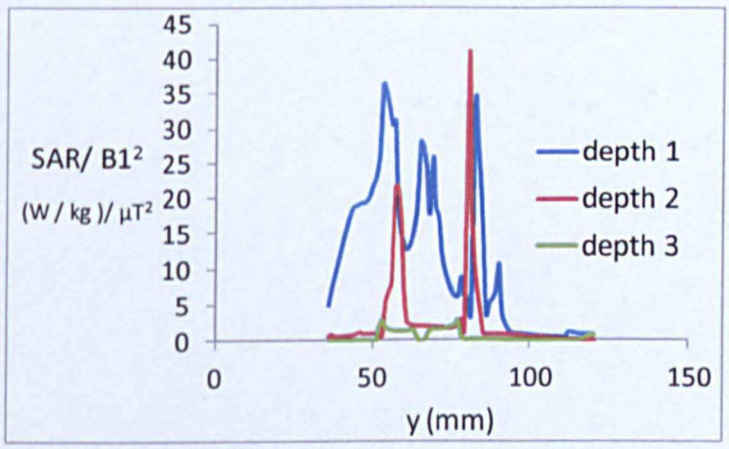

Figure 6.12-4: The line profile of the SAR per B_1^{+2} in three regions: near field (4 *cm*), middle (10 *cm*) and in the end of the pelvis (14 *cm*).

6.13 Coil Construction

The coil was built in an electronic laboratory. It was designed to be similar in shape and dimensions as in the simulation as shown in Figure 6.13-1. Each element was designed as a square loop. Two square-loops coils were built with dimensions of $14\ cm \times 14\ cm$ and a 10 *mm* wide copper tape. Each coil was

individually tuned and matched. The component values used for tuning the coil were found to be $C_1 \rightarrow C_7 = 5.7\ pF$ and $C_8 = 3.3\ pF$.

If the coils are placed near each other, the mutual inductance M among the elements causes the main resonant frequency to split into peaks. This was observed on a network analyzer. It is extremely important to diminish the mutual inductance. This is because the coupling results in a loss of sensitivity at the frequency f_0. There are different techniques to decouple the elements such as the overlapping technique, the interactions between the coils reduced by overlapping adjacent coils and the coils were tuned at 298 MHz.

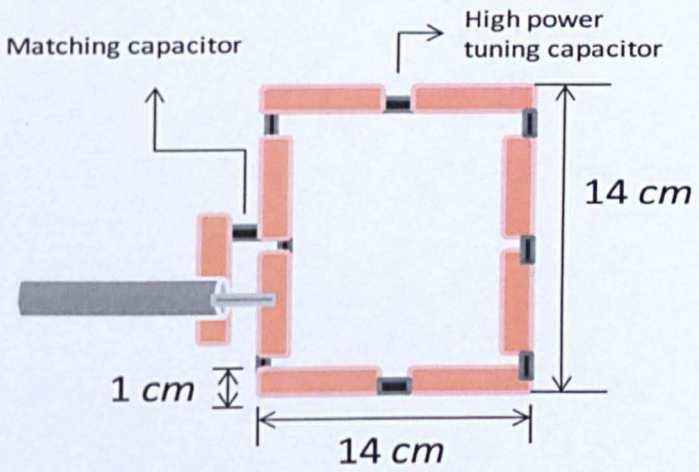

Figure 6.13-1: The schematic view of loop coil.

The coil was tested on the workbench before it was used in the 7T. Validation of the coil involved measuring the quality factor using a network analyzer by using two search coils perpendicular to each other. The quality factor for a loaded coil will be smaller than the quality factor measured without a sample. The coil had an unloaded Q to loaded Q ratio of 74/14 when the loop was loaded with two phantoms. The real resistance of the coil can be estimated by using this formula.

$$R = L\omega/Q. \qquad 6.13.1$$

We assume that the imaginary impedance diminishes as the coil is tuned at 298 MHz. We used RLC lumped components to estimate the equivalent inductance of the coil circuit for tuning at a resonance frequency. The coil was designed to work at 298 MHz and has an inductance of 437.9 nH. The unloaded and loaded coil, real resistances were calculated using the equation 6.13.1 and found to be 11 and 58 ohms respectively. Experimentally, it would appear to be significantly less or greater than the estimate above. This is only an approximation, not an exact value.

6.14 Phantom Imaging

This section refers to the assessment of the loop coil. MRI experiments were performed on a 7T (Philips scanner) system. The loop was placed on two homogenous phantoms (8.5 *cm* diameter, 17 *cm* in length) filled with a solution of 9 g/ml NaCl, and then the coil was matched, tuned and then it was connected to a linear interface box. Transverse MRI images were obtained by using the following parameters: a Fast Field Echo (FFE) technique, with repetition time TR of 30 *ms*, an echo delay time TE of 4.9 *ms* and flip angle of 15 degree. Figure 6.14-1 shows images of two phantoms, the signals intensity in the region where the coil is closest to the phantoms is very high in comparison to other regions. This indicates that the sensitivity decreases with increasing depth as we noted in the simulation. There is a dark line in the images, this due to cancellation of the B_1^+ in these regions.

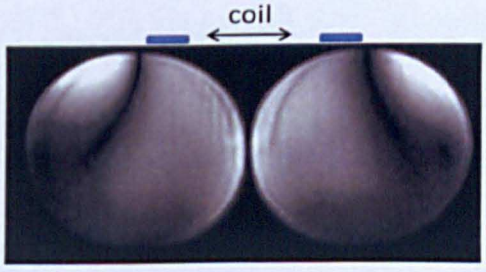

Figure 6.14-1: Images of uniformity phantom (8.5 *cm* diameter, 17 *cm* in length), obtained with the loop coil (T_X/R_X).

6.15 *In Vivo* Imaging

Data were acquired on the Philips 7T MRI scanner using a square coil that was designed and built at the MRI centre. The surface coil was used for imaging the knee. Some of the *in vivo* MRI images were obtained from a healthy volunteer as shown in Figure 6.15-1. The coil was connected to the linear interface box and placed about 1 *cm* from the knee. The FFE technique was used with the following parameters: a repetition time (TR) of 17.1 *ms*, an echo time (TE) of 4.9 *ms* and a flip angle set to 20 degrees.

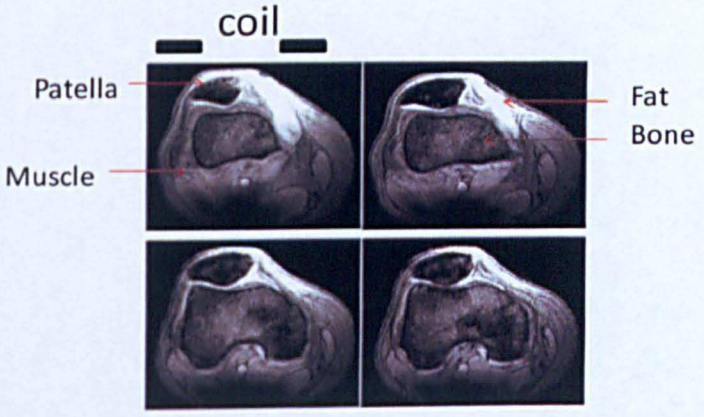

Figure 6.15-1: axial MRI images of the knee in a normal volunteer at 7T.

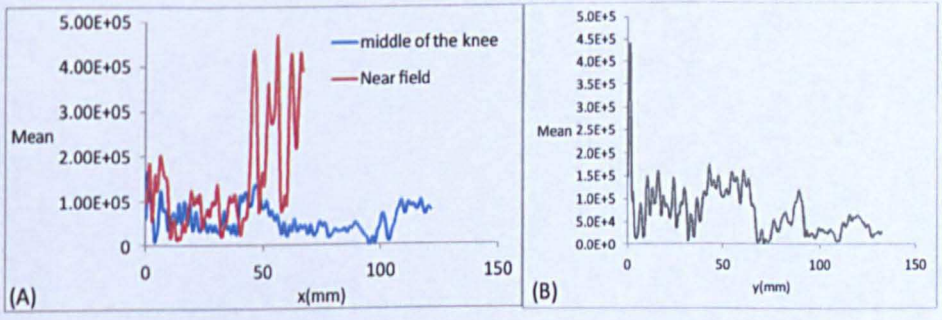

Figure 6.15-2 : (A) The mean signal in horizontal cross section close to the knee and in the middle of the knee, (B) in vertical cross section of the image.

6.16 Discussion

We have shown through simulation the one loop and two loops can be tuned to resonate at 300 MHz and then produce a huge B_1^+ field in the near field region as shown in Figure 6.6-1 and Figure 6.6-2. The two elements were driven 90 degrees out of phase. We generated a phase difference between the currents that flowed in each element.

In the phantom study, the efficiency and FOV was analyzed. The results indicated that a two-element coil will be able to improve the field of view. In order to determine this, two-loop coil was compared to one loop coil. The two-loop covered about 25 *cm* while one loop covered approximately 15 *cm*. It was expected that one loop will image a limited area and the field of view is comparable to the dimensions of the coil. So, the coil can pick up signals from the area surrounding the region of interest.

This study has shown that the efficiency of two loops coil shows the desired improvement, compared to a one loop design. The efficiency is increased by adding two elements in horizontal direction and reached a peak close to the surface of the phantom and then dramatically decreased in the end of the phantom and also in the pelvis as shown in Figure 6.11-1. Depth penetration can be defined as efficiency of the coils to detect weak signals. We expected that the maximum depth of visualization is limited.

Furthermore, based on our computed results the high SAR/B_1^{+2} reached a peak of 3.39 and 3.276 $(W/kg)/\mu T^2$ by the one loop and two loops respectively. The calculations shown that the two-element coil had better homogeneity compared to the one element. The coil was constructed in the laboratory for imaging a phantom and human knee at 7T. It was built and developed as a transmit and receive coil and it was tuned to 298 MHz (the proton Larmor frequency of the 7T). We were only able to test one square coil on the scanner. It is hoped that the two-loop version can be used on the 7T when independent drive (2 channel multi-

transmit) becomes available. This will allow the phase shift to be controlled and B_1^+ shimming employed.

Attempts were made to image a healthy human knee and the images demonstrate a good excitation along the knee over approximately a 14 *cm* field of view. Figure 6.15-1 shows axial MRI images of the knee. The structure of the subject was observed and could be easily identified from the images as: clear muscle, fat, bone, vein, and trabecular bone. This indicates that anatomic details of the knee were well visualized. It was found that there was a significant increase in the mean signal intensity close to the coil as shown Figure 6.15-2. This means that the intensity was best in the region where the coil was closest to the knee.

References:-

1. Jackson, J.D., ed. *Classical Electrodynamics*. 1998, John Wiley and Sons,INC.

2. Ocegueda, A. and A. Rodriguez, *A simple Method to calculate the Signal to Noise Ratio of a circular shaped coil for MRI.* Concepts in Magnetic Resonace 2006. **28 A** (6).

3. Rojas, R. and A.O. Rodriguez, *A simple Numerical Method to Compute the signal to noise ratio of a magnetic resonance imaging surface coil.* Progress in electromagnetics research 2009. **7**: p. 109-122.

4. Kwok, W.E., J. Z, and G. Seo, *A four element phased array coil for high resolution and parallel MR imaging of the knee.* Magnetic Resonance imaging, 2003. **21** (9): p. 961-967.

5. Kumar, A., W.A. Edelstein, and P.A. Bottomley, *Noise Figure Limits for Circular Loop MR Coils.* Magnetic Resonance in Medicine, 2009. **61**: p. 1201–1209.

6. Wei, J., J. Yuan, and G.X. Shen, *Effect of Tuning Capacitor Placement on Mutual Coupling for MRI Array Coils.* Magnetic Resonace Engineering, 2006. **29B (1)**.

7. ROEMER, P.B., P.S. Souza, and O.M. Mueller, *The NMR Phased Array.* MAGNETIC RESONANCE IN MEDICINE, 1990. **16**: p. 192-225.

8. Mark, D.Y. and T. Connick, *Prostate MR Imaging at 3T with a Longitudinal Array Endorectal Surface Coil and Array Body Coil.* magnetic Resonace Imaging, 2008. **27**: p. 1327-1330.

9. Hoult, D. and R. Deslauriers, *A High-Sensitivity, High-B1 Homogeneity Probe for Quantitation of Metabolites.* Magnetic Resonance in Medicine, 1990. **16**: p. 411-417.

Chapter 7

Dipoles as MRI Transmit and Receive Probes

7 Introduction

This chapter will discuss in detail the stages involved in the design and building of dipole probes. It focuses on the development of RF dipole probes that can be used to overcome several of the problems associated with loop coils and strip-line geometries such as inhomogeneity and interference patterns. This approach shows that when imaging a far field region a very good image quality can be obtained whilst maintaining low SAR levels.

In the previous chapters conventional loops and strip lines coils were designed and tested. In this chapter five new dipole geometries were developed for use at 7T. Theoretically, the electromagnetic field of an antenna can be divided into a near- field and far-field regions. Up until now the majority of RF coils have been designed as near field antennas such as loops and strip lines coils. The coils produce a large magnetic field in the near field region. This is good when the Region of Interest (ROI) is located close to the probe. However, at high frequencies most of the ROIs are located at a depth similar to one wavelength, which is a major problem because as frequency increases the wavelength becomes shorter than the dimensions of a sample volume [1]. This is a significant problem when imaging human organs located deep within the body such as a female pelvis (uterus).

Previous research suggested that using a dipole can overcome these problems [2, 3]. It can be shown that the dipole will be suitable for imaging structures deeper

in the human body than conventional coils, as the electromagnetic energy is expected to propagate more uniformly in the far field regions. A brief overview of the dipole antenna will be given in the following section. The results obtained from the simulations and practical applications are explained. Images of phantoms and *in vivo* were obtained at 7T by using the dipoles.

7.1 Background Theory for Dipole Probes

The aim of this section is to describe the electromagnetic wave emitted by an antenna. The dipole antenna can be designed to emit and/or receive electromagnetic energy. It can be made in various shapes and sizes such as an electric dipole which is a centre fed linear antenna. It is assumed to be along the z direction as shown in Figure 7.1-1. It consists of two approximately quarter wavelength conductors and has a narrow gap at the centre for excitation. The currents on the two halves of the dipole are symmetrical. The voltage reaches a maximum V_{Max} at the end of dipole and is zero in the centre. The current reaches a maximum at the centre with a value of I_o and has nodes at both ends, the current phasor $I(z)$ can be assumed to be a sine function [4]. The current is given by:

$$I(x'=0,y'=0,z') = e_z I_o \sin\left[k\left(\frac{1}{2}-z'\right)\right], \quad 0 \le z' \le \frac{d}{2} \qquad 7.1.1$$
$$I(x'=0,y'=0,z') = e_z I_o \sin\left[k\left(\frac{1}{2}+z'\right)\right], \quad -\frac{d}{2} \le z' \le 0.$$

Where $k\left(=\frac{2\pi}{\lambda}\right)$ is the wave number and d is the length of the dipole.

From equation 7.1.1 we would expect that the magnetic field generated nearby to be proportional to the current through the dipole [5]. Also it may be predicted by reciprocity that the receive signal to noise ratio has the same spatial pattern [6], which will be investigated later. From the continuity equation $i\omega\rho = \nabla.\boldsymbol{J}$, the linear charge density ρ' (charge per unit length is constant along each arm of the antenna with value $\rho'(z) = \pm(\frac{2iI_o}{\omega d})$.

The upper and lower sign refer to positive and negative values of z. The dipole moment can be defined as the follows: $p = \int_{-\frac{d}{2}}^{\frac{d}{2}} z\rho'(z)dz = \frac{idI_o}{2\omega}$. The total power radiated is defined as: $P = \frac{Z_o I_o^2 (kd)^2}{48\pi}$ [7]. Moreover, the vector potential **A** and magnetic field **B** generated by the dipole antenna in the cylindrical coordinates can be written as [7]:

$$\mathbf{A}(\rho, z) = \frac{\mu_o}{4\pi} \int_{-d/2}^{d/2} I(z') \frac{e^{-ik\sqrt{\rho^2+(z-z')^2}}}{\sqrt{\rho^2+(z-z')^2}}\, dz', \tag{7.1.2}$$

$$\begin{aligned} \mathbf{B}(\rho, z) &= \nabla \times \mathbf{A}(\rho, z) \\ &= -\frac{\mu_o I_o}{4\pi i \rho}\left[e^{-ik\sqrt{\rho^2+(z-d/2)^2}} + e^{-ik\sqrt{\rho^2+(z+d/2)^2}} - \right. \\ &\qquad \left. 2\cos\left(\frac{kl}{2}\right) e^{-ik\sqrt{\rho^2+z^2}}\right] e_{\emptyset}. \end{aligned} \tag{7.1.3}$$

In general, the magnetic field generated by the dipole antenna can be computed at any point in space by using the Maxwell equation, which can be written as the following:

$$\begin{aligned} \nabla \times \mathbf{B} &= \mu_o \varepsilon \varepsilon_o \frac{\partial \mathbf{E}}{\partial t} + \mu_o \sigma \mathbf{E} \\ &= (i\omega \mu_o \varepsilon \varepsilon_o + \mu_o \sigma)\mathbf{E}, \end{aligned} \tag{7.1.4}$$

From the previous equation, the electric field can be defined as:

$$\mathbf{E} = \frac{1}{(i\omega \mu_o \varepsilon \varepsilon_o + \mu_o \sigma)} \nabla \times \mathbf{B}. \tag{7.1.5}$$

The magnetic and electric fields generated by the dipole in a near and far field region can be expressed as:

$$H_{\emptyset} = \frac{I_o\, l\, k^2}{4\pi} e^{-jk\,R}\left[\frac{j}{k\,R} + \frac{1}{(k\,R)^2}\right]\sin\theta, \qquad 7.1.6$$

$$E_R = \frac{2I_O\, l\, k^2}{4\pi}\eta_O e^{-jk\,R}\left[\frac{1}{(k\,R)^2} - \frac{j}{(k\,R)^3}\right]\cos\theta, \qquad 7.1.7$$

$$E_\theta = \frac{I_O\, l\, k^2}{4\pi}\eta_O e^{-jk\,R}\left[\frac{j}{k\,R} + \frac{1}{(k\,R)^2} - \frac{j}{(k\,R)^3}\right]\sin\theta. \qquad 7.1.8$$

In this research, we are interested in the radiation pattern of the dipole at a distance far from the antenna, which corresponds to a distance R such that $R \gg \lambda$. It can be achieved by keeping only the term varying as *(1/kR)* in the above equations, thus ignoring terms which reduce with R^2 and R^3, which usually dominate the near field expressions [8].

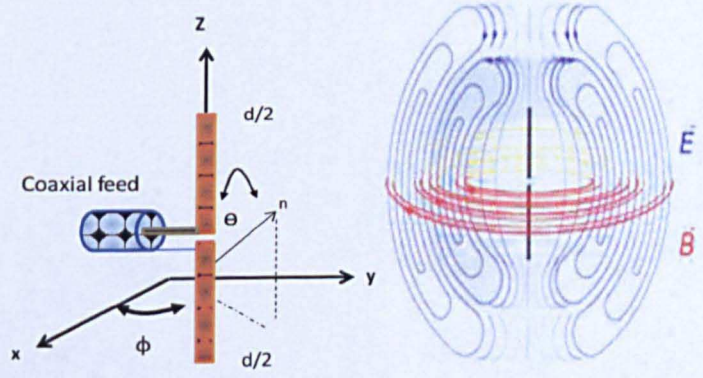

Figure 7.1-1: (left) the dipole, (right) electric field and magnetic field lines surrounding the dipole [9].

Moreover, the length of the resonant dipole can be computed using this equation

$$d = 0.47 \times \lambda = 0.47 \frac{v}{f}, \qquad 7.1.9$$

Where v is the propagation speed on the antenna, which relies on the effective dielectric constant. Voltage and current distributions on a dipole can be described using simulations, which used MATLAB code. Figure 7.1-2 shows voltage distribution on a dipole for a half wavelength. Figure 7.1-3 demonstrates current distribution on a dipole antenna for different wavelengths on an antenna tuned at $d = \lambda/4$ where d is the length of dipole and λ is the wavelength of the oscillating current source. At quarter wavelength the current reaches a peak in the centre fed point. This will be detailed later in the simulation of the dipole antenna.

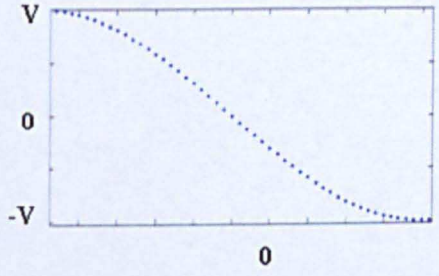

Figure 7.1-2: Voltage distribution on a dipole for a half wavelength.

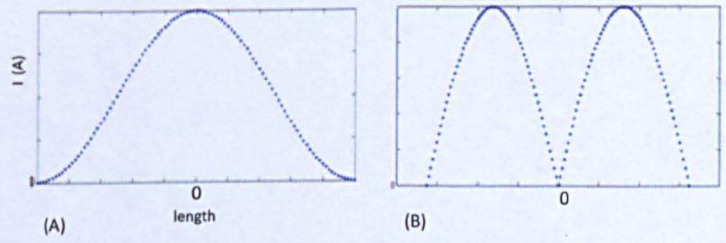

Figure 7.1-3: Current distribution on a dipole antenna for different wavelengths: (A) wavelength/2 and (B) a full wavelength.

The purpose of considering the distributions of the current and voltage is to determine the point impedance. When the dipole is fed at distance z as an example from one end of a half wavelength, the feed point resistance becomes very high while at the centre the impedance is low.

7.2 Simulations

A simulation of an RF dipole was performed to compute the homogeneity, efficiency, electric field, RF field and SAR. The dipole antenna was simulated in water and also using a ceramic material. Four different antenna structures were modelled for imaging at 300 MHz as shown in Figure 7.2-1. These are new designs and they have shown to improve the field of view, homogeneity and efficiency.

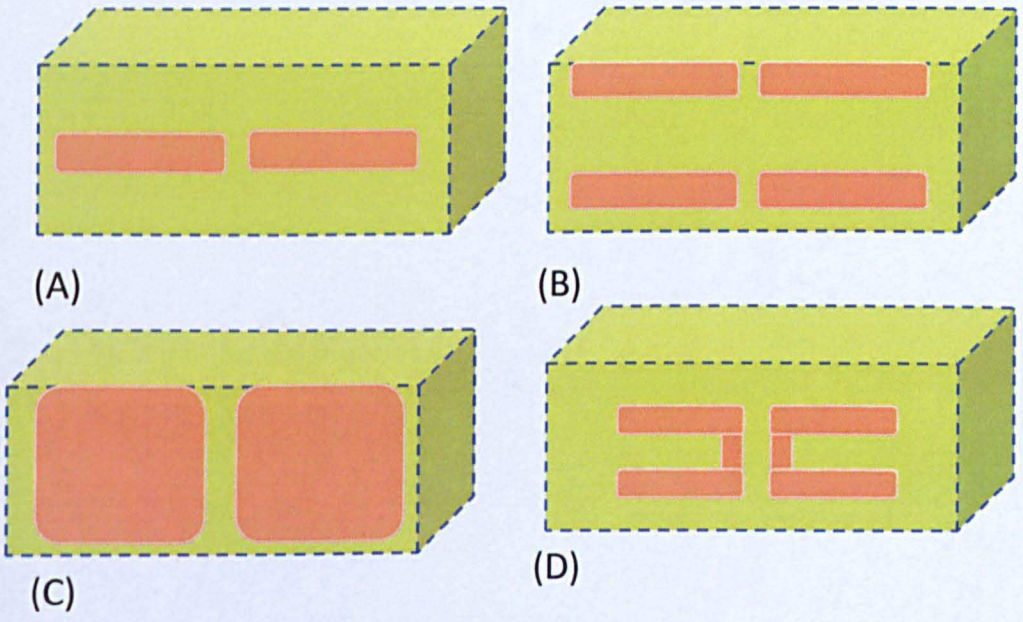

Figure 7.2-1: Four different antenna structures: (A) the structure of the one-strip dipole, (B) two-strips dipole, (C) flat-strip dipole and (D) the dipole array structure.

The copper strips were mounted on the top of the ceramic: The first model was a 10 mm wide strip mounted on top of the dielectric material. The second model

was two strips mounted on the same block material. The third model was a 70 mm wide flat strip placed on the block. The final model was array strips mounted on the block as shown in Figure 7.2-1 (A, B, C and D). There is no mention in the literature about the last three dipole designs.

Results of all simulations and practical applications are compared and discussed in the next sections. All models had the identical dimensions and mesh as well. In this research, the dipole antenna in water was the first to be studied, to obtain information such as the distribution of the B_1^+ and imaging near field and far field regions on the 7 T. Details about modelling and building the dipole antennas will be provided.

7.3 Dipole in Water

In this section we describe how to simulate the dipole antenna in water. It consists of two arms. Each arm is a quarter wavelength long. Figure 7.3-1 and Figure 7.3-2 show the electric circuit and structure of the dipole antenna in XFDTD. The arms of the dipole were simulated using Perfect Electric Conductor (PEC) in the simulation. The dipole was placed in a number of different dielectric materials that have very low conductivities of 0.005 (*S/m*). The coil was driven with a Gaussian pulse as the source waveform to provide a wide bandwidth frequency response. The frequency range of the model was 0 to 18.74 GHz. The cell size was chosen to be 0.5 mm in the *x* direction and 1.5 *mm* in the *y* and *z* directions. Approximate memory required for the calculation was 200 MB.

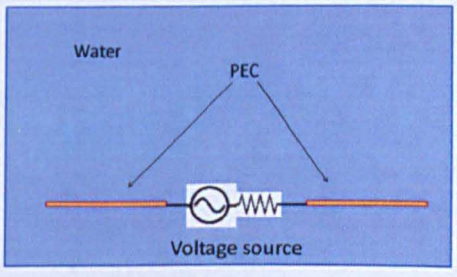

Figure 7.3-1: A diagram of the circuit used to tune the dipole in the simulation.

In this part of this section, we investigate the effect of the dielectric to tune the dipole. It was tuned by adjusting the length of the dipole, there are no electric components such as capacitors in the simulation used to tune the coil. It tuned as a self-resonance at 300 MHz. The dipole was placed in the dielectric material of water and the distance between the surface of the water and the dipole antenna caused a variation of the effective permittivity, which affected the tuning frequency. The table below shows two dipoles placed in the same depth in the simulations, but in different two dielectric materials. It was observed that the permittivity can affect the total length required to resonate the dipoles at a self resonance frequency, the simulation results showed that there is a relationship between the length of the dipole, frequency and permittivity can be expressed as $f = C/2L\sqrt{\varepsilon_{eff}}$, so that the shortest wavelength is 11.5 *cm* in the dipole. The resonant length of the dipole for 300 MHz under loaded condition was found to be 13 *cm* as shown in Figure 7.3-3.

Permittivity	The total length of dipole under unloaded condition(*cm*)	Self-resonance (MHz)
33	13.601	300
76	12.64	300

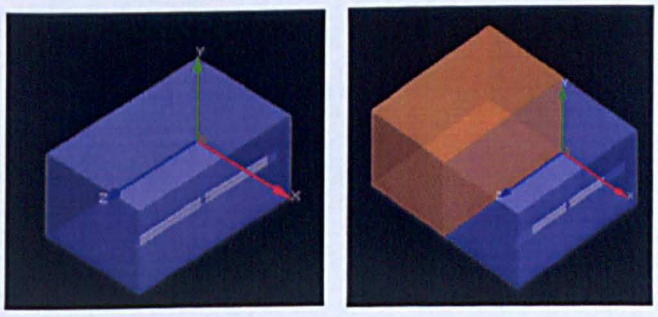

(A) (B)

Figure 7.3-2: The dipole structure in XFDTD: (A) Unloaded and (B) loaded conditions.

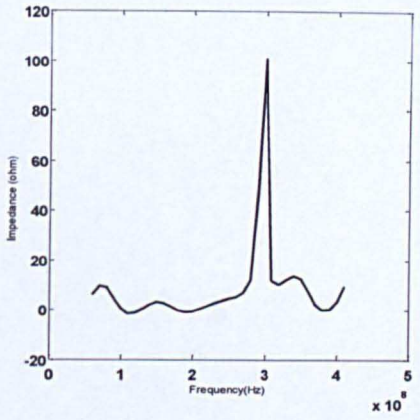

Figure 7.3-3: The dipole tuned at 298 MHz.

7.4 The B_1^+ Mapping

Figure 7.4-1 shows the B_1^+ maps produced by two elements inside the dielectric material. It can be noted that the highest intensity of magnetic fields were generated inside this material, under the two elements. It can be predicted when testing the dipole that the NMR signal will be generated in the water inside the box and the same pattern will be obtained when testing the dipole to image a phantom. Figure 7.4-2 demonstrates that the B_1^+ values were very high close to the dipole, in the region of interest the B_1^+ produced only decayed slowly as shown in Figure 7.4-2.

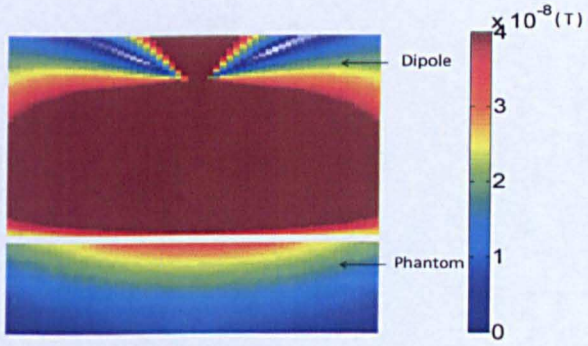

Figure 7.4-1: The $\mathbf{B_1^+}$ mapping in the *x*-*y* plane.

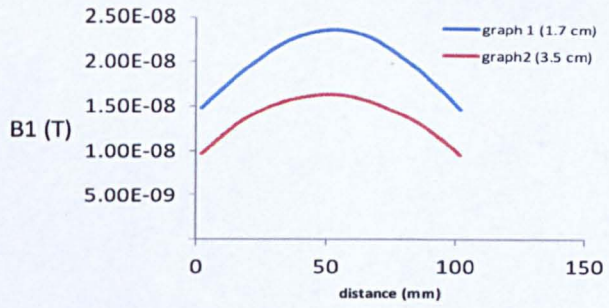

Figure 7.4-2: Computed B_1^+ profiles for different depths in phantom material, (the net input power used for transmission into the dipole was about 1.47×10^{-3} watt).

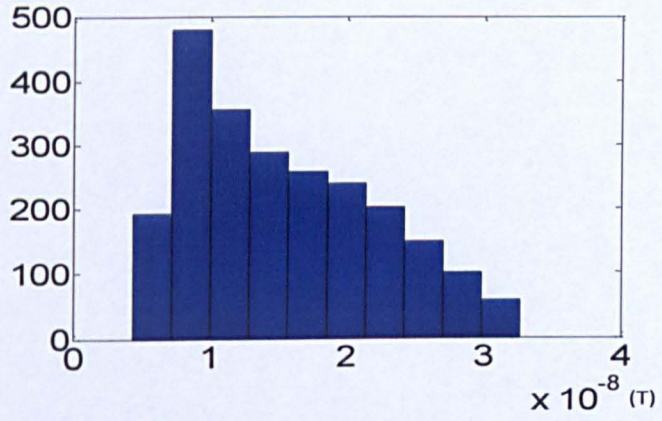

Figure 7.4-3 : The histogram shows the distributions of data values (B_1^+) generated by the dipole in the phantom.

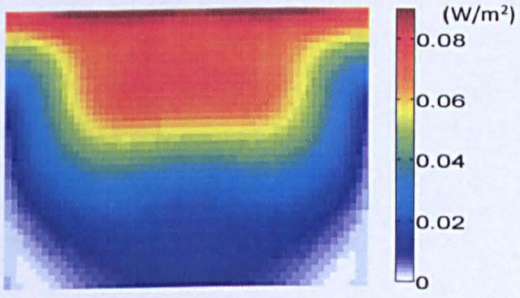

Figure 7.4-4: The magnitude of the Poynting vector generated by the dipole.

7.5 The Dipole Construction

The dipole antenna is a very simple design, which consists of two thin cylindrical conductors that have a total length of half a wavelength. The dipole was placed in a small box, which contained distilled water as shown in Figure 7.5-1. The purpose of using distilled water was to obtain low conductivity to minimize antenna losses and to get high permittivity (close to the relative permittivity of the human body) in order to decrease reflections between the surface of the sample and the dipole.

The size of the box was 16 cm in length, 11.5 cm in width and 9.5 cm in height. In this design, the dipole was tuned to 298 MHz by adjusting the length of the dipole and also by varying the amount of water in the box. This was done to bring the resonant frequency of the antenna to 298 MHz without having to change the dielectric permittivity of the water. However, the effective relative permittivity of the dipole could have been varied by changing the amount of water in the box or adding non-polar or lower permittivity liquids such as methanol. In chapter three we discussed that many different types of a bal-un circuits can be used to convert an unbalanced signal to a balanced signal. In this study a half wavelength coaxial cable was used as a bal-un circuit. Adding it to the dipole had many advantages, such as removing currents flowing on the outer shield of the coaxial cable and reducing the instability of the S-parameter measurement. It was observed that without a bal-un circuit the measured S-parameter relied on the position of the cable. If the cable touched or was placed close to dielectric material, the S-parameter changed. In chapter three we studied and showed how to use the coaxial cable, and the electric half wavelength and full wavelength were computed. Therefore, a $\lambda/2$ length of coaxial cable was used as a bal-un circuit to eliminate feeder radiation.

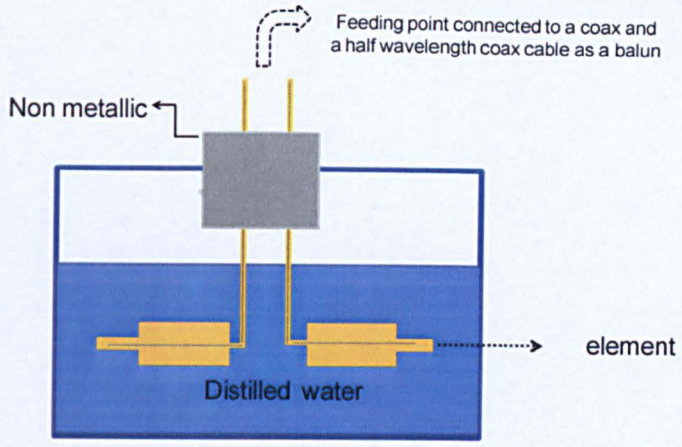

Figure 7.5-1: The structure of the dipole built in water.

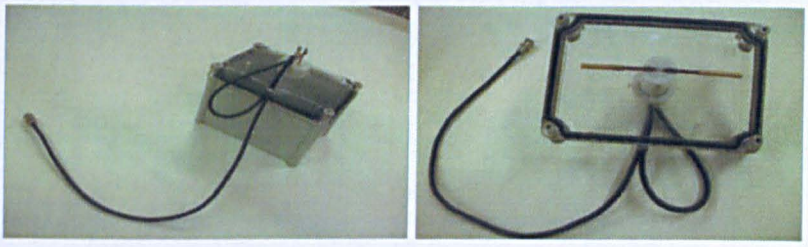

Figure 7.5-2: The dipole built in water.

7.6 Testing the Dipole

The constructed dipole was loaded with two phantoms filled with a solution of 9 g/ml NaCl. This study showed that the dipole was tuned at 298 MHz and matched to 50 ohms without adding any capacitors. Therefore, it can be said that the experiment results agree well with simulation. The antenna was used to transmit RF and receive the MR signal. It was tested on the 7T Philips scanner. It was connected to the linear interface box and used as a transmitter antenna and receiver. Figure 7.6-1 shows that most of the signals were generated from the water. However, it can be said that the antenna covered near field and far field regions. From this design, we can see that the B_1^+ is uniform as demonstrated in Figure 7.4-3. These results point towards the fact that the coil is suitable for the 7T and would improve the image quality above that of surface coils. It can be said that the dipole antenna is a very good transmitter and a receiver.

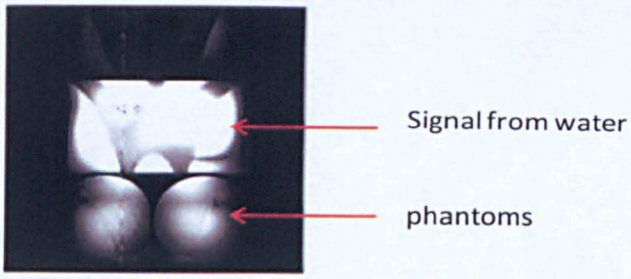

Figure 7.6-1: The images obtained by using dipole as a transmitter and receiver.

The work with this simple system gave confidence that a ceramic based dipole for human imaging would be worthwhile. Using ceramic with high relative permittivity ensured that both the near electric and magnetic fields are inside the block, resulting in the Poynting vector being directed into the sample or patient as demonstrated in Figure 7.4-4. The electromagnetic wavelength travelling in this material was found to be 16.4 *cm*. The dimensions of the ceramic block were very important parameters in the design (such as the length, width and height). In most of our discussions in the next sections, dipole dimensions will be referred in wavelength units. The height of the block must be the quarter wavelength long, about 4 *cm* [2]. This is to minimize the reflections of electromagnetic waves when the coil is placed close to the surface of a sample or a human body.

7.7 Dipole (Ceramic)

A high frequency RF surface coil based on the use of ceramic has been developed for *in vivo* MRI applications on the human pelvis at 7T. The steady state calculations of B_1^+ fields and SAR were performed at 300 MHz with voltage source magnitudes equal to 1 volt. In the phantom study and pelvis model, the FOV, efficiency and uniformity of each dipole was analyzed.

A difference in the B_1^+, efficiency and SAR that was generated by four dipoles can be clearly observed and compared. All line profiles predictions were computed numerically in the same depths, so the numerical method presented in

this work offers a simple approach to make a comparison between the dipoles. Radiofrequency field inhomogeneity, and the field of view and the SAR were major challenges in this research. The latter is a significant RF safety concern.

The purpose of this design study was to increase the FOV, improve the B_1^+ homogeneity and the efficiency of the antenna. It may be improved by adding flat strip, two strips or four strips, or when more than two antennas are joined together such a combination is called an antenna array. Two strips acted as two dipoles connect to the quadrature interface box to produce two signals which have equal amplitudes and 90° out of phases. This mode potentially allowed a sensitivity gain by a factor of $\sqrt{2}$. A partially circularly polarized magnetic field is generated when driving the RF coil in quadrature, but driving the dipole in a single mode as described here with only one strip will generate a linearly polarized magnetic field that is only half as efficient in rotating the spins. This is only exact if the spatial modes are orthogonal.

The dipoles were chosen to work at an electrical-half wavelength. The wave in the dielectric does not have the same wave length as a wave travelling in free space. So the length of whole the structure of the dipole was considerably shorter than the length computed for a signal travelling in free space (the wavelength at 300 MHz in free space is about one meter long).

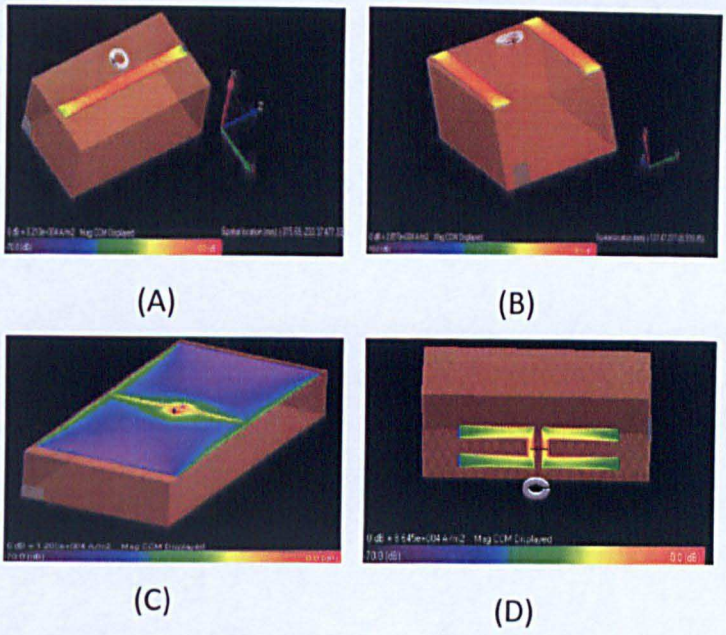

Figure 7.7-1: Four possible structures: (A) the structure of the one-strip dipole, (B) two-strips dipole, (C) flat dipole and (D) the dipole array structure (the total currents divides equally between the four strips).

In this study, the FDTD method was used to compute the electrical half wavelength of the dipoles. One method of tuning the dipoles is as a self-resonant structure in the simulation. A small search loop coil was used to excite the dipoles. We should pay special attention when we excite the dipole using the search loop; the search loop coils were placed in the middle of the strips because the maximum current density occurs at these locations. Hence the search loop located at the centre can pick up the signals at these excitation positions to obtain better simulation results. In order to demonstrate that the interactions between the search loop coil and the dipoles were working, signals were introduced by a search coil into the dipoles.

The coils were tuned at self resonance as follows: the narrow strip dipole, two strips dipole and array dipole tuned at 295 MHz, 298 MHz and 289 MHz respectively. However, when the second strip was added, the resonance frequency was shifted and two strips were tuned at a self-resonance of 236 MHz. It was

found that this shift of the frequency was caused by coupling between the two strips, which also acted as a parallel capacitor. The coupling was very weak in the simulation. Therefore, strong coupling may have occurred if the elements had been placed very close to each other. An attempt was made in the simulation to decouple the two elements by placing two strips away from each other. We found that this could be achieved by increasing the width of the dielectric material or placing two blocks close to each other. These results agree well with work done in the laboratory when the dipoles were exicted by a search loop connected to a network analyzer and tuned to the desired frequencies.

Designing correct dipole function requires an accurate knowledge of the distribution of the current on the PECs. Figure 7.7-1 demonstrates a comparison of the current distributions on the PECs obtained for the four dipoles. The half-wavelength was found to be 14.2 cm and which generate two nodes at each end of the PEC and a maximum current in the middle of the PEC. The impedance of the drive point of a narrow strip dipole is purely resistive at this length. As the array dipole consists of two identical elements and each element consists of two parallel strips. The total current was applied to a single port, the current divides equally by symmetry between the four strips with the same amplitude and phase. Figure 7.7-1 showed that the current distribution would cover all the PEC. Results of the simulation demonstrated that, the current distribution covered almost all the PEC and was distributed over the surface of the coil. This leads to a formation of two currents which reached a peak on the edges of the PEC. There was a lower conduction current magnitude (CCM) in the middle of the flat-strip but the maximum signals appeared to be at the end of the edges. It seems clear that the impedance between the edges is slightly higher than at the end of the edges. There was more magnetic field energy near the edges because there was a change in the amplitude of the current across the conductor. This result agrees well with theory mentioned in chapter five. The second study was to resonate the dipoles at about 298 MHz in simulations by adding a small bridge above the elements, which acted as a circuit which consists of a voltage source, one capacitor for tuning and a second for matching. The dipoles were loaded with the homogeneous tissue

equivalent phantom and tuned at 298 MHz, so that the performance in the coil could be evaluated.

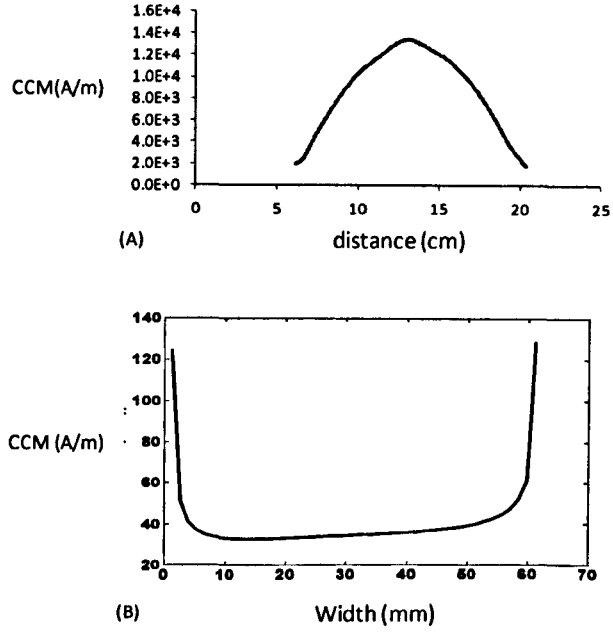

Figure 7.7-2: (A) the CCM (A/m) created on the surface of the narrow strip dipole and (B) the current distribution on the surface of the flat dipole.

7.8 B_1^+ Mapping Generated: One Strip Dipole, Two Strips Dipole, Flat Strip Dipole and Array Dipole

In this section four comparison studies were performed. For SAR safety validation, the dipole models were tuned to the desired frequency then the magnitudes of the positive B_1^+ magnetic field were generated and the SAR calculated as demonstrated in Figure 7.8-1 and Figure 7.9-1. Calculations were performed at 298 MHz with voltage source magnitude equal to 1 volt. SAR is then normalised to that produced for a B_1^+ field of 1 μT.

The net input power used for transmission into the narrow strip dipole and two-strip, flat-strip and the array dipole to generate **H** and **E** fields was about 2 ×

$10^{-3}, 3.67 \times 10^{-3}$, 1.07×10^{-3} *and* 6.8×10^{-4} W respectively. It seems clear that the RF power needed depends on the transmitter coil design and tuning arrangements.

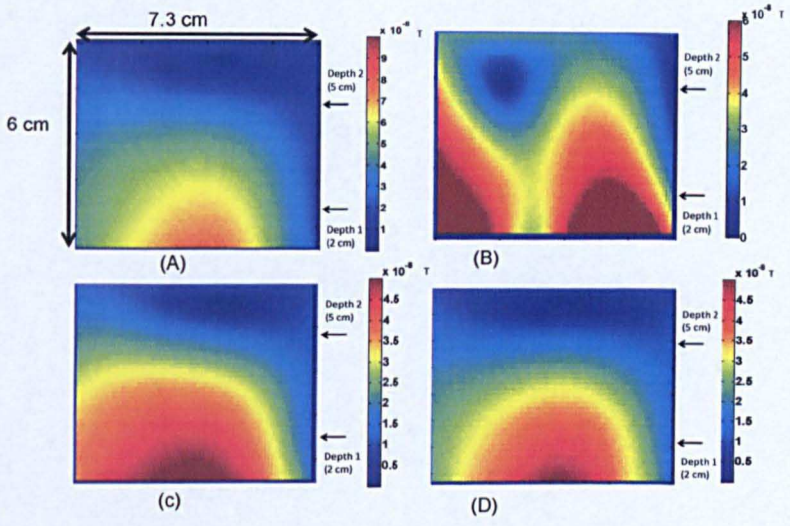

Figure 7.8-1: (A) Mapping of the B_1^+ produced by a narrow strip, (B) two strips dipole, (C) flat strip dipole and (D) array dipole.

7.9 B_1^+ Line Profiles

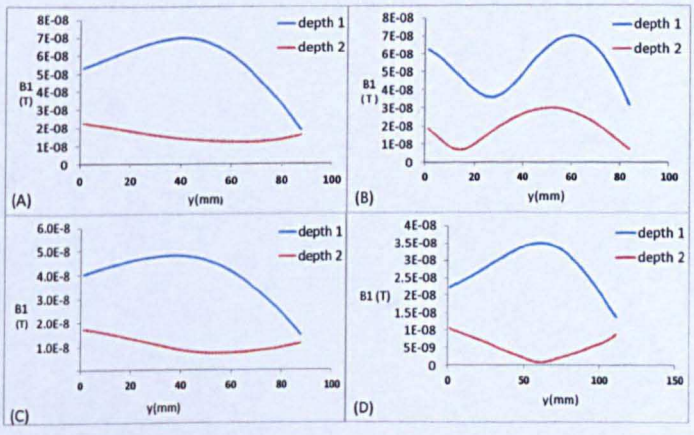

Figure 7.9-1: Computed in depth B_1^+ profiles generated: (A) a narrow strip, (B) two strips dipole, (C) flat strip dipole and (D) array dipole.

As far as the uniformity is concerned, the four dipoles generated different uniformity that can be clearly seen when the dipoles were loaded with the homogeneous phantoms as shown Figure 7.9-2 (A, B, C and D). The distributions of B_1^+ values were plotted as histograms. When calculating the homogeneity for the surface coil, a narrow histogram graph indicates a good homogeneity. Therefore, the two-strip dipole provides more homogenous signal than array strips dipole followed by narrow-strip dipole, while flat strip dipole has the lowest image uniformity. The array dipole and two-strip dipole are the best geometries for obtaining good homogeneity.

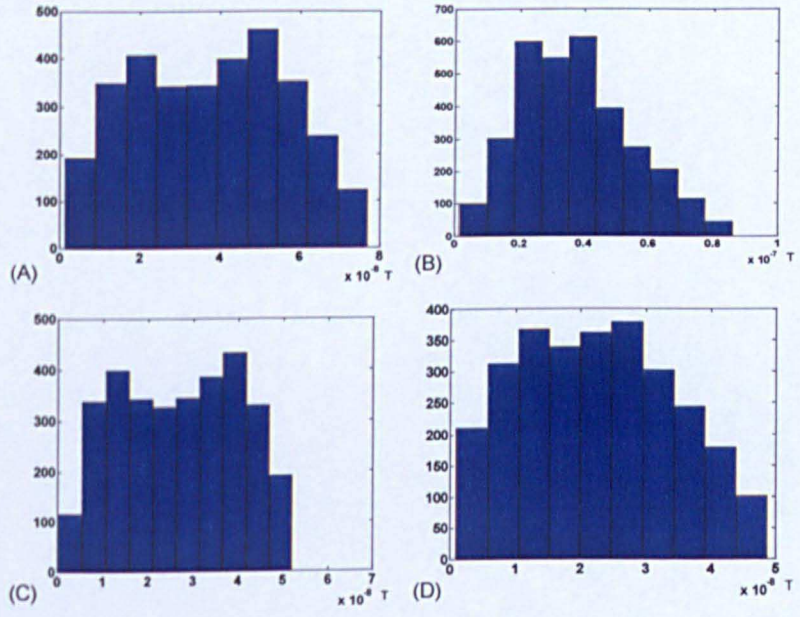

Figure 7.9-2: The histograms show the distributions of data values B_1^+ generated: (A) a narrow strip, (B) two strips dipole, (C) flat strip dipole and (D) array dipole.

7.10 Efficiency Mapping Generated: One Strip Dipole, Two Strips Dipole, Flat Strip Dipole and Array Dipole

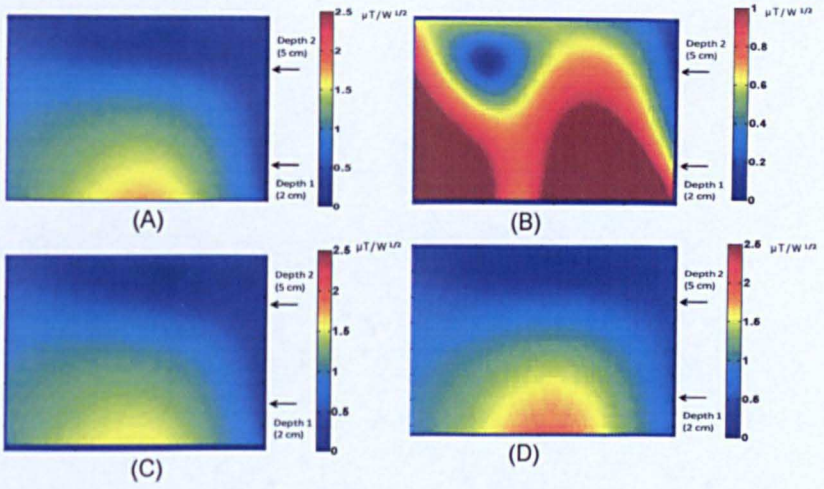

Figure 7.10-1: The efficiency mapping for (A) a narrow strip, (B) two strips dipole, (C) flat strip dipole and (D) array dipole, in linear scale and normalized for 1 W delivered power.

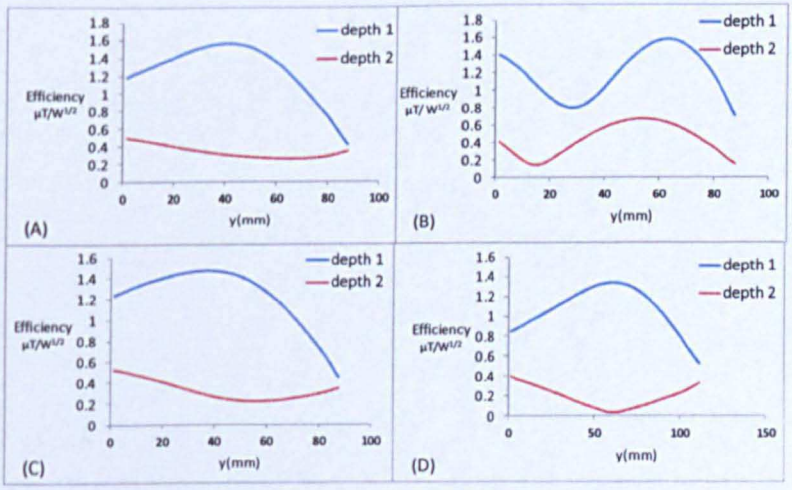

Figure 7.10-2: Calculated in depth efficiency profiles for (A) a narrow strip, (B) two strips dipole, (C) flat strip dipole and (D) array dipole, normalized for 1 W delivered power.

7.11 SAR Mapping Generated: One Strip Dipole, Two Strips Dipole, Flat Strip Dipole and Array Dipole

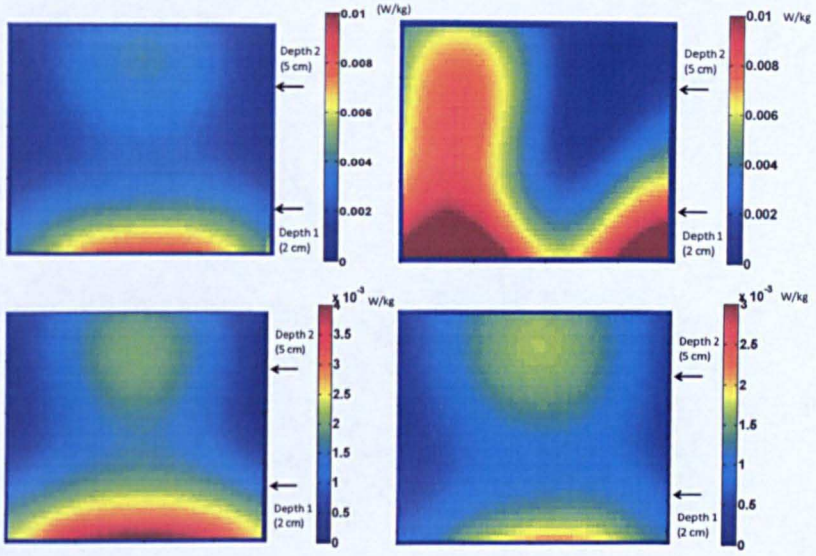

Figure 7.11-1: The SAR distribution (W/kg) generated: (A) a narrow strip, (B) two strips dipole, (C) flat strip dipole and (D) array dipole.

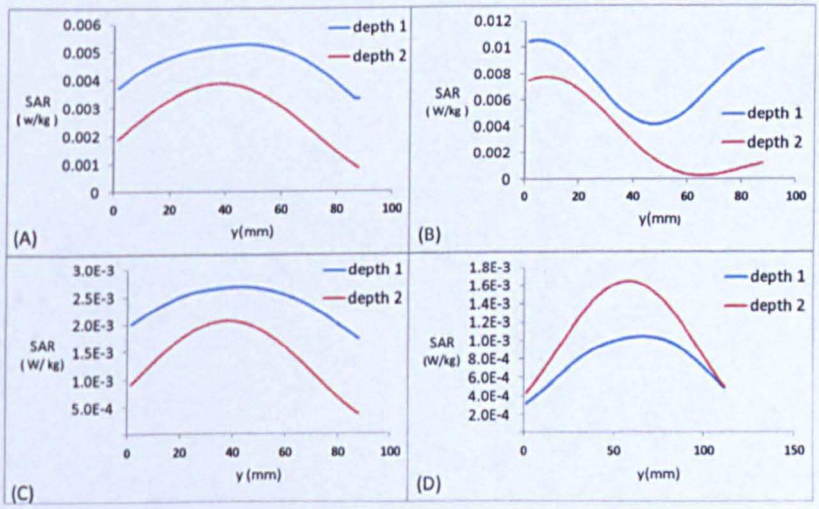

Figure 7.11-2: The line profile of SAR in depth: (A) a narrow strip, (B) two strips dipole, (C) flat strip dipole and (D) array dipole.

7.12 SAR/B_1^2 Mapping Generated: One Strip Dipole, Two Strips Dipole, Flat Strip Dipole and Array Dipole

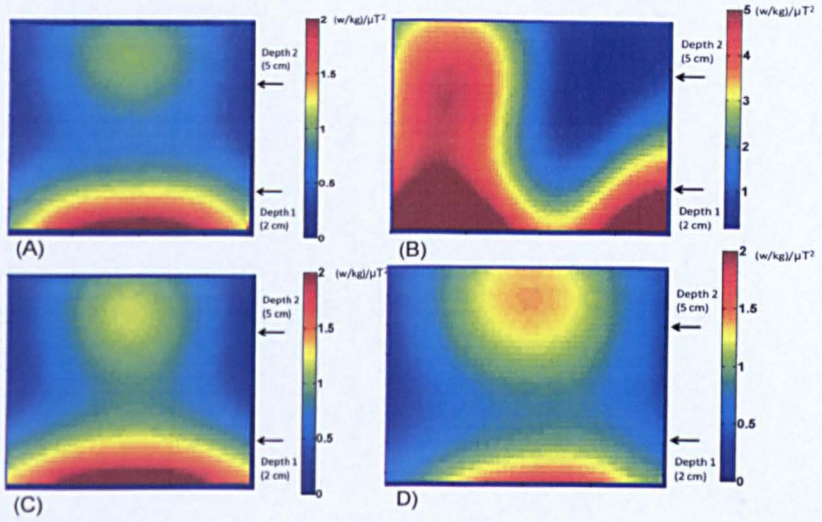

Figure 7.12-1: The SAR per B_1^2 distribution generated: (A) a narrow strip, (B) two strips dipole, (C) flat strip dipole and (D) array dipole.

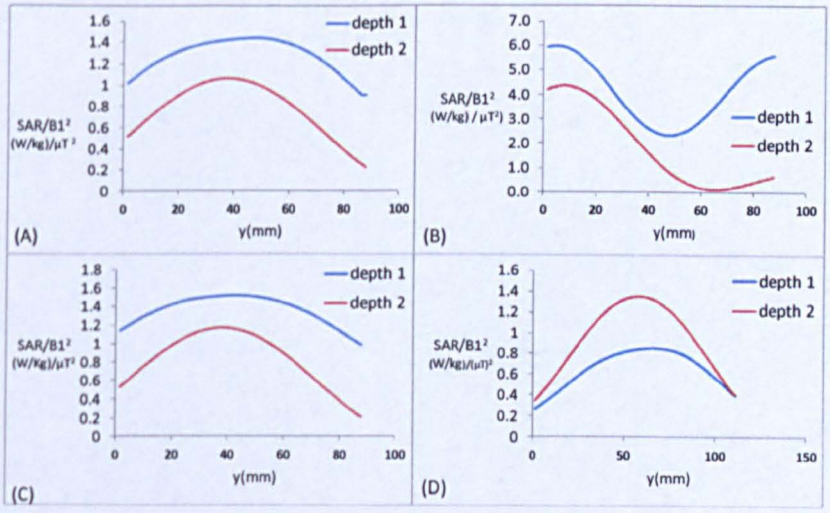

Figure 7.12-2: The line profile of the SAR per B_1^2 in depth: (A) a narrow strip, (B) two strips dipole, (C) flat strip dipole and (D) array dipole.

7.13 Poynting Vector

We computed the Poynting vector by using the same method that was used to generate B_1^+ and the sum of squares root method. The results point towards the fact that the Poynting vectors were oriented towards regions of the phantom as shown in Figure 7.13-1 and Figure 7.13-2. The total Poynting vector below the surface of the phantom was higher, but it started dropping in the end of the phantom as shown in Figure 7.13-3. To demonstrate this we have compared the four dipoles. The two-strip dipole and one-strip dipole provided good distributions of Poynting vector compared with the flat-strip dipole and array dipole. This difference in image intensity distribution due to the excitation net input power is large. Based on our calculated results, the four dipoles have as a main advantage, the B_1^+ transmitted towards deep locations. We obtained good penetrations in order to excite the spins and then detect the signals from these locations. As we discussed already in Chapter 3, the penetration depends on the rf frequency. Moreover, there was distribution of electromagnetic energy in both field regions. Therefore, less electromagnetic energy was absorbed in the near-field region, and some energy was absorbed in the far-field region.

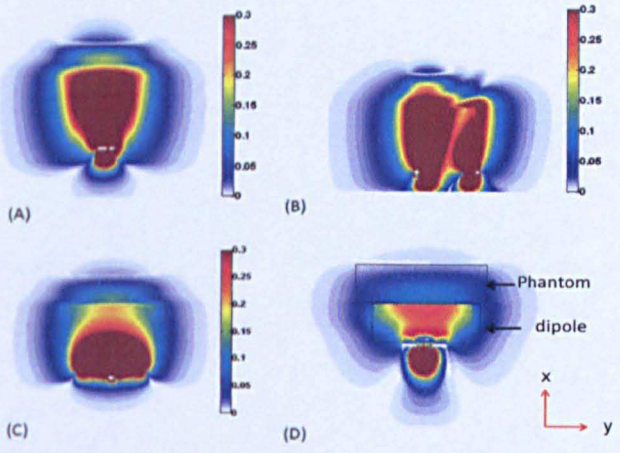

Figure 7.13-1: The magnitude of the Poynting vector generated in the x direction: (A) a narrow strip, (B) two strips dipole, (C) flat strip dipole and (D) array dipole.

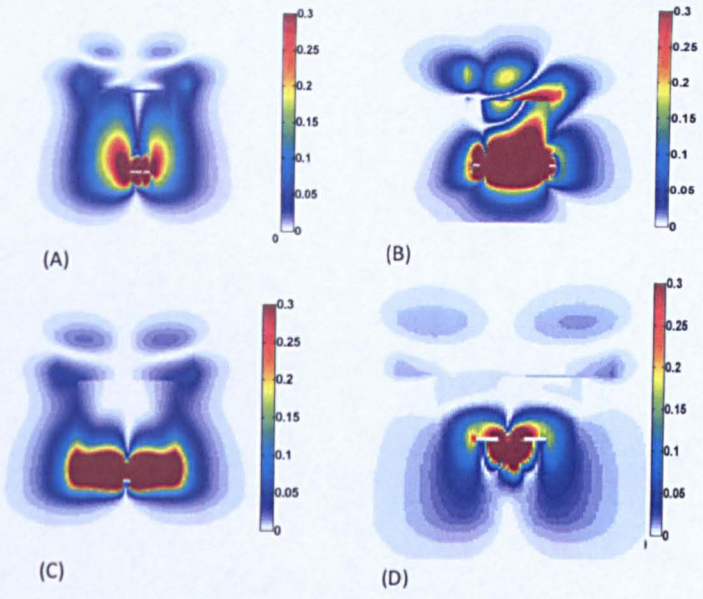

Figure 7.13-2: The magnitude of the Poynting vector mapping generated in the *y* direction: (A) a narrow strip, (B) two strips dipole, (C) flat strip dipole and (D) array dipole.

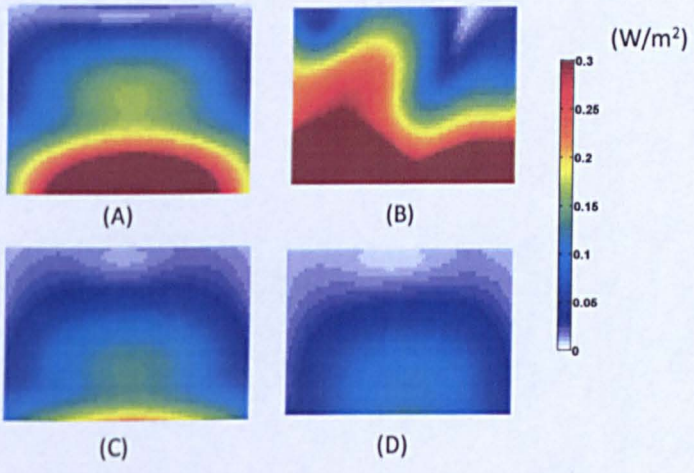

Figure 7.13-3: The total magnidue of the Poynting vector generated: (A) a narrow strip, (B) two strips dipole, (C) flat strip dipole and (D) array dipole.

7.14 Results of Simulation

It can be noted that the narrow strip, flat strip, two strips and dipole array produced a high B_1^+ in near field regions and then the B_1^+ decayed slowly in the depth as shown in Figure 7.8-1, Figure 7.9-1 and Figure 7.9-2. These show that the distribution of the transverse field B_1^+ was homogenous. To make a comparison between the four dipoles, a good homogeneity can be obtained by two strips dipole followed by the array dipole and flat strip dipole, but a narrow strip dipole generated more signals directly below the element.

The sensitivity calculations for each dipole were taken along the y axis of the dipole and were considered in different depths as shown in Figure 7.10-1. The results of the calculations showed that the four coils had very high efficiency close to the phantom and also that the efficiency of the coils dropped down in the depths as shown in Figure 7.10-2. The high efficiency reached a peak of 1.8 ($\mu T/W^{0.5}$) by the array dipole in near field regions, followed by flat-strips and narrow-strips. Images showed that very good coverage and a large field of view can be achieved by a dipole array followed and a flat dipole. Increasing the width of PEC that was mounted on the block tended to produce a larger field of view. The current amplitude on the flat-strip generated good RF field strength in the edges of the dipole and the central region. The simulations have shown that the dimensions of strips agree well with the field of view. The four coils generated high SAR values close to the surface of the phantom as shown in Figure 7.12-1 and Figure 7.12-2. The values can be estimated as the following 1.44 $(W/kg)/\mu T^2$, 1.52 $(W/kg)/\mu T^2$, 5.9 $(W/kg)/\mu T^2$ and 1.35 $(W/kg)/\mu T^2$ for narrow-strip dipole, flat-strips, two strips and array dipoles respectively.

7.15 Loaded One-Strip Dipole, Two-Strip Dipole and Flat-strip Dipole on the Human Pelvis

In next section, we demonstrate three different designs using the ceramic. All simulations were performed with the same grid, so the probes had to be identical, the voxel dimensions varying from 0.5 *mm* in the region of the dipole to 3 *mm* in

the pelvis. The human pelivs model consisted of 3 different tissues and 3 *mm* resolution was generated as described previously. We used an adaptive mesh in the region of the dipole, so we generated many voxels in this region compared with the pelvis region. Therefore, the dipole antenna appeared very large when data were imported from the files in MATLAB. The pelivs model was adjusted to match the dielectric such as the conductivity and permittivity of a human tissue at 300 MHz. The wavelength at 7 Tesla (300 MHz) depended on the type of tissue, as mentioned in Chapter three in the section in electric properties of biological material [10]. The wavelength inside the pelvis and the uterus (relative permittivity constant of 66.2) was about 12 *cm*. Therefore, the largest dimension of the pelvis was approximately more than twice of the operational frequency at 300 MHz.

The coils were placed above the pelvis model and were tuned to 300 MHz. When the coils were driven by a current source or voltage source it was difficult to tune it during the simulation, but we added a circut consisting of one capacitor used for tuning and a second used for matching. The second capcitor was used in the simulation just to reduce the impedance of the coil. It is very complicated to match the coil to 50 ohms in the simulation because we needed to change the value of the capacitor many times, and at certain values it started to act as a tuning capacitor. In simulation we may accept this because the simulation can always normilse to a power delivered to the coil.

Results of the simulation showed that two strips mounted on the dielectric material can be tuned at 300 MHz. Therefore the RF coil was tuned by changing the length of the strips. This was accomplished using a search loop coil which induced a current and EMF. Furthermore, it was noted that there was only a very weak coupling, and no splitting appeared in the spectrum. As we mentioned before, parasitic capacitance occurred between the two strips. It is possible that these capacitors worked approximately as decoupling capacitors elements. It can be said that the coupling between strips in an array dipole adds to variation in the input impedance of the dipole array.

In this study a new approach for designing a dipole was investigated. A flat-strip dipole was simulated as shown in Figure 7.15-1, by adding a wide PEC on the dielectric material to increase the field of view. The coil was driven from the middle of the coil by adding a small bridge (PEC) on the top of the flat strips. We placed a tuning capacitor between the two flat strips and a matching capacitor between the bridge and flat strip, the coil was tuned at 300 MHz. The RF field and SAR were simulated for the human pelivs loaded coil.

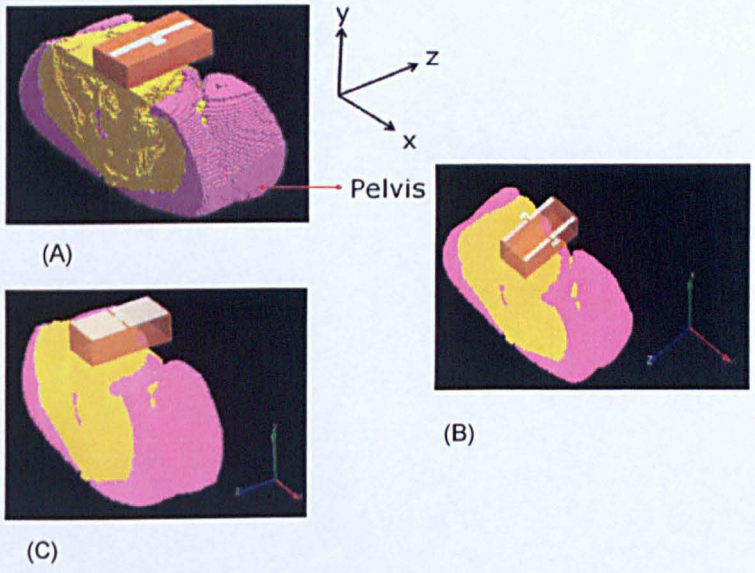

Figure 7.15-1: (A) A narrow strip, (B) two strips dipole and (C) flat strip dipole.

7.16 The B_1^+ Generated by the Dipoles

Figure 7.16-1 shows that there was very good distribution and also that the coil covered almost the surface of the pelvis model. By using this coil we were able to image all the field of view without moving the coil around the ROI. This has the advantage of minimizing the energy absorbed by the patient. Furthermore, The B_1^+ appeared to be uniform and covered the area close to the coil and the far field regions. It seems that a near field region had a high B_1^+ value and in the middle of the model as shown in Figure 7.16-1.

In this model, two elements were driven 90 degrees out of phase so there was a phase difference between the currents that flowed in the PEC. Therefore, adding more than one strip increased the field of view, two strips covered approximately all the pelvis. However, the B_1^+ values fluctuated; this was due to the inhomogeneity of dielectric materials such as conductivity and permittivity inside the pelvis. It can be noted that more magnetic fields appeared in the beginning of the pelvis and started to drop down in the end of the object as demonstrated in Figure 7.16-1 and Figure 7.16-2.

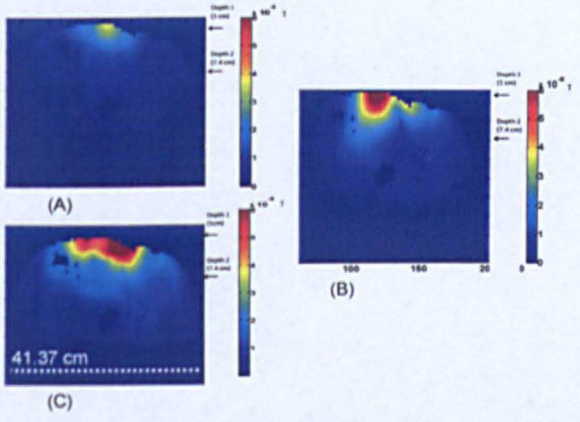

Figure 7.16-1: The B_1^+ produced by the dipoles: (A) a narrow strip, (B) two strips dipole and (C) flat strip dipole.

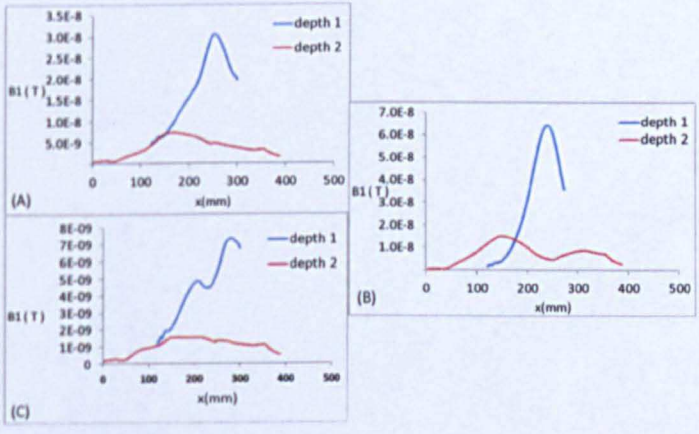

Figure 7.16-2: Computed in depth B_1^+ profiles for (A) a narrow strip dipole, (B) two strips dipole and (C) flat strip dipole.

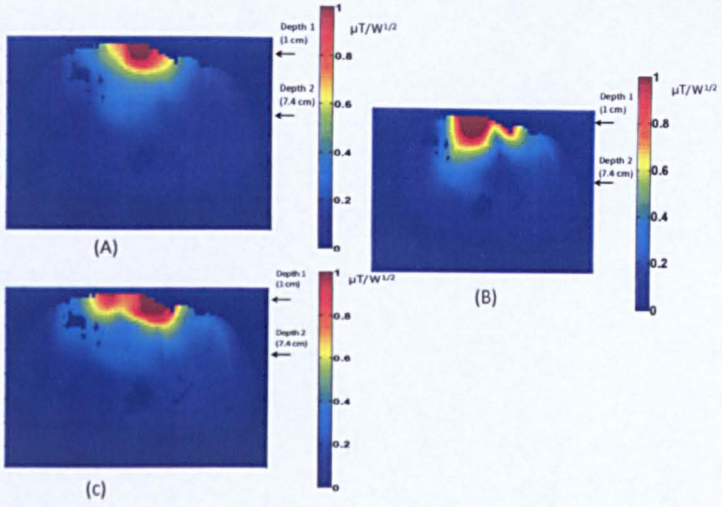

Figure 7.16-3: The efficiency mapping generated: (A) a narrow strip dipole, (B) two strips dipole and (C) flat strip dipole, in linear scale and normalized for 1 W delivered power.

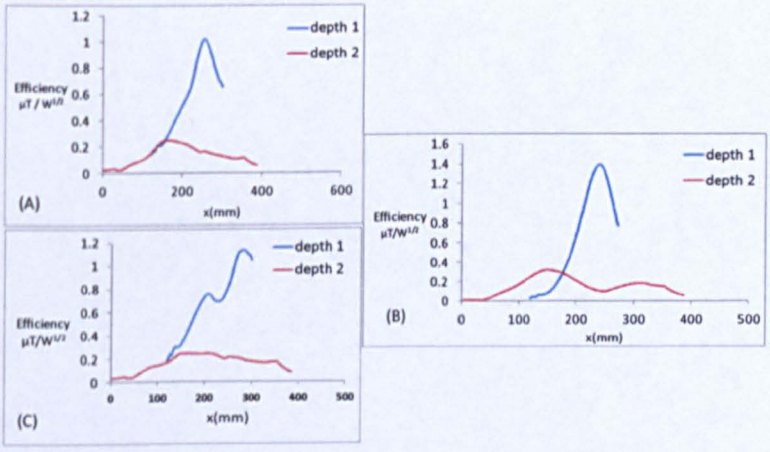

Figure 7.16-4: Calculated in depth efficiency profiles: (A) a narrow strip dipole, (B) two strips dipole and (C) flat strip dipole, normalized for 1 W delivered power.

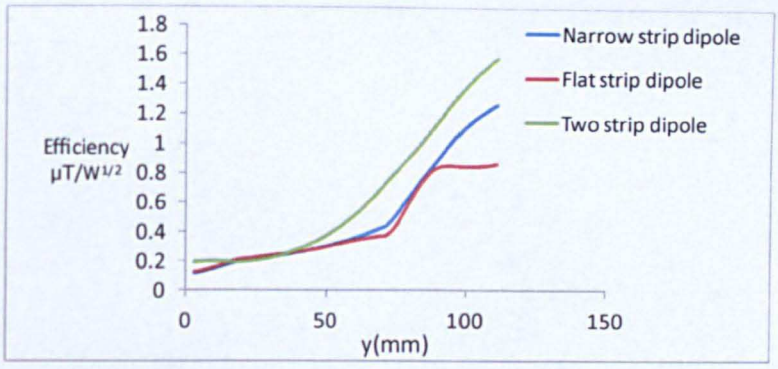

Figure 7.16-5: Calculated in depth efficiency profiles along a vertical line passes through the centre of each dipole: (A) a narrow strip dipole, (B) two strips dipole and (C) flat strip dipole, normalized for 1 W delivered power.

Based on the B_1^+, the results were used to calculate the power efficiency of each coil as shown in Figure 7.16-5. Plotting the vertical line profile across the image mapping for the three coils, the comparison results showed that the dipole consisting of two strips had higher efficiency compared with the one strip and flat strip. The two strips and flat strip have more advantage of increasing the efficiency and field of view, as well as there being more efficiency in depth using two strips as shown in Figure 7.16-5. It can be concluded that using the two-strips and flat-strips provides best coverage.

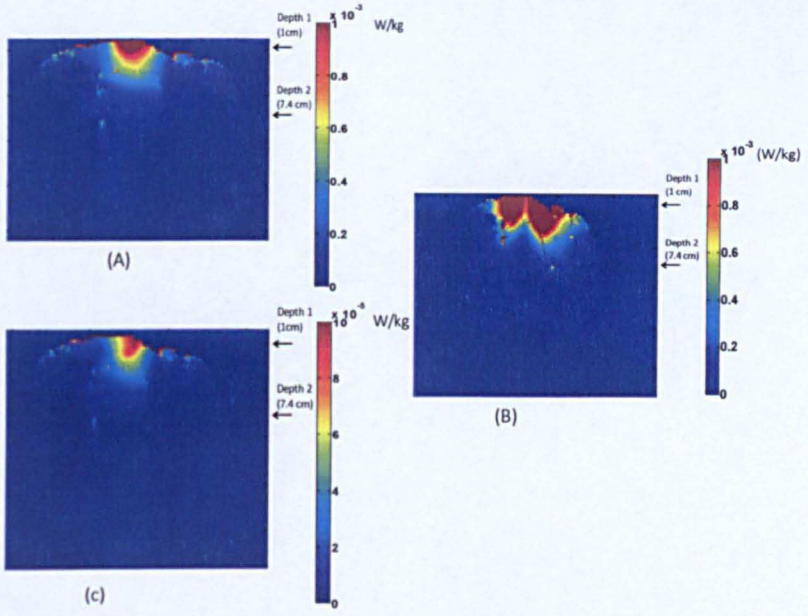

Figure 7.16-6: The SAR distribution (W/kg) generated: (A) a narrow strip dipole, (B) two strips dipole and (C) flat strip dipole.

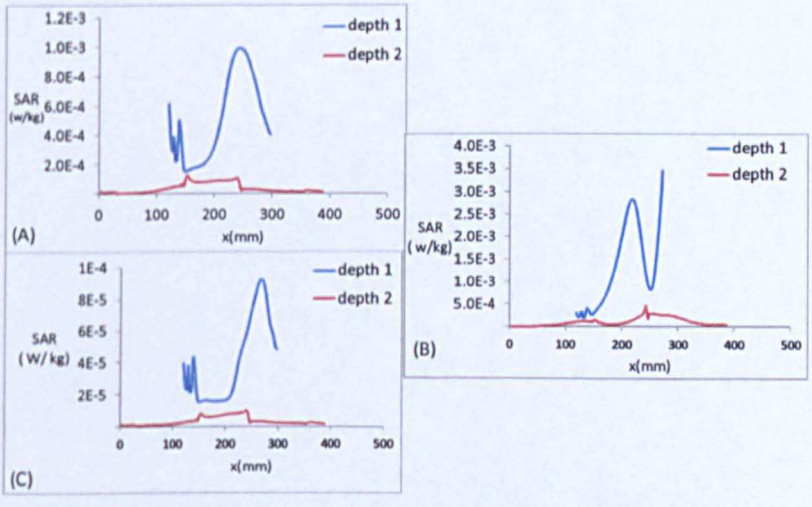

Figure 7.16-7: The line profile of SAR in depth: (A) a narrow strip dipole, (B) two strips dipole and (C) flat strip dipole.

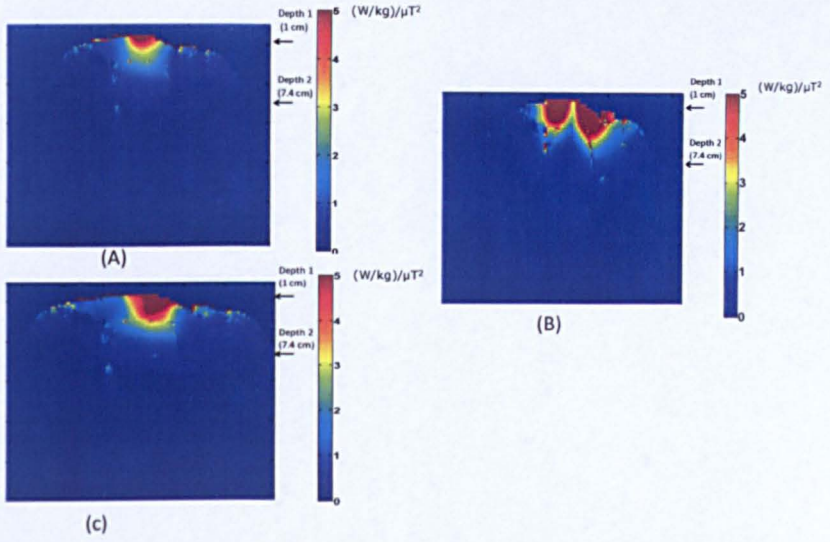

Figure 7.16-8: The SAR / B_1^2 distribution generated: (A) a narrow strip dipole, (B) two strips dipole and (C) flat strip dipole.

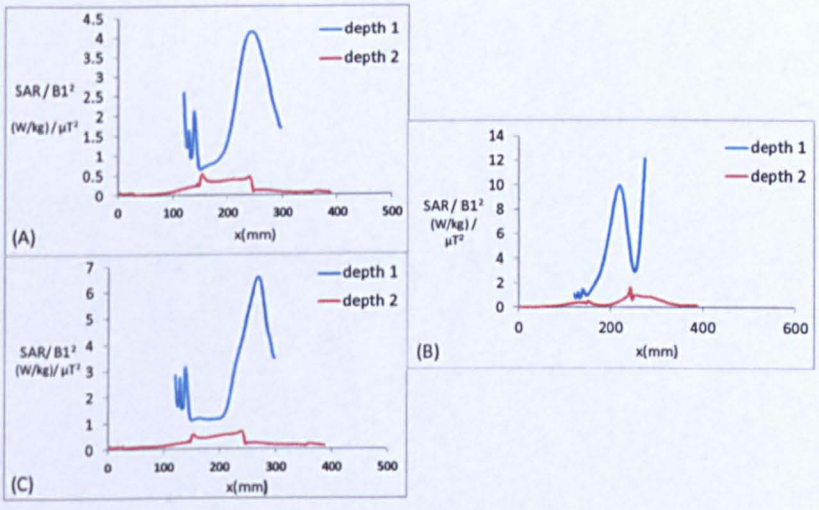

Figure 7.16-9: The line profile of SAR per B_1^2 in depth: (A) a narrow strip dipole, (B) two strips dipole and (C) flat strip dipole.

7.17 SAR

For safety validation, calculations of the SAR per B_1^{+2} were performed on the female pelvis model. The SAR was computed for each dipole and compared with

each other. Table 7.17-1 shows the flat-strip dipole generated more SAR compared with the one strip and two strips. Results of simulations showed that two strips mounted on the block can provided us with the lowest SAR. The two strips coil is the best with regard to the SAR and also the coil which covered most of the region of interest (ROI) of the pelvis. The coil produced lower SAR, due to the inhomogenity of the electric field and therefore we expect that the electric fields cancelled each other out in some regions.

Table 7.17-1

coil	Narrow strip	Two strips	Flat strip
Net input power (Watt)	8.91×10^{-4}	2.131×10^{-3}	4.15×10^{-5}
10 g average SAR (W/kg)	1.06×10^{-4}	3.48×10^{-4}	9.03×10^{-5}
(SAR/B_1^{+2}) $(W/kg)/\mu T^2$	0.102	0.967	2.78

7.18 Radiation Efficiency

The radiation efficiency is a significant parameter, which is affected by losses that may occur in electronic devices and materials surrounding the coil. It is defined as the ratio of the radiated power to the input power of the coil as the following

$$\varepsilon_{R=P_{radiated}/P_{input}}. \qquad 7.18.1$$

The radiation efficiency can be computed based on equation 7.18.1 for the narrow strip dipole antenna, flat strip and two strips dipole antennas. It can be noted that the efficiency of the narrow-strip dipole was better than the flat-strip and then followed by the two-strips.

Coil	Narrow-strip	Flat-strip	Two-strips
Radiation efficiency	54.14%	37.2%	33.24%

As the B_1^+ was computed, the results were used to calculate the power efficiency of each coil. This research has shown that plotting the vertical line profile across the image mapping for the three coils shows that the dipole consisting of two strips had higher efficiency and shows desired improvement compared with the one strip and flat strip whereas flat-strips provides good coverage. It can be concluded that the two strips and flat strip have more advantage of increasing the sensitivity and field of view, as well as there being more efficiency in depth using two strips.

7.19 Construction of the One-Strip, Flat-Strip, Two-Strips and Array Dipoles

In this section, the dipoles with different strip shapes were built as shown in Figure 7.19-1. There are three possible structures; the dipoles were built with the same dimensions that were used in the simulations. MRI results comparison was performed and some of the results were summarized in the sections 7.20, 7.21 and 7.22. The coil consisted of a dielectric ceramic (15 x 7.3 x 4 cm^3, ceramic material is D36 made by Morgan Technical ceramic, UK), with copper mounted on top of the dielectric. The coil was tuned at 294.6 MHz as a self-resonance when 13.6 *cm* copper length was placed on the top of dielectric. Each arm of the dipole was a quarter wavelength long (6.7 *cm*) so that the maximum current distributions were at the centre and the nodes were at both ends. It is important to point out that the dipole could be fed at any point but it was fed at the minimum voltage and maximum current point i.e. to generate very low impedance. By adding a half wavelength coax cable, which acted as a balun and a matching and tuning circuit, the antenna could be tuned at 298 MHz and matched to 50 ohms. The circuit shown in Figure 7.19-2 was made of two variable capacitors which were enclosed in a plastic box, one for tuning and the second for matching. This circuit uses a half wavelength line between the circuit and dipole to ensure no change in impedance due to impedance transformation. In order to obtain 50

ohms impedance at the circuit where the capacitors were soldered is exactly the same if the capacitors soldered on the dipole. These properties should be clearly obtained at the frequency for which the line is a half wave long. This needs an accurate cutting of the cable, but it would not have mattered if the length of the cable had been slightly greater or less than a half wavelength, a small difference in the electric length of the cable has no dramatic on the performance of the dipole. The coaxial cable behaves as a capacitor or inductor, depending on the length, this was discussed in detail in chapter three.

The main advantage of this kind of feeding scheme is that the tuning and matching capacitors were placed away from the region of interest. This will reduce the electric fields in this location producing by the capacitors. It has been shown that a good level of matching was obtained and therefore the dipole worked at its maximum efficiency. This circuit is suitable for impedance matching of a dipole antenna and tuning the coil at 298 MHz.

An increase in the FOV and efficiency of the probe can be achieved by adding two additional elements, which act as two dipoles. The coil now consists of two ports which are connected to the quadrature interface box. This mode allows a sensitivity gain by a factor of up to $\sqrt{2}$. We attempted to tune the two elements at their-resonance without adding any electric component such as a capacitor. It was found that each element tuned at a further self-resonance at 294.6 MHz when the length of each element was about 13 cm. As the coil will be used on the 7T, the elements had to be individually tuned at 298 MHz and matched to 50 ohms. In this case two elements were connected to two electric circuits for tuning and matching. It was noted that there was coupling between the two elements, observed in the network analyzer, and the resonance frequency split into peaks. It can be said that mutual impedance between elements in dipole array was generated. Coupling in the dipole array added variation in the input impedance of the coil. It became very complicated to tune and match the dipole array when two elements were placed in the same block. If we had had two blocks, the mutual

impedance could have been minimized by placing the blocks further away from each other.

The aim of designing and building an array dipole was to increase the field of view. The size of the coil such as length and width is determined in the laboratory by tuning the coil to a self-resonance of 294 MHz. It can be noted that the results agree well with simulation. The coil was loaded on the phantom, therefore, it was tuned and matched at 298 MHz and 50 ohms and we used the same circuit as before.

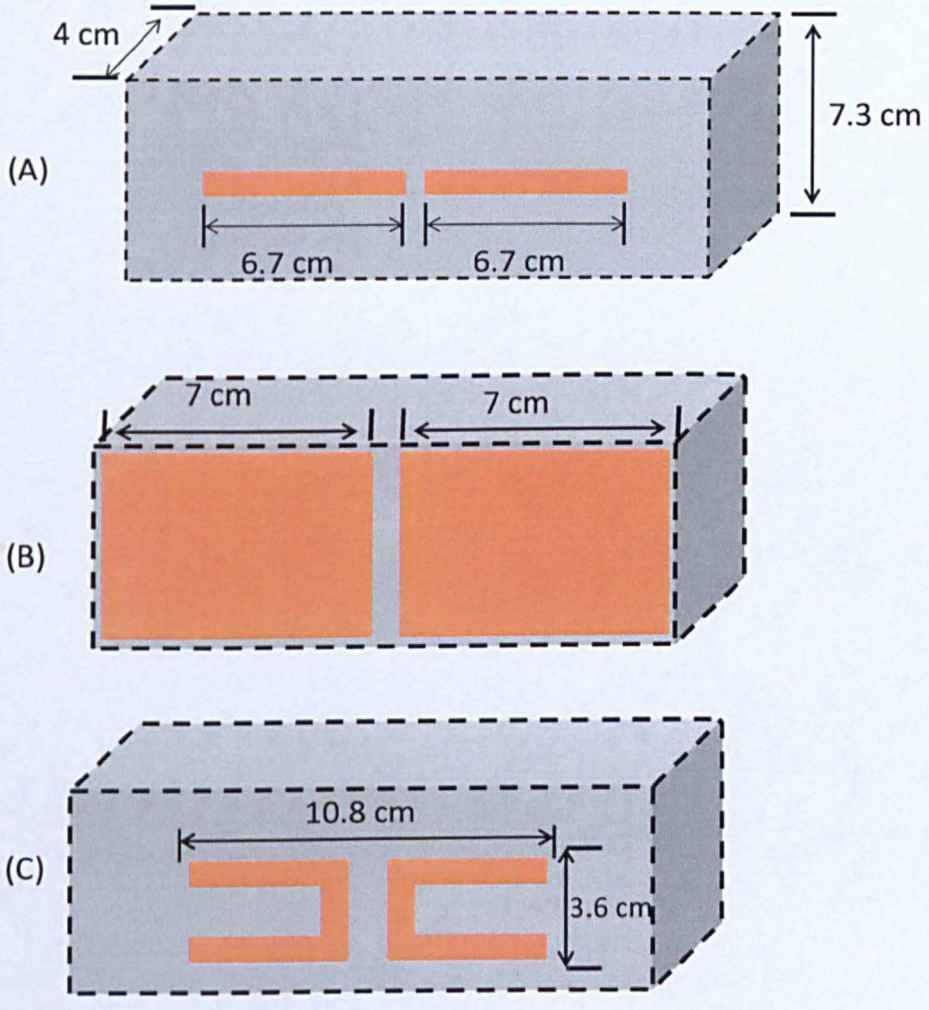

Figure 7.19-1: The schematic and the geometrical dimensions of the dipoles: (A) Narrow strip dipole, (B) Flat strip dipole and (C) Array dipole.

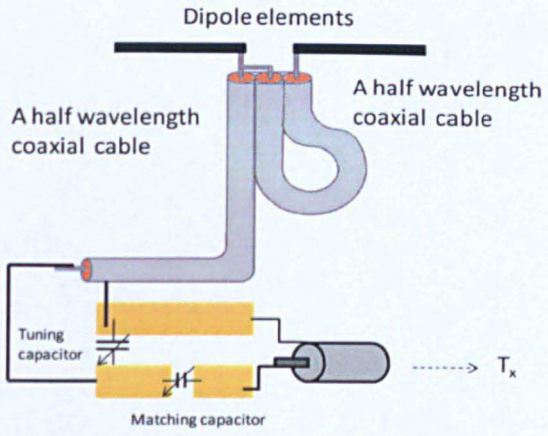

Figure 7.19-2: The schematic of the balun, tuning and matching circuits.

7.20 Comparison with Phantom Studies

This section refers mainly to the assessment of the three constructed dipoles. These were tested by loading with the gel phantom. The dipoles were connected to a quadrature interface box, and 50 ohms were connected to the second channel to terminate the line, therefore a $\sqrt{2}$ reduction in signal to noise ratio [11] is expected. The dipole had to be placed as close as possible to the phantom and we ensured that it was parallel to the z axis of the magnet, which guaranteed that the transverse magnetization B_1^+ was generated in the *x* and *y*-axes perpendicular to the dipole and that maximum signal is produced. Placing the dipole at an angle to this axis would have resulted in a loss of signal. The three dipoles (The narrow strip dipole, flat strip dipole and dipole array) were tested on the 7T and loaded with the gel phantom. Images were acquired with the same sequence FEEPI and with the following parameters:

TR/TE = 8000/28.45 *ms* and a flip angle=90^0 parameters. The axial slice of the phantom is shown in Figure 7.20-1. It can be seen that the antenna covered both near and far fields regions and the intensity was good in both regions.

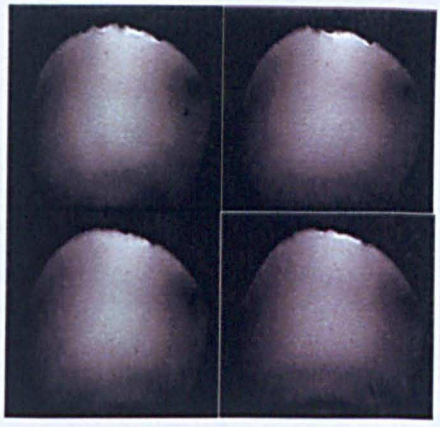

(A) Narrow strip dipole

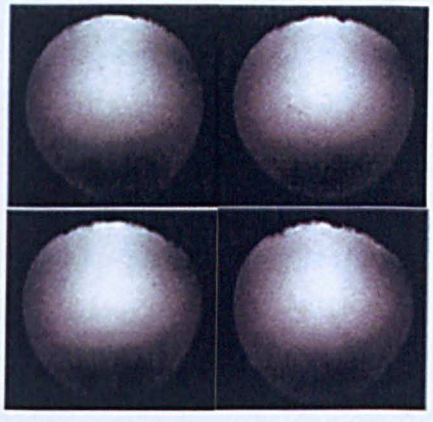

(B) Flat strip dipole

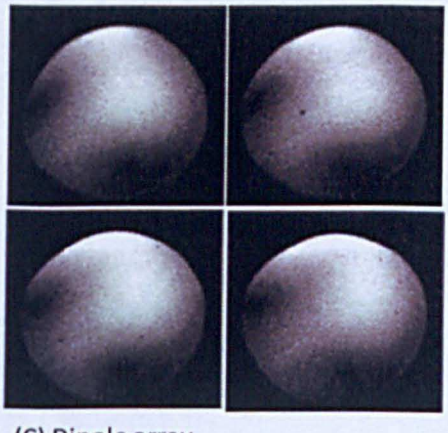

(C) Dipole array

Figure 7.20-1: (A) Testing on the 7T a narrow-Strip dipole, (B) flat strip dipole and (C) dipole array. The images were obtained with two cylindrical homogeneous phantoms (8.5 *cm* diameter, 17 *cm* in length) using a FEEPI sequence, TR/TE of 8000/28.45 *ms* and a flip angle=90°.

The SNR comparison of the dipoles was obtained with a homogeneous gel phantom and was performed at the centre of the phantom images in the *z*-axis direction. The SNRs were computed at the same depth and plotted on the same graph for comparison, as shown in Figure 7.20-2. This shows that the SNR profiles along the z-axis for transverse phantom images reached a peak in the middle of the coils and then decreased at both ends of the coils. The SNR with a flat strip dipole was a little higher than with a narrow strip, followed by four strips dipole, but at the feed points of the dipoles, two small peaks appeared in the centre. More precisely it almost reached zero at the end the copper strips, the SNR was distributed as a current distribution that has been demonstrated in section 7.7. The current reached a maximum at the centre and two nodes in the end of the copper strip. It can be said that there was a good agreement between the measured and simulated graphs. It is necessary to obtain more information about the homogeneity and one way in which this can be achieved is to look at the distributions of the SNR or average signals and then to present them as the histograms. Comparing Figure 7.20-3 A, B and C, it can be noted that the flat dipole is more homogeneous than the array and narrow strip dipoles. Furthermore, based on the results described in Figure 7.20-3, it can be noted that the simulated data for the narrow strip dipole, flat strip dipole and array dipole are in good agreement with the measured images.

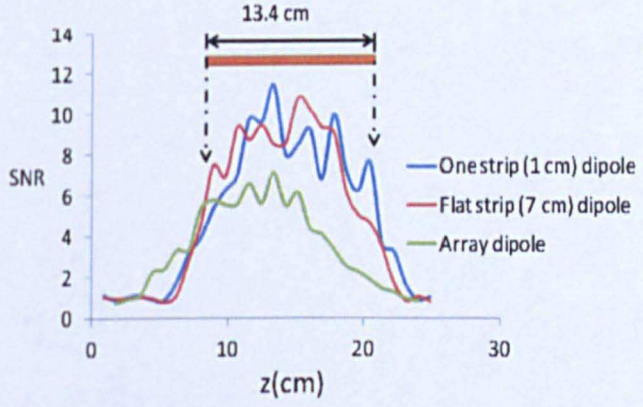

Figure 7.20-2: SNR profiles of phantom images, plotted of SNR versus distance in the z direction correspond to axial plane generated by three different dipoles.

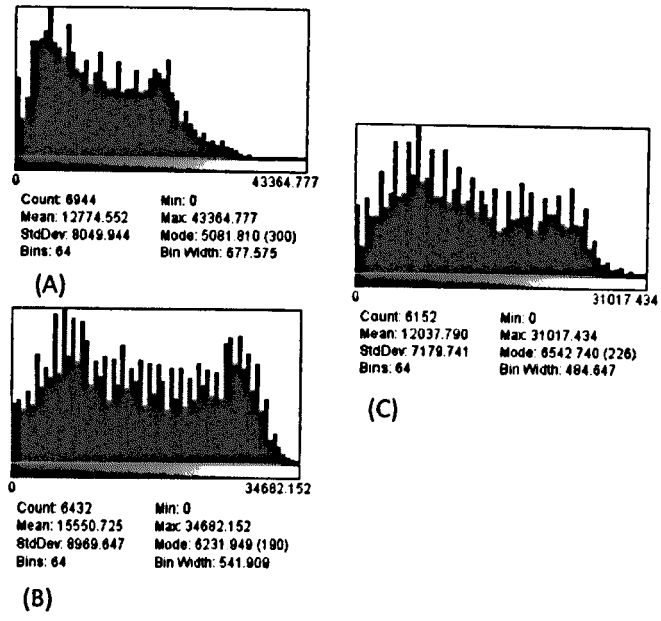

Figure 7.20-3: The histograms show distributions of data values (mean signals) generated: (A) a narrow strip, (B) flat strip dipole and (C) array dipole.

7.21 *In Vivo Imaging* (One Strip Dipole)

After construction and testing of the probe loaded on the phantom on a 7T, the first *in vivo* images were taken of a human knee then followed by image of a human pelvis. The dipole was placed on the upper surface of the knee as shown in Figure 7.21-1 and then matched and tuned in the network analyzer, using circuits discussed in the section 7.19, which is easy to use. Various imaging methods have been attempted to image a human knee. Images were performed on the 7T to scan the volunteer (left knee). The FFE sequence was used with the following parameters: TE/TR=4.94/20 *ms*, a flip angle=100°, FOV=170×67.5×170 mm^3.

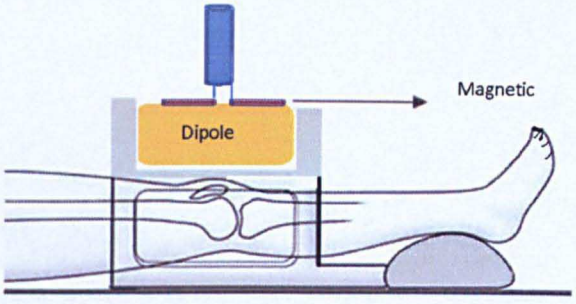

Figure 7.21-1: Correct placement of a dipole in the magnetic and it should be parallel to z axis.

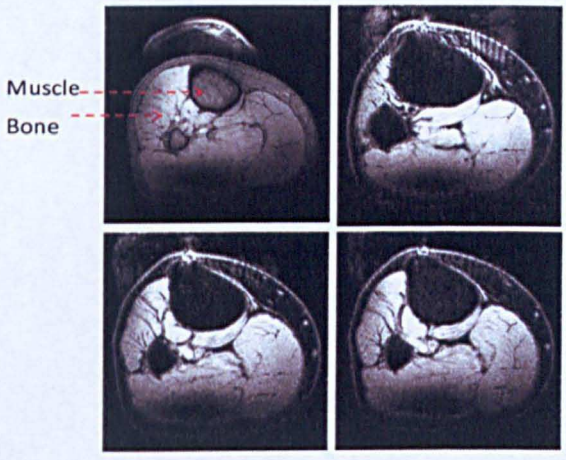

Figure 7.21-2: Transverse knee images taken by the dipole.

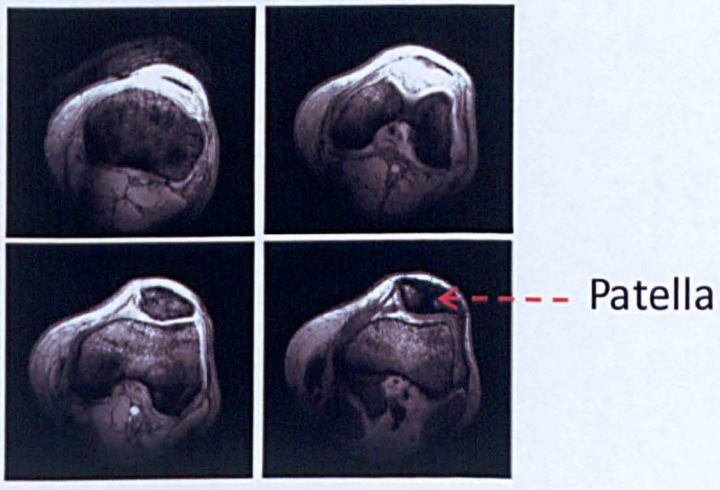

Figure 7.21-3: Transverse knee images taken by the loop coil.

It can be noted that the dipole antenna provided us with very good data compared to the loop coil. One of the most interesting observations is that the dipole covered both near field and far field regions, where the energy was flowing away from the dipole and the electromagnetic energy propagated into the knee. The structure of the subject was clear; patella, muscle, fat, bone, veins, and trabecular bone were evaluated in the image and could be easily identified from the image slice. The images obtained from the dipole antenna and loop coil can be compared in Figure 7.21-2 and Figure 7.21-3. The dipole antenna showed the desired improvement in SNR and more homogeneous coverage compared to a square loop coil design. Coverage went much further into the knee, indicating that the dipole antenna is better suited for imaging structures deeper into in the body, such as the pelvis.

The one-strip dipole antenna was used to scan the pelvis. The dipole antenna was placed anterior to a female pelvis for tuning and matching to the load before it can be used on the scanner. On the 7T a Turbo Spin Echo sequence was used to obtain images from a healthy volunteer in the proliferative phase of her cycle with following parameters: FOV=180×180×37 mm^3, voxel size 0.7x0.8x3 mm^3, TE/TR=520/80 *ms*, which used a nominal refocusing flip angle which varied from 110 to 170°. It has been shown that the dipole antenna provides us with very good image quality and contrast at sub-millimetre resolution as shown in Figure 7.21-4. It can be seen that the dipole covers both near field and far field regions where the energy is flowing away from the dipole and the electromagnetic energy propagates into the pelvis.

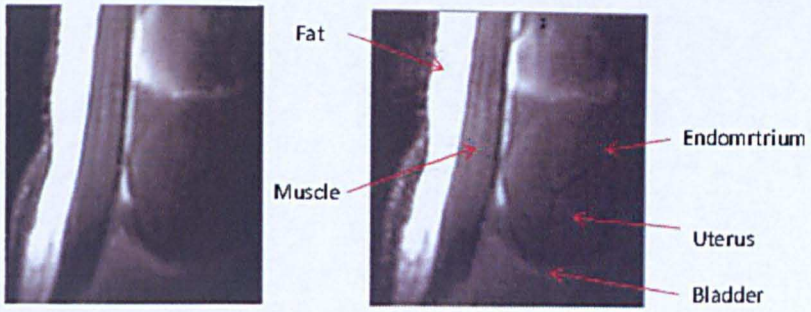

Figure 7.21-4: Transverse pelvis images taken by the dipole.

The anatomy of the pelvis is clearly demonstrated such as skin, fat, muscles and myometrium and endometrium of uterus. The sequence is surprisingly robust to the variation in B_1^+ across the field of view, but further work is required to improve the refocusing pulse and improve image contrast. The dipole antenna shows the desired improvement in SNR and homogeneous coverage. Coverage goes much further into the pelvis than is shown in Figure 7.21-4 the image, indicating that the dipole antenna is better suited for imaging structures deeper into the body than loop or strip transmitting elements. This study has been demonstrating that MRI has proven useful in showing the soft tissue of the pelvis.

7.22 *In Vivo Imaging* (Flat Strip Dipole)

Flat dipole was designed and constructed to increase the field of view. The dipole was placed anterior to the knee with patient lying on the supine position and then placed on female pelvis to image uterus and the pelvis.

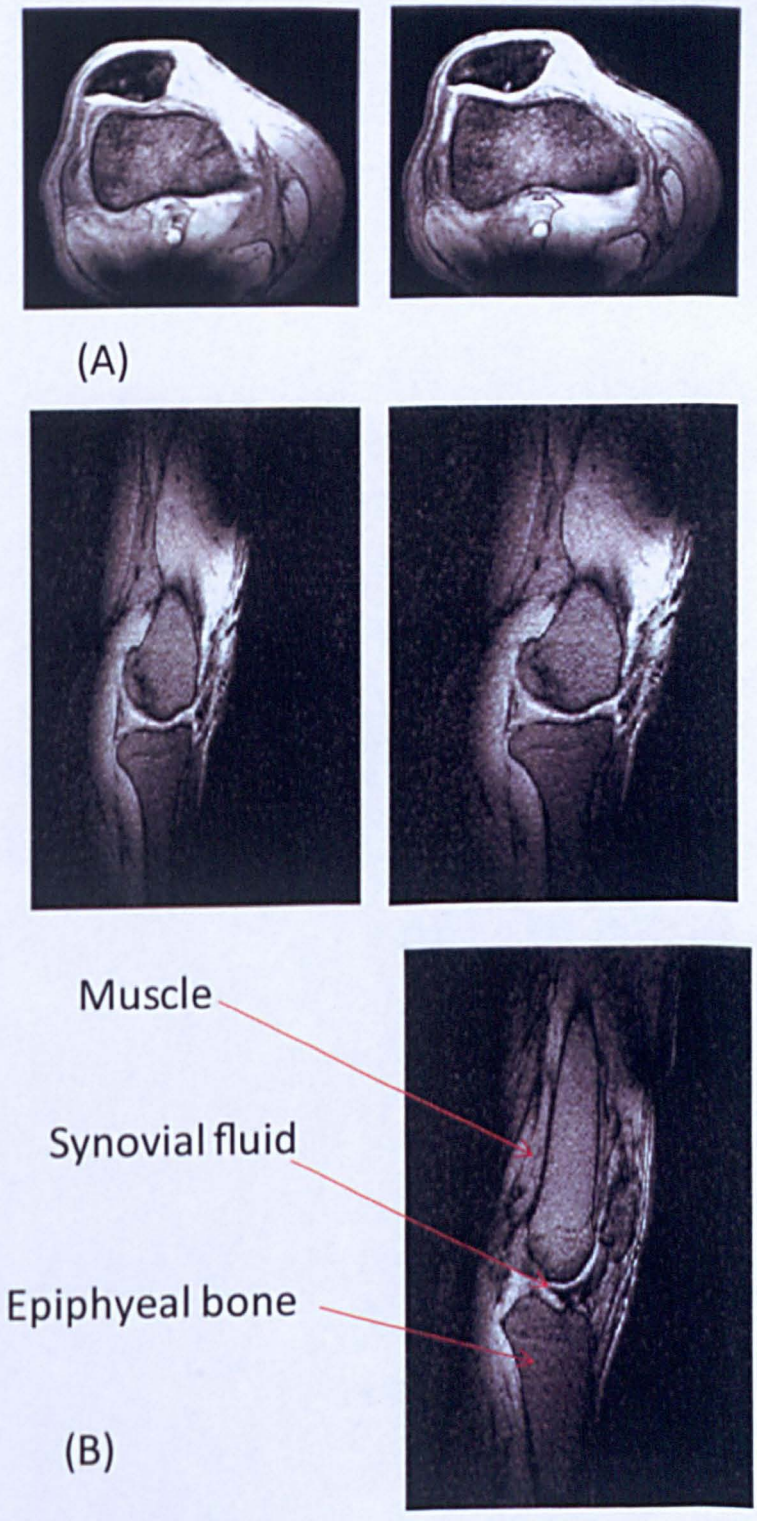

Figure 7.22-1: (A) Transverse knee images and (B) coronal section of left knee-joint images taken by the flat strip dipole.

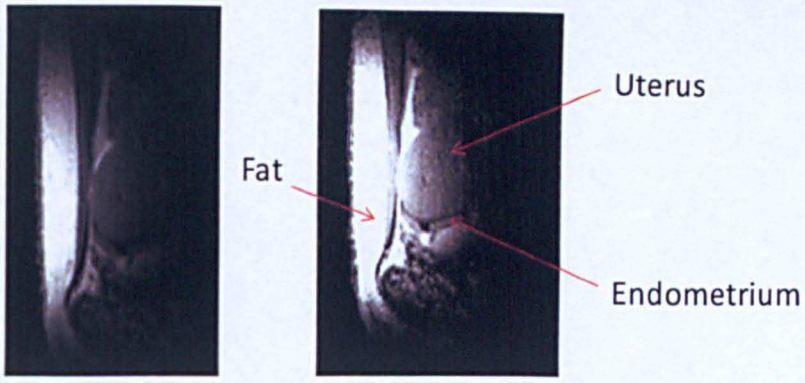

Figure 7.22-2: Transverse pelvis images taken by the flat strip dipole.

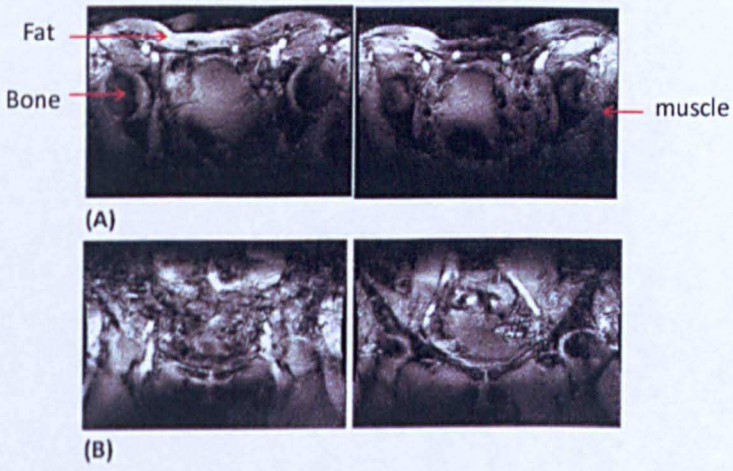

Figure 7.22-3: (A) Transverse pelvis images, (B) coronal pelvis images of healthy volunteer taken by the flat strip dipole.

7.23 Discussion

In this section, we compare results of simulations and experiments such as one-strip dipole, two-strip dipole, and flat-strip dipole antenna loaded by the muscle tissue phantom and on the dielectric model of the human pelvis. All the coils in the simulations were tuned at about 300 MHz. The five important parameters were considered such as B_1^+, homogeneity, efficiency, SAR/B_1^{+2} and Poynting vector for the design of the dipole.

The SAR/B_1^{+2} profiles produced by the four dipoles were taken in x-directions. Results showed that the maximum SAR/B_1^2 was generated directly below the dipoles and level was highest for the two-strips, followed by the flat-strip and reached a peak at 5.9 $(W/kg)/\mu T^2$ and 1.52 $(W/kg)/\mu T^2$ respectively. The lowest SAR produced by the array dipole and narrow-strip were 1.35 and 1.44 $(W/kg)/\mu T^2$ respectively.

From all these results, we can conclude that the field of view was increased in horizontal direction when two-element and also a flat strip were placed on top of dielectric material. The flat strip dipole can provide higher SNR and better uniformity followed by a narrow strip dipole and array dipole. These designs improve field homogeneity and field of view in comparison to a narrow strip dipole.

References:-

1. Bin, X., Q. Wei, L. Feng, and S. Crozier, *An Inverse Methodology for High-Frequency RF Coil Design for MRI with De-emphasized B1 Fields.* IEEE, 2005. **52** (9).

2. Raaijmakers, A.J.E., O. Ipek, D.W.J. Klomp, C. Possanzini, and C.A.T. Van den beng, *Design of a Radiative Surface Coil Array Element at 7 T: The Single-Side Adapted Dipole Antenna.* Magnetic Resonance in Medicine, 2011. **66** (5): p. 1488-1497.

3. Raaijmakers, A.J.E., D.W.J. Klomp, C. Possanzini, and N. van den Berg, *High-field imaging at low SAR: Tx/Rx prostate coil array using radiative elements for efficient antenna-patient power transfer*, 2010, ISMRM: Sweden.

4. Chen, X., V. Taracila, and H. Fujita, *An Antenna-Theory Method for Modeling High-Frequency RF Coils: A Segmented Birdcage Example.* International Journal of Antennas and Propagation, 2008. **10**: p. 10.

5. Thomas, K.F., C. Hayes, and N.W. Kang, *Reduction of RF Penetration Effects in High Field Imaging.* magnetic resonanc in Medicine 1992. **23**: p. 287-301.

6. Hoult, D. and R. Deslauriers, *A High-Sensitivity, High-B1 Homogeneity Probe for Quantitation of Metabolites.* Magnetic Resonance in Medicine, 1990. **16**: p. 411-417.

7. Jackson, J.D., ed. *Classical Electrodynamics*. 1998, John Wiley and Sons,INC.

8. Ulaby, F.T., E. Michielssen, and U. Ravaioli, *Fundamentals of Applied Electromagnetics*2010: Pearson.

9. *Dipole antenna*, 2012: http://en.wikipedia.org/wiki/Dipole_antenna.

10. Gabriel, C., S. Gabrriel, and E. Corthout, *The dielectric properties of biological tissues.* Phys. Med. Biol., 1996. **41**: p. 2231-2249.

11. Mispelter, J., M. Lupu, and A. Briquet, *NMR Probeheads for biophysical and biomedical experiments* 2006: Imperial college.

Chapter 8

Discussion and conclusion

8 Discussion

The RF coil is a very important part of the MRI scanner. The coil can have two functions: transmit (T_X) and receive (R_X). The work in this thesis has focused on the development of RF probes that have good uniformity, efficiency and low SAR level. They can be used at a high field frequency to image anatomy such as the female pelvis as well as the knee and wrist

The first study was the wrist probe detailed in Chapter 4. The probe acts as a receiver only and it consists of two identical elements. We could not observe the coupling between the two elements in the simulation, but two-element resonated individually at 298 MHz and then the B_1^- and sensitivity were computed by exciting the receiver using a small search loop coil. The B_1^- field was first obtained for each individual element and then for two elements together, in order to estimate the B_1^- uniformity. This is proportional to the sensitivity and was used for comparisons. From the simulation results and practical applications, it can be said that two-element is enough to detect the signals from the region of interest (ROI). In the laboratory decoupling between two elements was minimised by using a low input impedance pre-amplifier. When connecting the probe to low input impedance pre-amplifier, two elements became invisible to each other which functionally independent and can detect the signal from a single region of interest. The images obtained from the 7T had a high resolution about 0.5 mm^3 and good quality. The structure of the human wrist can be seen clearly such as muscle, bone and blood vessels.

The second, third and fourth studies in this thesis were to develop conventional coils such as a loop coil and strip line and dipole probes. For modelling the probes were loaded with equivalent tissue homogenous phantom (conductivity of 0.77 S/m and relative permittivity of 58.2) and the pelvis model was generated from our own MRI data. The pelvis images were obtained from the 3T MRI scanner using the body coil that functions as transmit and a receiver coil. MATLAB code was used to convert the segmentation data to XFDTD geometry file format to be compatible with XFDTD software. The healthy pelvis tissue was divided into four types: fat, muscle, bladder and inner air. There are two main parameters of biological material; conductivity and relative permittivity. The permittivity of media varies with frequencies. The pelvis mesh file was loaded in XFDTD and then the dielectric properties of tissues were computed at 298 MHz. The pelvis model was used when modelling the loops, strip lines and dipoles. The probes had similar dimensions and FOV for comparison. All probes discussed in this thesis were both simulated and constructed.

In Chapter 6 the coupling of two loops was computed and then the overlapping technique was used in the simulation to decouple two elements. By using this method two elements were decoupled and became invisible to each other. The results of the simulations of one loop coil and two loops showed that the loop coil has higher efficiency in a near field but rapidly dropping off farther away from the coil. However, the B_1^+ values were sum constructively in the middle of the coil due to the combination of both elements. It can be demonstrated that this higher efficiency should be between two elements and the efficiency was increased when adding two elements in horizontal direction. It was noted that two loops provided better uniformity and can generate a large field of view than compared to a one element coil. The two-element covered about 25 cm whereas one element covered about 15 cm. This indicates that probe picks up signals from the region surrounding the probe.

Furthermore, during the modelling of the loop coil, it is observed that adding more series tuning capacitors can decrease the net electric fields at these locations. SAR hot spots appeared near to the locations of the tuning capacitors. This is due

to the conservative field potential which contributes to the electric fields at these locations. The second advantage when distributing *n* capacitors is that, this design can be loaded to any patient and these reduced the effect of loading. This is due to the total parasitic capacitance being minimized with respect to the total loop capacitance. It is also reflect of the reduction of the reduced electrical coupling, which leads to local SAR.

In Chapter 5 it was shown that the strip line coil, one strip line and two strip coils could be simulated and loaded with the phantom and pelvis model. When the probe was assessed on the work bench, no coupling appeared on the network analyzer while in the modelling, there is a weak coupling present but without splitting the main resonance frequency. By driving one strip line with voltage source, it was found that the current flowed in the second strip line. It was found that having two elements coil improved several parameters when compared to a single element. The coverage was increased and then two elements provide better homogeneity compared to one strip line coil. The SAR was computed at the location of tuning capacitor, where it was noted that hot spots appeared. This is due to conservative field potentials. The one strip and two strips were tested on the 7T. Images showed that the higher signals appeared at the position of driving the coil and then decay along the strips. It means that high signal intensity should be close to this area. From these results, it can be said that the strip line coils are suitable for imaging a volume sample. When using a volume coil design by using many strips surrounding the region of interest, the signal intensity generate by each element will be added in the middle of the volume and also a little in near field region.

The work in this thesis demonstrated that the simulations agree well with both electromagnetic theory and practice. The electromagnetic fields of an antenna can be divided into near field and far field regions. The loop and strip line can image the near field region when the region of interest located in this field while far field region can be achieved by the dipole antenna. The fourth study in Chapter 7 was to design and construct an RF probe to image a human pelvis. The dipole antenna was selected, because it was found that the dipole had a high efficiency further

from the coil and the dipole probe can overcome many problems such as imaging the far field region with a low local SAR level such as the uterus. First a dipole in the water was considered to estimate the performance parameters such as the efficiency. The dipole was placed in the dielectric material of water. It was tuned to a self-resonance at 298 MHz and matched to 50 ohm. The dipole was tuned by adjusting the length and in the simulation and laboratory no electrical components such as capacitors were used to tune and match the dipole. This was followed by modelling for geometrically different dipoles using a block material made of ceramic. Subsequently these were built using copper tape on the top of the block as a narrow strip, two strips, flat strips and array strips during the simulations and experiments.

In the phantom and pelvis model study, the transmit efficiency $B_1^+/\sqrt{P_{delivered}}$, SAR/B_1^{+2}, field of view (FOV) and homogeneity of each probe was analysed and the Poynting vectors for the four dipoles were computed and then compared. The Poynting vector magnitudes were computed in the vertical and horizontal directions. It was found that the Poynting vector pointing into the phantom in the vertical direction. The dipoles transmitted the electromagnetic energy and it propagates into the near field and far field regions as demonstrated in the modelling. In the practical applications when the normal volunteers were scanned the anatomy such as the knee and uterus were scanned by the dipoles on the 7T. We obtained good resolution and high quality images when the knee was imaged by the dipoles compared to the loop coil. The structure of the knee such as trabecular bone, patella, muscle and fat were very clear when imaging the knee using the dipoles compared to the loop coil.

It can be concluded that the strip line and loop coils generated high electric fields at the tuning capacitor locations. This increased the local SAR in these locations. The strip line is not suitable for the surface coil. For safety validation, the max SAR level per B_1^{+2} was calculated for each probe. It was found that the SAR/B_1^{+2} produced by one strip dipole, flat dipole and two strips dipole much less produced than by the strip line coil and loop coil in the pelvis.

This indicated that the dipoles probes have a good SAR performance in the pelvis. The dipole probe is a safe to use on the 7T. Furthermore, the flat dipole can provide a large field of view and produce better homogeneity compared to two strips dipole and dipole array. The efficiency of each probe was computed. The dipole antenna provided better efficiency and deep penetration compared to strip line and loop probes. The efficiency and homogeneity increased in the horizontal direction when adding more than one loop and strip line coils. Hence, it was found that the high SAR was very close to the PECs and at locations of the capacitors when modelling the loop and strip line coils. However, PECs and capacitors were mounted on the top of the ceramic which is further away from the sample and capacitors were placed a half wavelength line away from the region of interest. I would recommend that the dipole antenna is a safe probe to use, because it can generate a low local SAR level, and has better efficiency and homogeneity compared with conventional probes. The images obtained by the dipoles have high quality. However, building the probe by using a dielectric made of the ceramic is very expensive, one block while using a high power capacitors is much less expensive.

8.1 Future

The wrist coil was built as two elements, it can be suggested that increasing to more than two elements will enhance the signal to noise ratio. The receiver coil should be as close as possible to the human wrist, as higher B_1^- values occurred very close to the edges of muscle tissue phantoms. This can be achieved by making the coil as small as possible. We have simulated a dipole antenna consisting of two strips on the ceramic. Modelling showed that there is no coupling appears in resonance frequency but still coupling exists. An attempt was made to build the coil in the Lab; but it was found that there is strong coupling. It can be suggested that in future work, decoupling two strips by using the same size of the block or by placing the elements on two blocks and then separating the blocks away from each other by distance d as shown in Figure 8-1. The field of view and the efficiency can increase by driving two elements 90 degree out of phase. The two elements coil will generate circularly polarized when two

orthogonal fields have the same amplitude but are 90 out of phase. Further modelling requires to be carried out to consider the effect of placing two dipoles close to each other.

An attempt was made to build a receiver coil, but it was found that the quality factor of the receiver coil was affected when the receiver was placed between the phantom and ceramic. The block material should be placed as close as possible to the region of interest to reduce the loss of RF and minimize the reflection of the electromagnetic field between the surface of the sample and ceramic. We suggest that building an array receive probe would consists of many elements close to each other and the diameter of each element should be very small as much as possible to increase the quality factor. Decreasing the size of the coil reduced the overall of parasitic capacitance that occurred between the sample and coil and also between the dielectric material ceramic and coil. This will act to increase the quality factor.

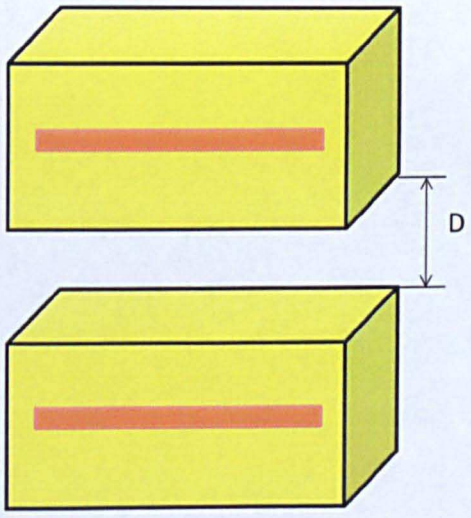

Figure 8-1: the dipole array.